ILL for scanning

Area Change Effects On Shock Wave Propagation

Jonathan Neil Dowse

A dissertation submitted to the Faculty of Engineering and the Built Environment, University of the Witwatersrand, Johannesburg, in fulfillment of the requirements for the degree of Master of Science in Engineering.

November 20, 2012

Declaration

I declare that this dissertation is my own, unaided work, except where otherwise acknowledged. It is being submitted for the degree of Master of Science in Engineering in the University of the Witwatersrand, Johannesburg. It has not been submitted before for any degree or examination at any other university.

Signed this 26th day of April 2013

Jonathan Neil Dowse.

Acknowledgements

I would like to thank the following people for their contributions.

Professor Beric Skews for his advice, patience and guidance throughout this project.

Mr Randall Paton for his support during manufacturing, testing and CFD preparations.

Mr John Cooper and the laboratory staff for the manufacture of the experimental profiles and their expertise during testing.

My beloved fiancé, Amy, and my parents, Lorraine and Russell, for their motivation, love and support.

Abstract

The work presented in this dissertation describes the effects that an area change has on shock wave propagation. Of particular interest is the analysis and optimisation of a gradual area reduction whereby a shock wave may be optimally strengthened. Experimental testing is conducted for a planar shock wave of $M_s = 1.33$ propagating through one of three compound parabolic profiles of 130, 195 or 260mm in length, all of which exhibit an 80% reduction in area. Experimental images were captured using an innovative colour schlieren setup for high–resolution images and lower resolution high–speed video. Results showed that there exists three main types of flow scenarios for propagation through a gradual area reduction, and an optimal net increase of 12.7% in shock Mach number was calculated for the longest profile of 260mm which was predicted to within 5% theoretical predictions using Milton's (1975) modified CCW Relation.

}

Published Work

Aspects of this dissertation have been presented at the following conferences:

J.N. Dowse and B.W Skews. Area Change Effects on Shock Wave Propagation. Proceedings of *28th International Symposium on Shock Waves*, Manchester, UK July 2011.

I.E. Ivanov, J.N. Dowse, I.A. Kryukov, B.W. Skews and I.A. Znamenskaya. Kelvin-Helmholtz Instability on Shock Propagation in Curved Channel. Proceedings of *15th International Symposium on Flow Visualization*, Minsk, Belarus, June 2012

Contents

List of Figures

List of Tables

List of Symbols

A	Cross-sectional area of ray tube, cross sectional area of one-dimensional tube
a	Speed of sound
C^+, C^-	Characteristics
H	Profile height
L	Profile length
M	Mach number, Mach stem
N	Number of coordinates across shock front
$\hat{\boldsymbol{n}}$	Normal to shock front
P	Particle path
p	Pressure
Q	Horizontal distance from profile start of the profile to the point of inflection
t	Time
T	Total time for simulation
u	Flow velocity
$\boldsymbol{x}$	Shock front position
x, y, z	Cartesian coordinates
z	Shock wave strength
α	Curvilinear coordinates defined by shock front or surface
β	Curvilinear coordinates defined by normal trajectories or 'rays'

γ	Ratio of specific heat
θ	Angle between ray and x-axis
μ	Mach number of moving shock with respect to flow behind the shock
ρ	Density

1 Introduction

1.1 Background

When a normal shock wave travelling down a channel encounters a section of variable area the strength and shape of the shock, as well as the flow behind the shock are disturbed. Where a decrease in cross-sectional area exists the shock is expected to strengthen and the average speed of the shock increases. And conversely, for an enlargement in cross-sectional area the shock is weakened and the average speed of the shock decreases. This is of particular interest in engineering where internal pipe flows with sudden or gradually varying sections of pipe diameter are common. In such systems it becomes useful to understand and predict the transient behaviour of a propagating shock and the subsequent flow characteristics in order to utilize or minimize their effects.

The field of shock wave dynamics is the study of shock wave phenomena such as propagation, diffraction, reflection and refraction through means of theoretical analysis, numerical calculations or experimental methods. Han and Yin (1993) categorises the various types of transient problems into a shock wave propagating into a quiescent 'still' gas or a moving gas. For the case of a shock propagating into a uniform quiescent gas Chester (1954), Chisnell (1957) and Whitham (1958) individually obtained a similar relation using different methods to relate the shock Mach number (M) and the cross-sectional area of a tube (A). The relation derived is commonly referred to as the CCW relation and it provides a quasi one–dimensional analysis of the shock. Later, Whitham (1957, 1959) expanded the study and derived a more generalized form of the CCW relation which relates 'ray tube' area in a flow field to the shock Mach number. Whitham also went on to develop a set of two- and three dimensional equations which form the basis for geometrical shock dynamics. Whitham's theory, as it is known, is particularly successful at predicting shock characteristics at higher Mach numbers ($M > 2$) but as mentioned by Skews and Kleine (2010) can be unreliable at lower Mach numbers. This highlights an important issue with previous theoretical models in that the theory ignores the influence of the flow behind the shock where the reflected and re-reflected disturbances may interfere with the shock front. In order to account for the re-reflected disturbances several authors have studied this problem further and added correction terms to the CCW relation.

From an experimental approach, Bird (1959) investigated the interaction between normal shock waves and several symmetrical converging nozzle designs, and Russell (1967) investigated shock wave strengthening by area convergence. Both Bird and Russell conducted their experiments at relatively high Mach numbers of between Mach $2.3 - 5.75$. Bird showed that by optimising the wall shape, an area reduction can be used to increase the strength of a shock significantly without compromising on the quality of the post-shock flow. Practically, this means an area reduction can be used in experimental shock tube set-ups to increase the strength of the initial shock without increasing energy requirements. More importantly, by analysing different profiles using numerical studies, the technique could then potentially be generalized to examine to what extent a shock may be manipulated to a certain shape. Finally, from a numerical approach several authors such as Igra et al. (1994, 1998) and Henshaw et al. (1986) have studied this problem but Igra et al. (1998) notes that an expanded understanding of Mach-area relations still needs to be achieved by combining more detailed one-/two dimensional computations with experimental observations.

1.2 Motivation

It is clear that experimental results agree well with theoretical predictions at relatively high Mach numbers but further work is still required at lower Mach numbers where the strength of reflected disturbances are comparable to that of the incident shock. Furthermore, few papers exist analysing shock wave strengthening via gradual area reductions utilizing clear experimental images and then comparing these to theoretical and numerical calculations. Work conducted by Khan and Skews (2009) look at optimization of an area reduction by minimizing losses, and will be used as a basis for this research, as well as recent advances in experimental techniques by Skews and Kleine (2008) which provide a means in which to analyse the affect of the reflected disturbance waves from different profile shapes.

2 Objectives

The following objectives have been proposed for this research project.

- Investigate the possible wave amplification that can be achieved by designing optimised wall shapes in order to minimize losses from reflected disturbances.
- Analyse the development and relaxation of the shock and post-shock flow during and after the area change and compare how long it takes for both to fully stabilize for different wall profile shapes.
- Investigate the effect of re-reflected disturbances on the shock front for varying shock strengths, and compare the results with the assumption of the CCW relation and Whitham's theory.

}

3 Literature Survey

This chapter provides an overview of the theoretical, numerical and experimental studies on the effects that area changes have on shock waves. Sections 3.1 to 3.3 cover the definition of the Mach-area relation and how it is applied to Whitham's (1957, 1959) ray–shock theory and Henshaw et al.'s (1986) numerical time-marching scheme. Finally, section 3.4 covers previous experimental papers analysing shock wave strengthening by area convergence.

3.1 Mach – Area Relation

Figure 3.1 shows an approximate description of the motion of a planar shock wave moving through a channel consisting of two uniform sections joined by a section of varying area. As the shock wave propagates through the area change the strength of the incident shock changes continuously and reflected disturbance waves and contact surfaces are generated (Han and Yin, 1993).

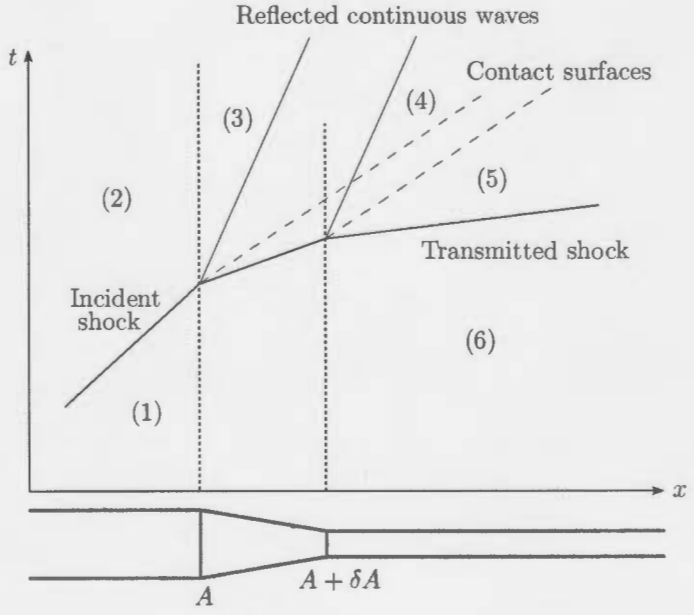

Figure 3.1: Planar shock moving along a tube with a small change in area, derived from Han and Yin (1993, p. 25).

Chester (1953, 1954) analysed this problem and assumed that if the area of the channel changes by a small fraction of itself, the disturbances produced in the flow behind the shock are regarded as negligible and thus the equations of motion for the one-dimensional case could be linearized. Thus an approximate first-order relationship was determined between the channel area A and the corresponding shock

strength z which may be used for finite continuous area changes. Although the shock is not uniform across the channel after entering the area change, by assuming that the pressure over the cross-section of the tube eventually becomes uniform, an average pressure was used to significantly simplify the analysis. Chester also noted that, ultimately, the disturbances or perturbations depend only on the variation in the area of the tube and not on the actual shape of the cross-section.

The approximate solution derived by Chester (1954) was also derived by Chisnell (1957) using steady state theory across the six regions shown in the $x-t$ diagram in figure 3.1. Similarly, Chisnell assumed that the effect of the reflected disturbances generated by the shock may be neglected and considered only after the final flow conditions where any flow disturbances have subsided. Chisnell obtained the following equation,

$$\left.\begin{aligned} -\frac{1}{A}\frac{dA}{dz} = \frac{1}{\gamma z} + \frac{1}{(z-1)} - \frac{(\gamma+1)}{2\{(\gamma+1)z+(\gamma-1)\}} \\ + \left[\frac{2}{\gamma z\{(\gamma-1)z+(\gamma+1)\}}\right]^{1/2} \\ \times \left[1 - \frac{(\gamma+1)(z-1)}{2\{(\gamma+1)z+(\gamma-1)\}} + \frac{(\gamma-1)z+(\gamma+1)}{2(z-1)}\right] \end{aligned}\right\} \qquad [3.1]$$

where A is the cross-sectional area of the tube and z is the shock strength and is defined as the pressure ratio across the shock, $z = p_2/p_1$. Ben-Dor et al. (2001) notes that [3.1] is only valid for long times after the initial shock wave has passed through the area change segment in the duct. Chester (1954) provides an equivalent formula to [3.1] with the right-hand side of the equation written as $\{(z-1)K(z)\}^{-1}$, where $K(z)$ is a decreasing function of shock strength with a small total variation and decreases from 0.5 (weak shocks) to approximately 0.394 (strong shocks) for $\gamma = 1.4$. The integration of [3.1] gives the shock strength/area relation,

$$A \cdot f(z) = \text{constant}, \qquad [3.2]$$

where,

$$f(z) = z^{1/\gamma}\cdot(z-1)\cdot\left(z+\frac{\gamma-1}{\gamma+1}\right)^{-1/2}\cdot\left[\frac{1+R}{1-R}\right]^{\sqrt{\gamma/2(\gamma-1)}}\cdot\left[\frac{R-\left(\frac{\gamma-1}{2\gamma}\right)^{1/2}}{R+\left(\frac{\gamma-1}{2\gamma}\right)^{1/2}}\right]$$
$$\times\exp\left[\left(\frac{2}{\gamma-1}\right)^{1/2}\cdot\tan^{-1}\left\{\frac{2\gamma^{1/2}R}{\gamma-1}\right\}\right]$$

and,

$$R = \left\{1+\frac{(\gamma+1)}{(\gamma-1)\cdot z}\right\}^{-1/2} \qquad z = \frac{2\gamma}{\gamma+1}\cdot M^2 - \frac{\gamma-1}{\gamma+1}$$

Whitham (1958) uses a simpler linearized characteristics approach to this problem and his elegant procedure is called 'Whitham's Rule'. When a shock moves through a tube of variable area the two families of characteristics, as shown in figure 3.2, result. Han and Yin (1993) explains, that physically the negative characteristics (C^-) are generated by the variable shock strength and are reflected disturbance waves travelling back into the flow – Whitham (1958) assumes that if a reflected shock wave is formed it does so outside the region under consideration. The positive characteristics (C^+) have the same direction as the incident shock and only play a subsidiary role when neglecting the effect of re-reflected disturbance waves. Finally, entropy changes are carried along the particle paths (P) and interestingly p and u do not directly depend on them.

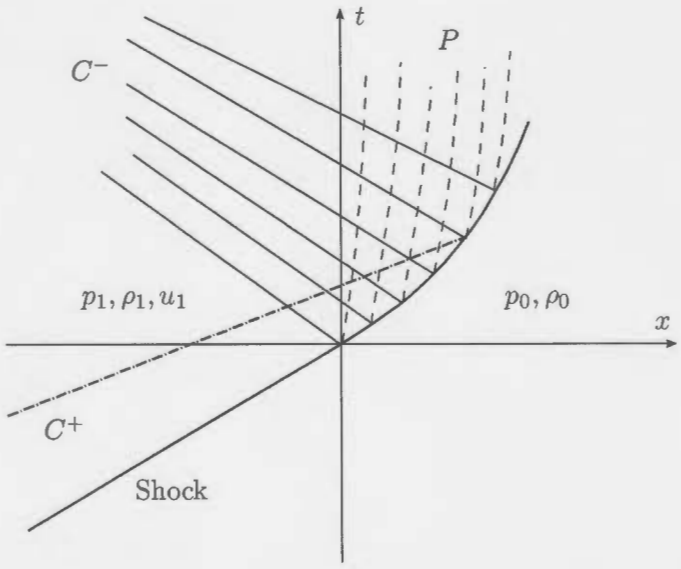

Figure 3.2: The x–t plane for the interaction of a shock wave with an area change

By applying the non-linear differential relation for the C^+ characteristics and substituting the expressions for p,ρ,u and a in terms of M, the resulting differential relation derived by Whitham is given by,

$$\frac{2M}{(M^2-1)}\frac{dM}{K(M)}+\frac{dA}{A}=0, \qquad [3.3]$$

where,

$$K(M)=2\left[\left(1+\frac{2}{\gamma+1}\frac{1-\mu^2}{\mu}\right)\left(2\mu+1+M^{-2}\right)\right]^{-1}$$

and,

$$\mu^2=\frac{(\gamma-1)M^2+2}{2\gamma M^2-(\gamma-1)}$$

It is an approximate differential solution that relates the shock Mach number and the cross-sectional area of a channel. It follows that relation [3.3] is similar to [3.2] and has been referred to as the Chester–Chisnell–Whitham relation or the CCW relation. Whitham (1958) presumes that the results would only be valid for flows that encounter a change in area that is 'slowly varying' but notes that the precise definition of 'slowly varying' is unclear. Importantly, it is described as an 'approximate solution' because it negates the effect of re-reflected disturbances from the subsequent flow. The integration of [3.3] can be written as follows,

$$A = C\exp\left[-\int \frac{2MdM}{(M^2-1)\,K(M)}\right] = Cf(M)$$

Letting $C = \dfrac{A_0}{f(M_0)}$ we have,

$$\frac{A}{A_0} = \frac{f(M)}{f(M_0)} \qquad [3.4]$$

where,

$$\begin{aligned} f(M) = \exp\Bigg\{-\Bigg\{ & \ln\left(\frac{M^2-1}{M}\right) + \frac{1}{\gamma}\ln\left(M^2 - \frac{\gamma-1}{2\gamma}\right) \\ & + \ln\frac{1-\mu}{1+\mu} + \left(\frac{\gamma-1}{2\gamma}\right)^{\frac{1}{2}} \ln\left[\mu + \left(\frac{\gamma-1}{2\gamma}\right)^{\frac{1}{2}}\right] \\ & - \left(\frac{\gamma-1}{2\gamma}\right)^{\frac{1}{2}} \ln\left[\mu - \left(\frac{\gamma-1}{2\gamma}\right)^{\frac{1}{2}}\right] \\ & + \left[\frac{2}{\gamma(\gamma-1)}\right]^{\frac{1}{2}} \ln\left[\left(M^2 + \frac{2}{\gamma-1}\right)^{\frac{1}{2}} + \left(M^2 - \frac{2}{\gamma-1}\right)^{\frac{1}{2}}\right] \\ & + \left[\frac{1}{2(\gamma-1)}\right]^{\frac{1}{2}} \tan^{-1}\left\{\frac{\left[4\gamma - (\gamma-1)^2\right]M^2 - 4(\gamma-1)}{4\gamma^{\frac{1}{2}}(\gamma-1)\left[M^2 + \frac{2}{\gamma-1}\right]^{\frac{1}{2}}\left[M^2 - \frac{\gamma-1}{2\gamma}\right]^{\frac{1}{2}}}\right\}\Bigg\}\Bigg\} \end{aligned}$$

If the initial shock is very strong ($M \to \infty$) or very weak ($M \to 1$), or the change of shock strength in a narrow region may be regarded as constant, equation [3.4] can be written as follows by equation [3.5] (Han and Yin, 1993). Equation [3.5] is a simple relation for engineering calculations but the results should only be considered a rough estimate.

$$A\left(M^2-1\right)^{\frac{1}{K}} = \text{constant} \qquad [3.5]$$

For strong shocks $K = 0.3941$ ($\gamma = 1.4$), and for weak shocks $K = 0.5$.

It is clear that due to the assumptions made the CCW relation does not account for the effect that the post-shock flow has on the shock as it passes through a variable area. Also, Whitham (1958) notes the possibility that small disturbances may accumulate over a large region and become significant. Several authors such as Rosciszewski (1960) and Oshima (1965) have studied this problem further and provided correction terms to account for the re-reflected disturbances. Milton (1975) provides a simple modified version of the CCW relation by including a correction term as shown here,

$$\frac{dA}{A} = -\left[\frac{2M}{K(M)(M^2-1)} + \frac{\eta}{M}\right] dM \qquad [3.6]$$

where $K(M)$ is the same as in relation [3.3], and

$$\eta = \frac{1}{2\gamma}\left\{\left[\frac{\gamma(\gamma-1)}{2}\right]^{\frac{1}{2}} + 1\right\}\left\{1 - \left(\frac{M_0}{M}\right)^2\right\} + \frac{1}{2}\ln\frac{A_0}{A}.$$

Milton and Archer (1996) found that Milton's modified version provided a significant improvement in results from the original CCW relation. Itoh et al. (1981) further revised Milton's results and provides a more complex expression for η, but no noticeable further improvement was found by Milton and Archer using the more complicated correction factor by Itoh et al..

3.2 Geometrical Shock Dynamics

As mentioned, the CCW relation provides an approximate relationship between the Mach number and the cross-sectional area, but it cannot predict the change in shape of a shock over the course of the area change. For this reason, Whitham (1957, 1959) developed an approximate theory for shock propagation to predict the strength and shape of a shock in two- and three-dimensions. In this theory, the motion of the shock is determined using geometrical shock dynamics where the shock positions are defined by the family of curves α =constant. The shock propagates on 'rays' normal to the shock front and are defined by the curves β =constant. This forms a grid of (α, β) coordinates as shown in figure 3.3 where ray inclination (θ) is measured with respect to the x–axis. A 'ray-tube' is defined by two adjacent rays and it is assumed that each ray-tube area may be treated as an independent problem of shock propagation in a tube with solid walls (Whitham, 1974).

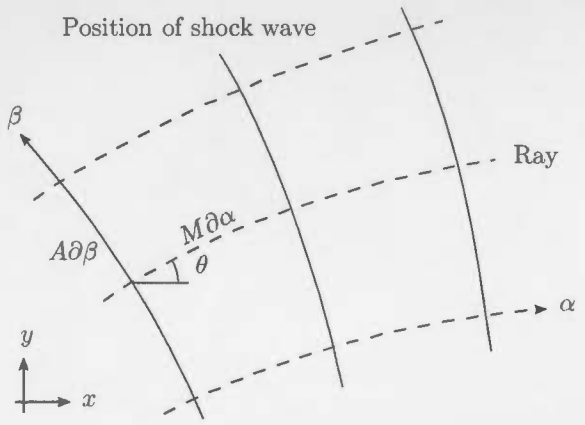

Figure 3.3: Shock positions given by α =constant (solid lines) and rays given by β =constant (dashed lines)

The shock position at any given time is specified by $\alpha = a_0 t$, where a_0 is the undisturbed sound speed. When figure 3.3 is analysed geometrically a geometrical relationship of shock dynamics is obtained [3.7].

$$\frac{\partial}{\partial \alpha}\left(\frac{1}{M}\frac{\partial A}{\partial \alpha}\right) + \frac{\partial}{\partial \beta}\left(\frac{1}{M}\frac{\partial A}{\partial \beta}\right) = 0 \qquad [3.7]$$

By assuming that each ray-tube is analogous to a simple solid tube wall, Whitham extends the application of the $M - A$ C.C.W. relation to each ray-tube individually. Han and Yin (1993) note that an approximation may be required when considering that a particle path further away from the shock front may deviate from the ray. By substituting the Mach – area relation $A = A(M)$ into [3.7] the following second-order hyperbolic equations are obtained,

$$\frac{\partial \theta}{\partial \beta} - \frac{A'(M)}{M}\frac{\partial M}{\partial \alpha} = 0, \qquad [3.8]$$

$$\frac{\partial \theta}{\partial \alpha} + \frac{1}{A(M)}\frac{\partial M}{\partial \beta} = 0, \qquad [3.9]$$

By introducing a speed of disturbance, $c(M)$, equations [3.8] and [3.9] can be written in characteristic form:

$$\theta + \int \frac{dM}{Ac} = \text{constant on } \frac{\partial \beta}{\partial \alpha} = c, \qquad [3.10]$$

$$\theta - \int \frac{dM}{Ac} = \text{constant on } \frac{\partial \beta}{\partial \alpha} = -c. \qquad [3.11]$$

$$\text{where,} \qquad c(M) = \sqrt{\frac{-M}{AA'}} \qquad [3.12]$$

The expressions $\theta \pm \int dM/Ac$ correspond to the Riemann invariants of one dimensional unsteady flow and $c(M)$ is the speed of non-linear disturbance waves propagating on the shock in the (α, β) plane. Physically, Whitham (1974) equates this to two-dimensional waves propagating with the local sound speed relative to the flow as shown in figure 3.4.

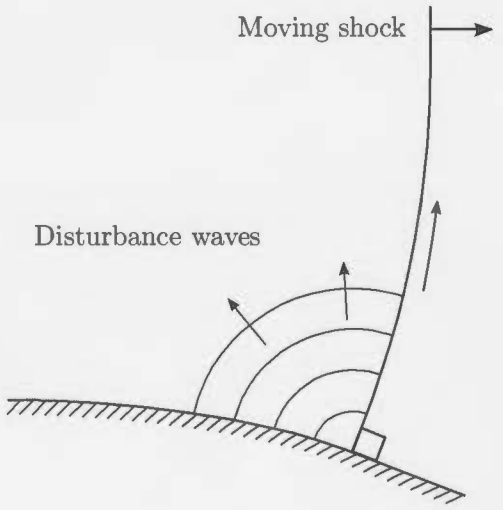

Figure 3.4: Cylindrical waves propagating along the shock front during the diffraction of a shock

Since the speed for a disturbance wave on the shock is an increasing function of M, the profile of a wave carrying an increase in Mach number will steepen like a compression wave (Whitham, 1957). Similarly, a wave carrying a decrease in Mach number will expand as is expected in gas dynamics. In the former case, it is typical for the flow to transition to Mach reflection and Whitham labels the discontinuity in Mach number and slope at the triple-point as the 'shock–shock'. In the case of a shock propagating along a boundary wall, the wall itself is defined as both a ray and a particle path which enforces the shock front to be orthogonal to the boundary wall. As such, any changes in upstream boundary conditions results in a disturbance wave propagating along the shock front carrying information about the change in slope and Mach number of the shock.

3.3 Numerical Analyses of Geometrical Shock Dynamics

There has been continued interest in numerical analysis of shock wave propagation in order to predict a shock's motion and provide validation to analytical models.

Most recently, accurate computational methods to solve the unsteady Euler equations of gas dynamics Igra et al. (1994) studied the difference between the Random Choice Method (RCM) numerical scheme and Whitham's approximation for a shock wave interacting with various area changes. Igra et al. concluded that Whitham's area rule may be used for estimating the flow behind a normal shock wave propagating in a duct, in which a monotonic smooth area reduction exists, provided that the area reduction ratio and the incident shock Mach number are relatively small. Furthermore, Igra et al. found that the error in pressure was less than 8% for an initial shock of $M_0 \leq 2$ and area reduction ratio (ratio of duct inlet to duct outlet) of $A_{\text{inlet}}/A_{\text{outlet}} \leq 2$.

Igra et al. (1998) presented a comparative study for area reductions between a quasi one-dimensional generalized Riemann problem (GRP) scheme and a two-dimensional Euler solution. Igra et al. observed that although in some cases the two-dimensional results did approach the respective one-dimensional approximations a over a long period of time, there were cases where the solution could not reduce to a one-dimensional equivalent due to the complexity of flow features produced.

Henshaw, Smyth and Schwendemen (1986) describe a numerical shock-fitting scheme that is based on Whitham's (1957) two-dimensional theory of geometrical shock dynamics. This approach differs from Igra et al. (1994, 1998) in that Henshaw et al. considers only the motion of the shock and not the details of the flow field behind it. The numerical scheme is based on a leap–frog time marching scheme of a discrete set of points describing the shock front as illustrated in figure 3.5.

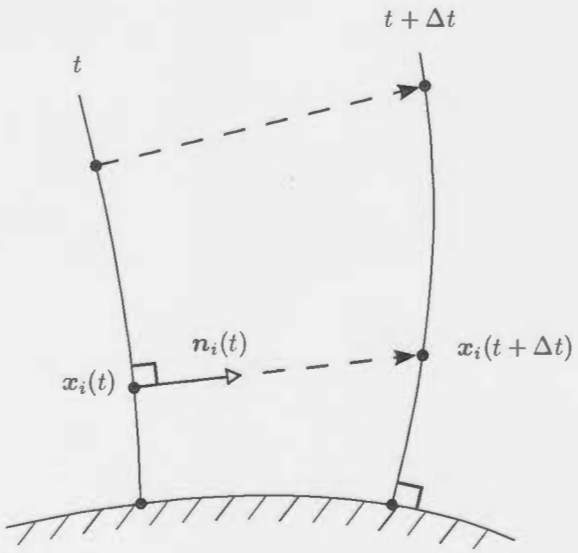

Figure 3.5: Time-marching scheme for shock front positions at t and $t + \Delta t$ (solid lines) and approximate rays (dashed lines)

The position of $\boldsymbol{x}_i(t+\Delta t)$ is calculated using the following two-step leap–frog scheme,

$$\boldsymbol{x}_i(t+\Delta t) = \boldsymbol{x}_i(t-\Delta t) + 2\Delta t M_i(t)\boldsymbol{n}_i(t), \qquad i = 1,\ldots,N, \qquad [3.13]$$

where $\boldsymbol{x} = (x, y)$ is the shock front position, $\boldsymbol{n} = (\cos\theta, \sin\theta)$ is the normal to the shock front, and $t = n\Delta t$, $n = 0,\ldots,T/\Delta t$. This two-step leap frog scheme is explicit, second-order accurate and provides no numerical dissipation. In general, scheme [3.13] is solved numerically using the Mach–Area relation (CCW Relation), but if the shock is strong or weak then the approximate relation [3.5] can be used to solve for $M_i(t)$ explicitly. The approximate area $A_i(t)$ is calculated from arc-lengths along the shock front centered about each discrete point and a one-sided scheme at the boundary points. In the theory of shock dynamics, since the boundary wall coincides with rays, all line segments at the boundary wall are adjusted to be normal to the wall. In cases where the shock tends to expand outward, points are added to maintain good shock front resolution and shock-shocks are fitted in compressive regions by deleting points. Finally, in order to dampen high-frequency numerical oscillations a smoothing scheme is applied. Figure 3.6 shows a sample of results obtained by Henshaw et al. (1986) of successive shock front positions for the case of shock wave diffraction by a 30° smooth concave wall. Figure 3.6 shows how the numerical scheme is able to track (as the shock is being compressed) the gradual formation of the shock-shock or transition to Mach reflection.

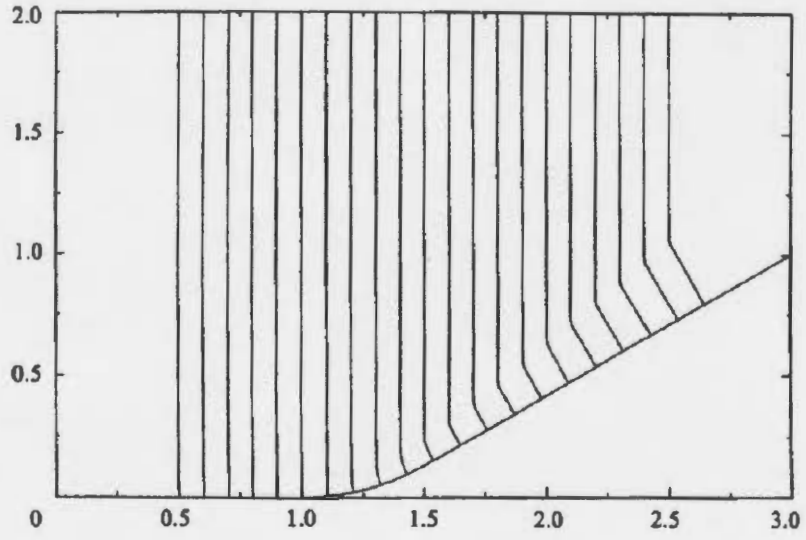

Figure 3.6: Sample results from Henshaw et al. (1986) for diffraction by a 30° circular concave wall

3.4 Experimental Analyses of Shock Wave Strengthening

Since Chester (1953, 1954), Chisnell (1957) and Whitham (1958) each derived the Mach–Area relation, a number of authors have investigated the effect of shock wave strengthening by area convergence experimentally in order to compare results obtained against the one-dimensional predictions.

3.4.1 Summary of Bird's (1959) experimental results

Bird (1959) investigated the interaction between normal shock waves and several symmetrical converging nozzle designs. Bird tested seven different converging nozzle designs, each with an area ratio of contraction of $9.9:1$, with tests carried out with an incident shock speed of between Mach $2.3-2.5$. The incident and transmitted shock strength, z, were calculated based on equation [3.14]. An estimate for the shock speed, q was calculated using the optical reduction of the schlieren system and the known rotational speed of the drum camera. Table 3.1 shows summarised results for the seven nozzle blocks tested for the mean percentage increase in shock wave strength.

$$z = \frac{2\gamma}{\gamma+1}\left(\frac{q}{a}\right)^2 - \frac{\gamma-1}{\gamma+1}, \qquad [3.14]$$

Table 3.1: Summarised results of experiments by Bird on interaction between normal shock waves and converging nozzle blocks

No.	Shape	Description	Mean Increase in Shock Strength (%)
1		90°, sharp corner	25
2		90°, 0.1H radius corner	29

3		90°, 0.2H radius corner	33
4		Quadrant shaped	72
5	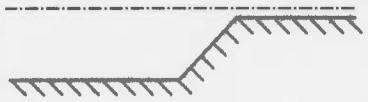	45°, straight	87
6		15°, straight	121
7		15°, rounded	130

The benefits of increasing the number of steps for an area reduction can be seen clearly in Table 3.1 where a discontinuous area change provided a 25% increase in shock strength, compared to a 130% increase for a gradual 15°, rounded reduction – a five times improvement in shock strength at the convergence exit. Bird concluded that the degree of shock wave strengthening depends critically upon the wall shape. Furthermore, given the theoretical maximum gain in shock strength calculated from Chisnell (1957), the gain in shock strength continues to increase with the number of steps until the ideal limiting case of an infinite number of vanishingly small changes in area is reached. Finally, Bird concluded that shock tubes could well incorporate a converging section in order to achieve the strongest possible waves, but care would have to be taken in the positioning of such an area reduction to ensure that reflected waves from the area change do not overtake the primary shock.

3.4.2 Summary of Russell's (1967) experimental results

Russell (1967) investigated shock wave strengthening by area convergence experimentally and compared his results with those from the C.C.W. model. He analysed a planar shock wave propagating down a 17 inch shock tube through to a 1 inch

tube with a 10° convergence cone as shown in figure 3.7.

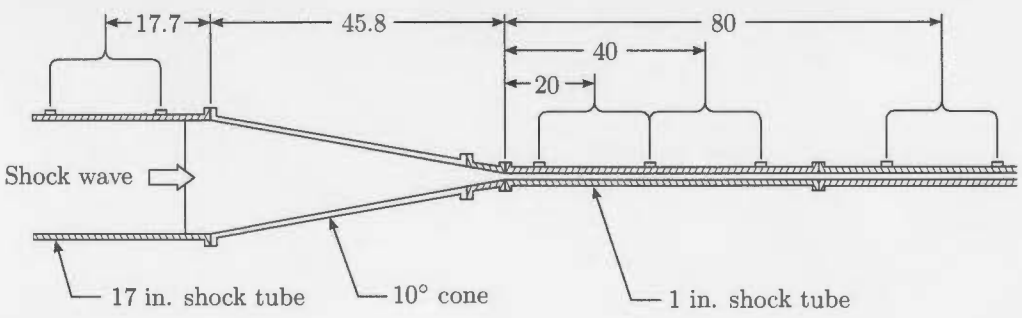

Figure 3.7: Illustration of Russell's (1967) test rig involving a 17 inch shock tube coupled by a 10° half-angle cone to a 1 inch diameter tube

The tests were conducted at relatively high Mach numbers of between Mach 2.75–5.75. Results depicted in 3.8(a) showed that the shock waves emerged from the convergence two to three times their entrance speeds and then proceeded to decelerate down the 1 inch shock tube. After applying a correction factor accounting for viscous attenuation, Russell found that strengthened shock speeds at the exit of the convergence agreed to within 5% of results obtained from the CCW model. Russell also analysed the decay rate of shock of the shock in the converged section as shown in figure 3.8(b). In general, Russell found that results were in good agreement with the non-steady and characteristic calculations. Russell suggested that the two-dimensional effects are of limited importance, at least for convergence cone half-angles under 30°.

3.4.3 Summary of Khan and Skews' (2009) experimental results

Khan and Skews (2009) investigated the optimisation of an area reduction within a duct in order to minimize the losses associated with the formation of Mach reflections for a planar shock propagating through it. A sinusoidal curve was chosen to define the basic shape of the profile because it provides a smooth transition from initial to final area. An initial computational fluid dynamic (CFD) analysis was conducted implementing a two-dimensional, density-based, inviscid solver and involving parameters of total length, curvature and height. From these results, aluminium profiles of 30%, 35% and 40% reduction in area, each with total length of 270mm, were manufactured and tested experimentally.

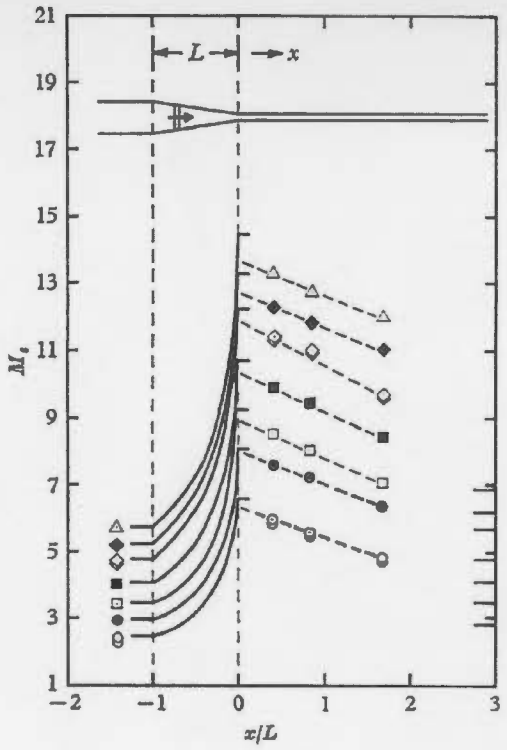

(a)

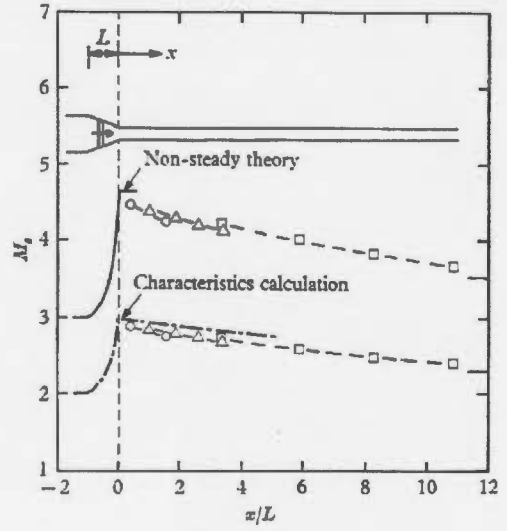

(b)

Figure 3.8: (a) Corrected data showing shock strengthening compared with non-steady theory for *real* air. (b) Corrected data showing shock decay compared with non-steady theory and one-dimensional characteristics calculation

Figure 3.9(a) shows a sample set of images captured using a mono-chrome shadowgraph optical setup for a profile with a 30% reduction in area where tests were

carried out at $M_i = 1.42$. A second set of CFD simulations were conducted and provided a selection of three final profiles of 50%, 60% and 70% reduction in area. Figure 3.9(b) shows a Mach 1.42 shock propagating through a profile with a 70% area reduction with $45\mu m$ perturbation sources. Khan and Skews showed that even with a 70% reduction in area the shock did not transition to Mach reflection, instead only strong compressions can be seen traversing the shock front and reflecting off the upper test section wall.

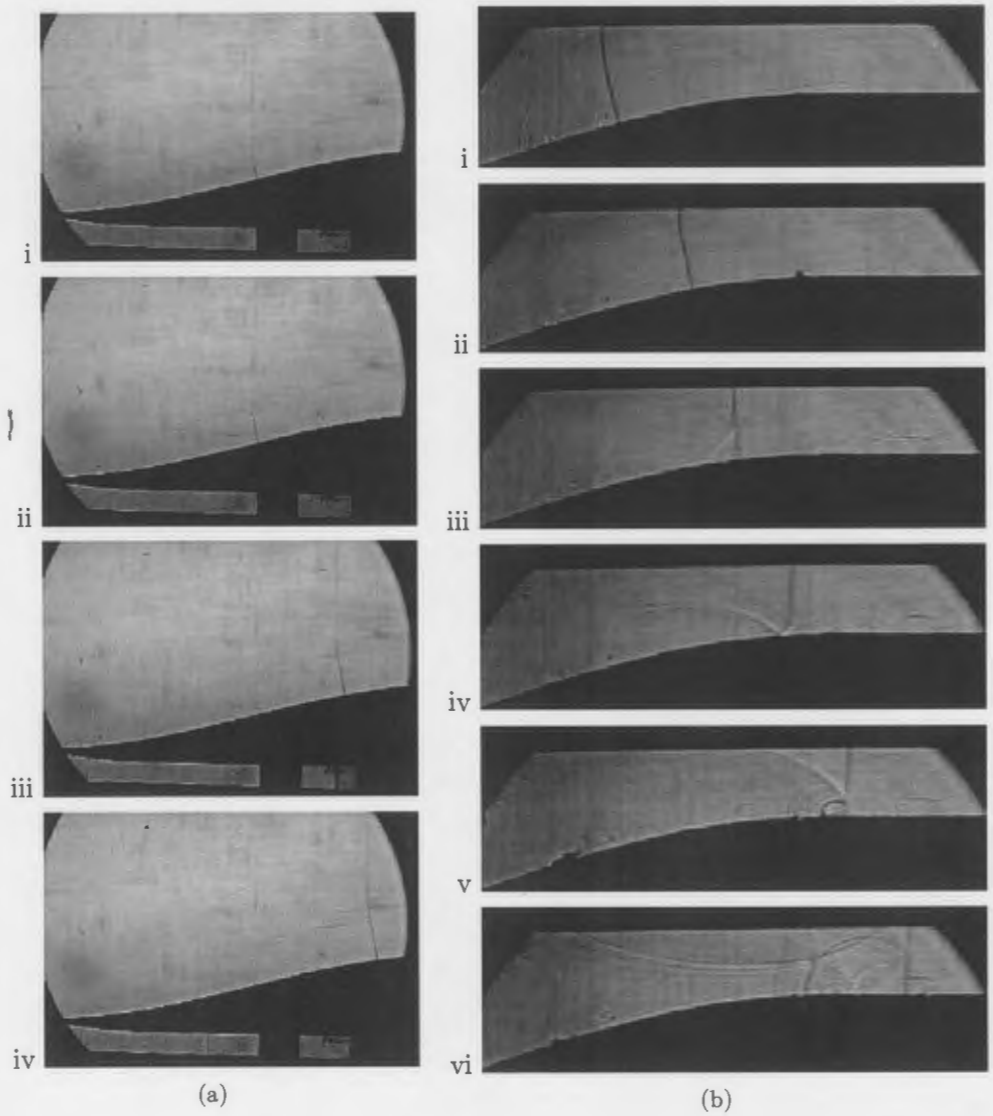

Figure 3.9: Experimental results from Khan and Skews (2009) for (a) 30% and (b) 70% reduction in area where $M_i = 1.42$

4 Experimental Methodology

4.1 Overview

The research was split into three main sections where numerical, experimental and analytical studies were conducted. A summarised list of the research methodology is provided below.

(a) *Initial numerical study*

A preliminary computational fluid dynamic (CFD) study was conducted to provide a basis for the profile design of the models for experimental testing. Results from Khan and Skews (2009) were used for initial profile and flow parameters.

(b) *Experimental study*

Aluminium profiles manufactured from the wall profiles chosen from the preliminary CFD analyses were tested using the Michael Seitz (2001) shock tube. Schlieren and shadowgraph flow visualization techniques were used together with captured pressure data.

(c) *Revised numerical study*

Results from the preliminary CFD analysis were revisited and mesh refinement criteria were improved to highlight certain flow features based on the observations of the experimental results. To provide an additional numerical analysis, a two-dimensional shock–tracking numerical scheme based on Milton's (1975) modified Whitham's Theory and Henshaw et al.'s (1986) time-marching shock–fitting scheme was created.

(d) *Analytical study*

Results produced from experimental and numerical studies are compared directly to theoretical predictions using the CCW Relation and modified versions of Whitham's theory of shock dynamics.

4.2 Numerical Studies

The numerical studies were conducted at three stages of the research: an initial set of CFD simulations providing a low-level analysis of the flow system to determine any noticeable flow features or areas of interest; a second set of simulations looked

at refining the initial CFD findings to duplicate any unresolved, observable features found in the experimental results; and finally simulations were conducted using a numerical scheme developed in MATLAB for comparison against the aforementioned CFD simulations.

4.2.1 Numerical domain

The numerical domain and initial flow conditions chosen for the initial and revised CFD simulations were chosen based on Khan and Skews's (2009) results for their final optimized profile. The wall profile that Khan and Skews used consists of a single sinusoidal curve with an area reduction of either 50%, 60% or 70%. Figure 4.1 shows the domain used for computations for the largest percentage of area reduction of 70%.

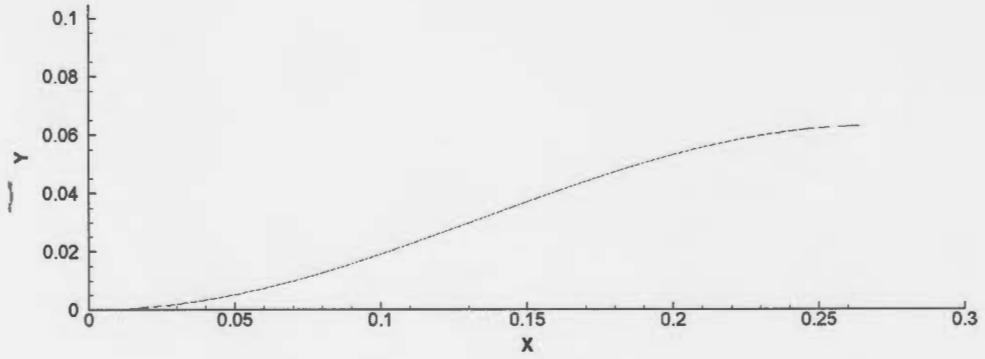

Figure 4.1: Sinusoidal curved profile with 70% area reduction used by Khan and Skews (2009) for numerical analyses

The domain consists of two simple boundary walls (the wall profile and the upper wall) and non-reflecting pressure inlet and outlet. Although a trigonometric function such as a sinusoidal curve provides a smooth transition from one point to another, the gradient of the function changes constantly. Additionally, it becomes difficult to alter the shape of the trigonometric curve for future analysis, for example; on the effect of an asymmetric profile on shock wave strengthening. As such, in figure 4.2 two parabolic curves (f and g) joined at a movable inflection point was chosen to define the wall profile from area A_1 to A_2. The area ratio is defined as the percentage by which the area is reduced and is defined by,

$$AR = \frac{A_1 - A_2}{A_1} \times 100\%. \qquad [4.1]$$

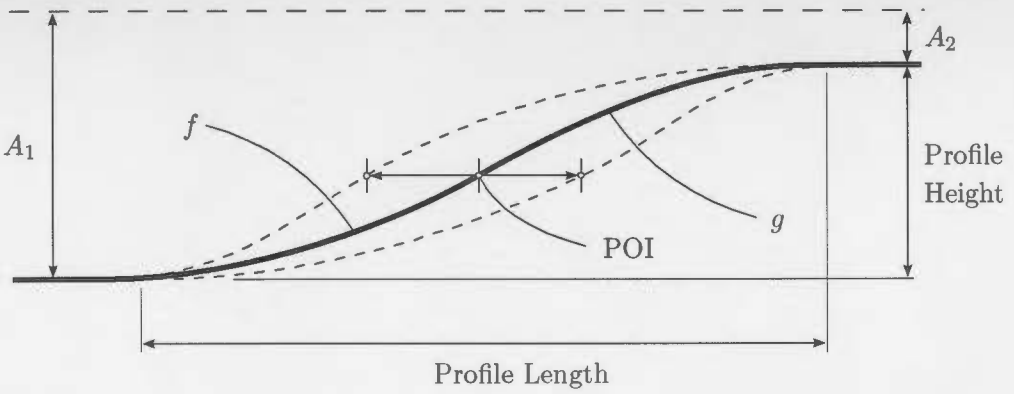

Figure 4.2: Description of the curve defining the wall profile consisting of two parabolic curves f and g intersecting at the point of inflection (POI)

The higher the percentage in area reduction of the profile; the smaller the profile exit area A_2.[1] When the point of inflection (POI) is central between the profile entrance and exit, the shock propagating down the profile length sees a constant change in the wall gradient, i.e. $f'' = \text{constant}$. By moving the POI to the left (upstream) or to the right (downstream) the shock propagating down the length of the profile will undergo varying rates of compression.

Considering the combination of parameters that can be used to define the profile and inlet conditions from figure 4.2, the following geometrical and flow parameters in table 4.1 were chosen based on comparability with previous research as well as restrictions with available experimental testing facilities (see Section 4.3.2 for details on the chosen testing facility).

Table 4.1: Parameters used for preliminary numerical simulations

Parameter Description	Unit	Chosen Value
Inlet height:	mm	120
Profile length:	mm	130, 195, 260
Percentage reduction in area:	(%)	40, 60, 80, 90, 95
Point of inflection:	(%)	25, 50, 75
Initial inlet Mach number:	-	1.2, 1.4, 1.6, 1.8

Two main cases were simulated for each of the profile lengths. The first case depicted in figure 4.3 consists of a half profile reduction with a symmetry boundary enforced on the upper plane. The shock is initialised from a pressure inlet located 100mm upstream of the profile start and a pressure outlet 200mm downstream of the profile

[1] The definition of the calculated area reduction is important to note as various authors define this term differently.

end allows the shock to pass freely through. The initial straight section of 100mm is incorporated into each simulation to ensure the shock is properly developed and uniformly refined as it encounters the leading edge of the profile.

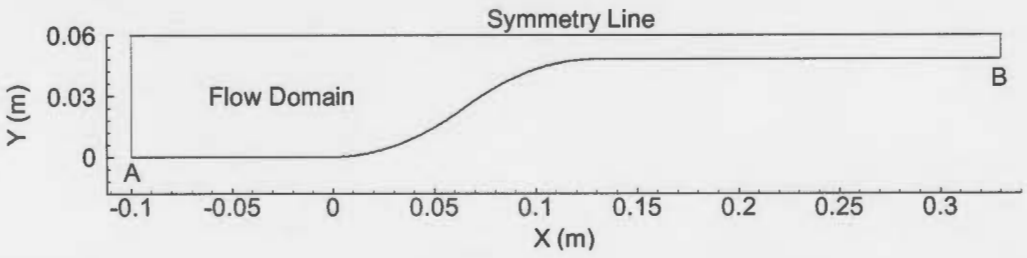

Figure 4.3: Computational domain used for typical simulations of shock travelling through area reduction and through the reduced section

At the beginning of each case the rest of domain is initialised to one atmosphere or 101325kPa. The parabolic curve defining the profile $P(x)$ is defined by equation [4.2] where H = Profile height, L = Profile length, Q = Horizontal distance to point of inflection.

$$p(x) = \begin{cases} f = ax^2 & \text{if } 0 < x < Q \\ g = bx^2 + cx + d & \text{if } Q \leq x < L \end{cases} \qquad [4.2]$$

where,

$$a = \frac{H}{LQ}, \qquad b = \frac{H}{L(Q-L)}, \qquad c = \frac{-2H}{Q-L}, \qquad d = \frac{Hq}{Q-L}.$$

The second case is setup similarly to the first case instead the pressure outlet is extended 1000mm downstream of the profile end. These 'extended profile simulations' are setup to track the shock decay as the shock progresses down the reduced section of the tube after the profile reduction. The focus of these extended profile simulations is to determine how much influence (if any) the profile length would play in the shock Mach number and its decay over the extended length.

4.2.2 Solution method

CFD simulations were carried out in ANSYS Fluent 12.0 using an inviscid, second order, implicit, density-based solver. The flow was modelled using an explicit third order MUSCL scheme with Roe-Flux Difference Splitting scheme where the domain was meshed using the least-squares, cell-based spatial discretization technique.

The specifications for the computer hardware and software used to do the numerical calculations are listed in table 4.2.

Table 4.2: CFD equipment specifications

Specification	Detail
CPU:	Intel Core i7 2.8GHz
RAM:	6GB
Graphics card:	512MB DDR3 GeForce video card
Operating System:	Microsoft Windows 7 Professional
CFD Software:	ANSYS Fluent 12.0

4.2.3 Mesh structure

Quadrilateral and triangular mesh structures were compared and a mapped quadrilateral mesh was chosen due to its better computational efficiency whilst producing similar results. Figure 4.4 shows an example of the mapped quadrilateral mesh structure with an average initial cell size of 2mm, whereas figure 4.5 shows the triangular mesh with an average initial cell size of 2mm.

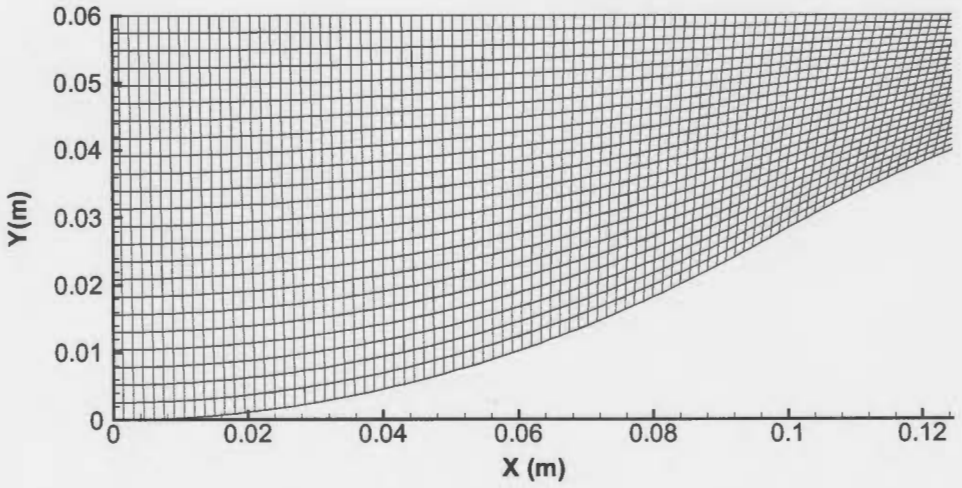

Figure 4.4: Rough quadrilateral mesh used for preliminary simulations showing typical initialized cell size

The mesh was adaptively refined up to five times in regions where pressure and Mach number gradients exceed 10% of the local normalized value. For the revisited CFD simulations initial cell size was reduced to 0.2mm in order to adequately capture shock curvature and possible shear layer development. Figure 4.6 shows an example of the finer mapped quadrilateral mesh.

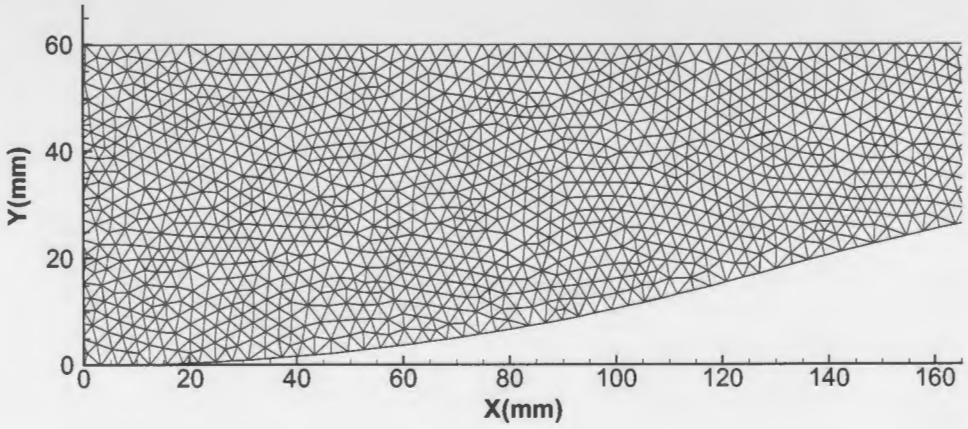

Figure 4.5: Triangular mesh used for a simulation for a 260mm profile to confirm mesh independence

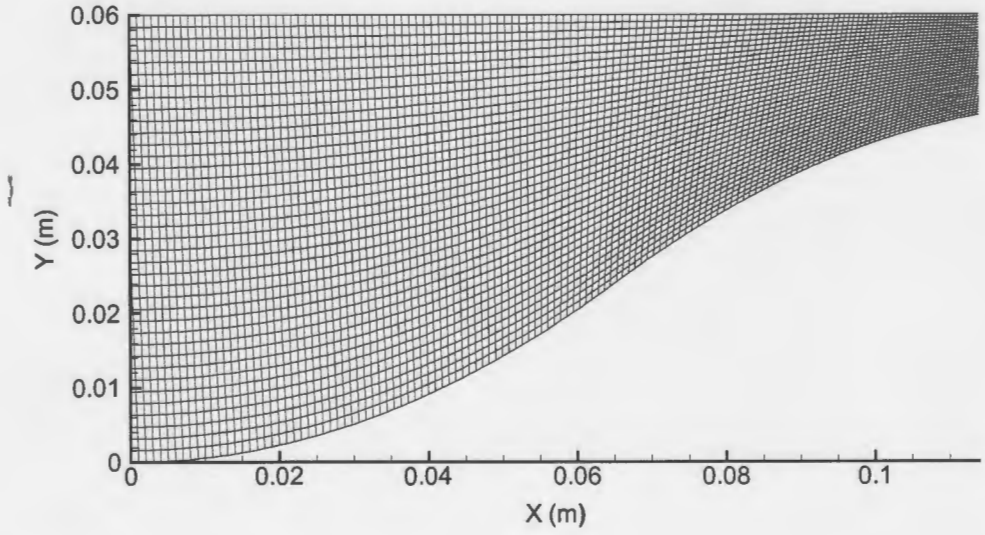

Figure 4.6: Ordered quadrilateral mesh used for simulations

4.2.4 Data capturing

For the simulations consisting of the profile and 200mm extension, pressure data for the average pressure ratio across the transmitted shock were extracted when the shock reached a distance of between 0.4 and 0.8 convergence lengths downstream from the exit of the area reduction. At this position the shock in all numerical cases proved to be planar in shape. For the simulations consisting of the extended profile with 1000mm extension, pressure data were extracted every 50mm.

4.2.5 MATLAB shock-fitting scheme

To provide additional numerical results using a different solution method, a numerical shock-fitting scheme was developed in MathWorks' MATLAB and is based on the numerical scheme presented by **Henshaw et al. (1986)**. The numerical scheme is based on Whitham's Theory of geometrical shock dynamics where the propagation of the shock front is tracked along walls and in channels. This section provides a brief overview of the program and an example of results achieved – a full software flow diagram of the code can be found in Appendix B, and the project 'm-file' with ancillary files can be located on the CD provided in Appendix A.

As introduced previously in Section 3.3, Henshaw et al. utilizes a leap–frog time marching scheme for a discrete set of points describing the propagation of the shock front within a bounded or non-bounded area. The program consists of three main sections namely;

(a) *Input variables and initialisation*

The user enters details on the profile geometry including the profile length, percentage area reduction, half inlet height, position of the inflection point and the outlet length. The only flow variables required to be specified are the initial shock Mach number and the ratio of specific heats (γ).

The initial number of x–coordinates and the maximum time–step Δt are calculated based on two rules given by **Henshaw et al. (1986)** which ensures adequate resolution and stability of the shock front for all cases. These two rules are provided in Appendix B. Once the initial grid of coordinates for $t = 0$ are assembled the corresponding scalar parameters for each grid point's arc-length [S], area [A], Mach number [MN] and Normal 'vectors' [Norm] are assembled. A figure is plotted of the profile and each subsequent shock position with connected coordinate points are overlaid on to the same plot.

The first time–step after initialisation is calculated using only the initial matrices with the expected Normal vector, but subsequent time–steps use the two step leap frog method which incorporates the current $x_i(t)$ and previous $x_i(t - \Delta t)$ coordinates to calculate $x_i(t + \Delta t)$.

(b) *Main iteration loop*

The position of each time–step Δt of the shock advances is calculated at the beginning of the main iteration loop using the two–step leap frog technique given in equation [3.13]. As the shock advances through across the defined profile, boundary conditions are checked and applied several times. This is

particularly important when calculating the coordinates for $x_i(t + \Delta t)$ where points are either added and/or removed. In the case of any points being deleted or added, the code gets stuck into an iterative loop which continues to judge the validity of the coordinates according to their spacing and boundary conditions.

Numerical dampening is implemented to dampen high–frequency errors in $x_i(t)$ and is implemented every n_s time–steps. Henshaw et al. recommends implementing numerical dampening once every 10 to 50 time–steps. The dampening is a simple two-step procedure where $x_i(t)$ is averaged between $x_{i+1}(t)$ and $x_{i-1}(t)$, for every i–even and then i–odd coordinate.

Mach number $M_i(t)$ is calculated using a Mach–Area relation based on the change in area from $A_i(t-\Delta t)$ to $A_i(t)$ and 'previous' Mach number $M_i(t-\Delta t)$. The M–A relation used is the evaluated integral equation [3.6] which corresponds to Milton's (1975) modified version of Whitham's Theory. From the literature Milton provides a correction term η which provided a significant improvement in results from the original CCW relation.

(c) *Saving and exporting of data*

After each time–step the average Mach number across the shock front is captured and saved in an *Excel* spreadsheet to compare with CFD results and theoretical predictions. The average Mach number within 5mm of the centerline was also captured in order to compare (once converted to a relative pressure) to experimental pressure tests.

4.3 Experimental Studies

4.3.1 Experimental profiles

The profiles used for experimental testing were designed based on the results from the initial CFD simulations and physical dimensions of the available testing facilities. Three sets of profiles were chosen with profile lengths of 130mm, 195mm and 260mm and all provide a percentage reduction in area of $AR = 80\%$. Each of the profile sets contains one pair of symmtrical profiles which are mounted on the upper and lower surfaces of the test section. Figures 4.7 and 4.8 show the isometric and side views with overall dimensions respectively - only one profile is depicted.

Each profile is made from aluminium and incorporates a parabolic curve $P(x)$ defined by equation [4.2]. The x, y and z coordinates used for CNC milling can be found in Appendix A – Digital Content within 'Manufacturing'. Polishing the surface of each

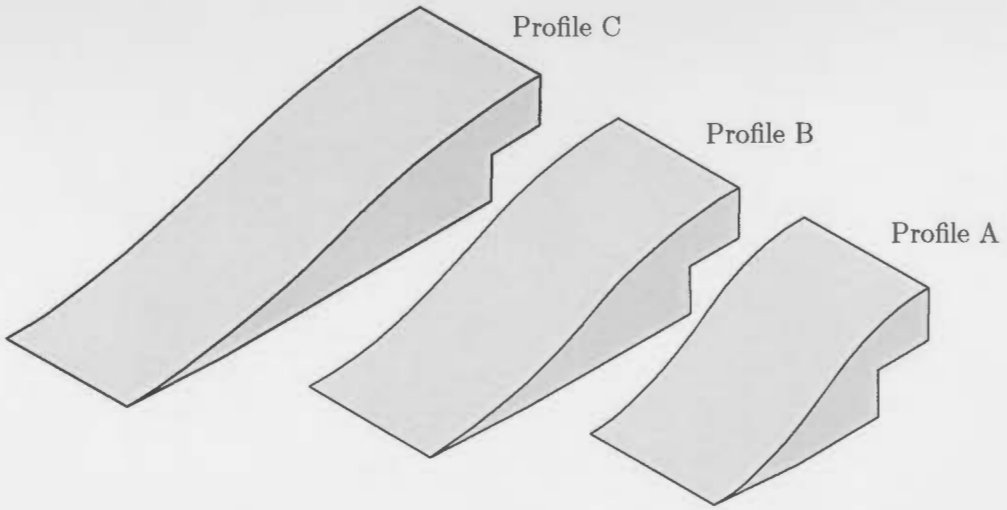

Figure 4.7: Isometric view of the 260mm [left], 195mm [center] and 130mm [right] test profiles

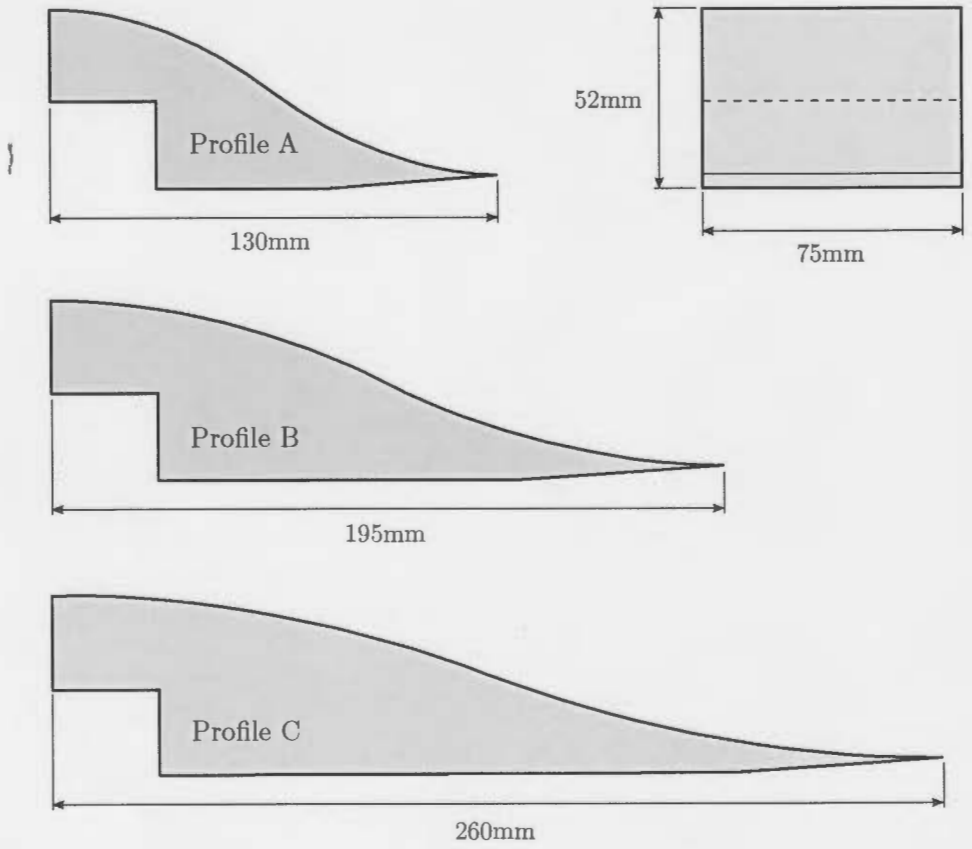

Figure 4.8: Side views of the profiles showing overall profile dimensions

profile provided a suitably smooth surface to ensure no perturbations are generated from the shock wave. A sharp 'cookie cutter' minimizes the strength of any reflected disturbances from the leading edge of the profile. In order to maximize the test

section viewing area window, spacers (see figure 4.9) were manufactured to elevate the profiles to the correct position.

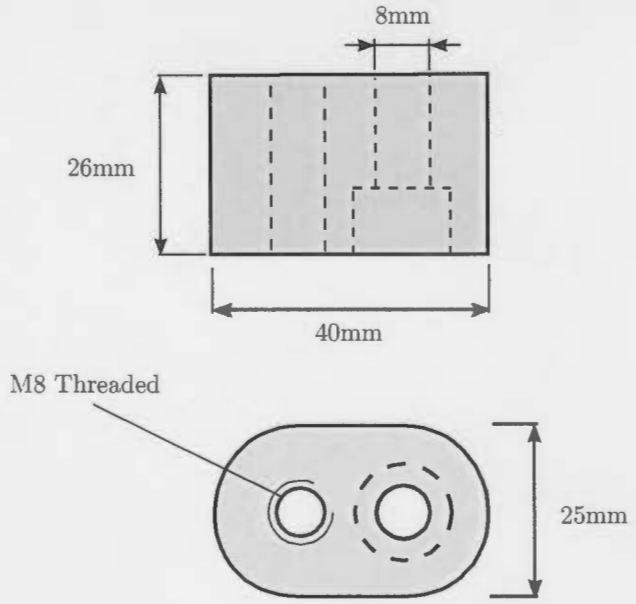

Figure 4.9: Spacer used to elevate profiles and flat extension

To study the strengthened shock and the post-shock flow beyond the profile exit two lengths of flat extensions (see figure 4.10) were manufactured from aluminium. When bolted to the end of the profile, the flat extensions sit flush with the exit of the profile.

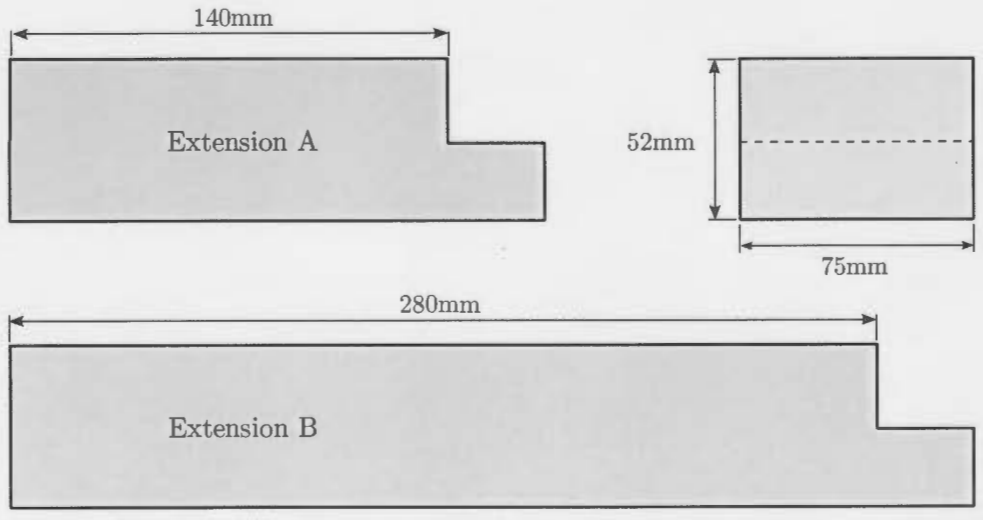

Figure 4.10: Drawing of the flat extension pieces showing overall dimensions

Figure 4.11 shows an assembly with a 195mm profile with 140mm flat extension – connecting bolts and bolt holes have been omitted. For all combinations between the three profiles (130mm, 195mm and 260mm) and the two extensions (140mm

and 280mm) the total inlet and outlet heights remain the same at 120mm and 24mm respectively. Therefore, regardless of the combination the shock undergoes a percentage reduction in area of 80%. For more detailed engineering drawings refer to Appendix D – Engineering Drawings.

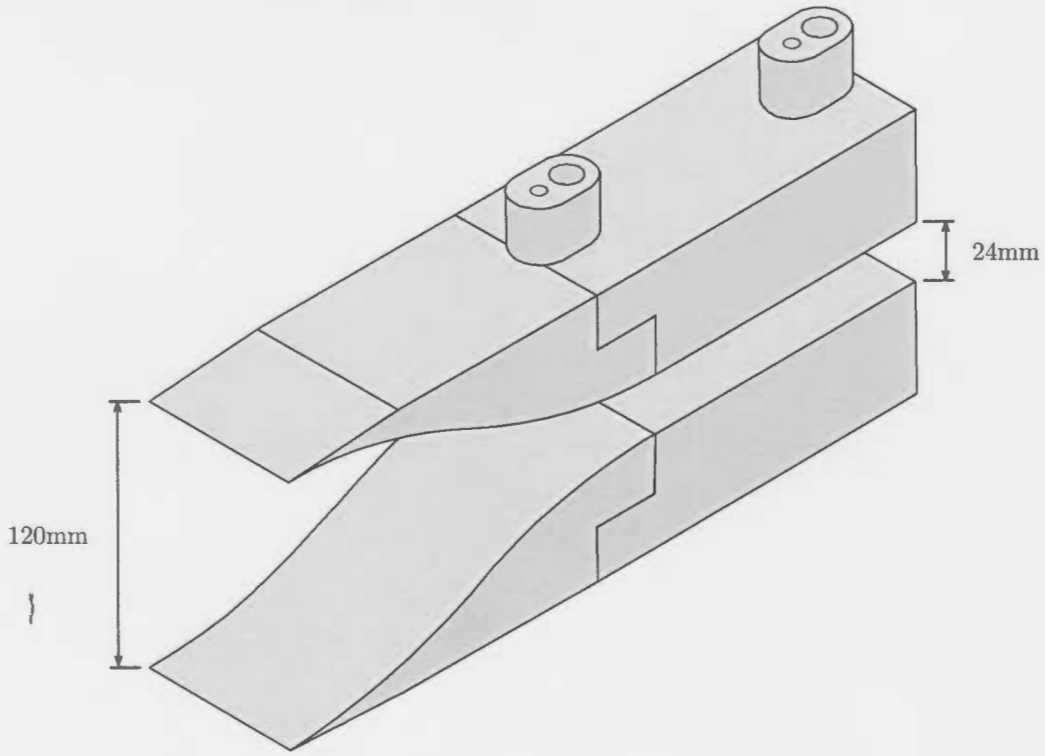

Figure 4.11: General profile assembly with extension piece and spacers

4.3.2 Experimental facilities

The Seitz shock tube located at the Flow Research Laboratory, University of the Witwatersrand, Johannesburg was used for testing due to its similar size to previous authors', but operates at a lower Mach testing range.

The Seitz tube, as depicted in Figure 4.12 on the following page, consists of a compression and intermediate chamber containing a rapid decreasing cross-sectional area and are separated by two plastic diaphragm sheets. The combination of thicknesses of diaphragms varies depending on the required shock Mach number. The compression and intermediate expansion chambers are sealed by a hydraulic piston and pressurised, once exposed separately to the building's high pressure pneumatic lines to a predetermined value. All activation/deactivation of the hydraulic and pneumatic lines are controlled automatically by a dedicated Seitz tube computer. Pressure in the three chambers are monitored by the program using low-speed pressure transducers mounted in their respective chambers.

The compression waves travelling down the 6m long expansion chamber steepen to a planar shock wave before entering the sealed test section containing two 55mm thick, 300mm quartz glass viewing area windows. Transverse waves produced from rupturing of the diaphragm are effectively dampened using carpet strips located within a short distance of the upper and lower sections of the expansion tube. The viewing windows located on either side of the test section are mounted on pivoting doors so that the test section can be easily accessed but also provide an airtight seal once fastened. To obtain more accurate pressure data, one of the doors can be removed and replaced with a similar door but containing an array of potential high-speed pressure transducer ports. Major performance specifications are listed in table 4.3.

Table 4.3: Technical specifications for the M. Seitz shock tube

Specification	Detail
Mach number range:	$M = 1.1 \rightarrow 1.8$
Driver:	Air
Test section pressurisation:	Atmospheric
Testing section dimensions ($H \times B \times W$):	$180 \times 180 \times 76$ mm
Expansion chamber length (L):	6 m
Viewing window:	Diameter = 300 mm Thickness = 55mm Max Press. = 20bar
Pressure transducers: (High-speed)	PCB 1μs, Kistler 2μs (Piezo-electric)
Pressure port intervals:	450mm (Exp. chamber) 15mm (Test section)
Control mechanism:	Fully automated, computer controlled

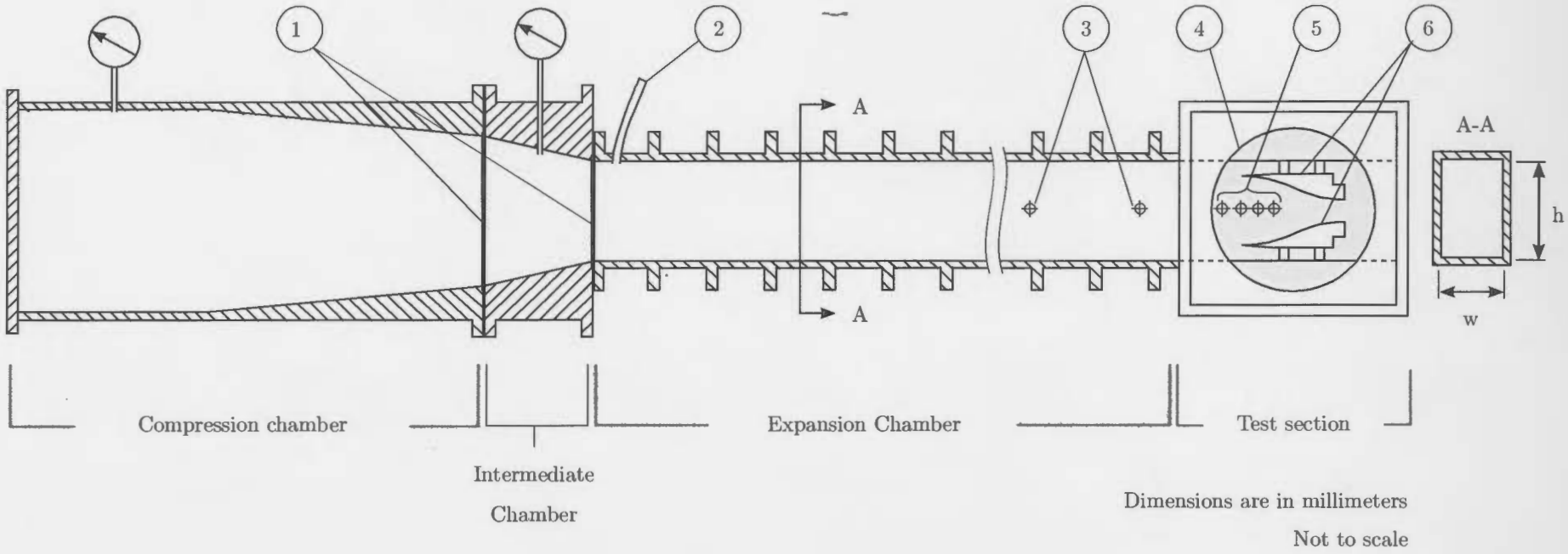

Figure 4.12: General arrangement of the M. Seitz (2001) shock tube

Part No.	Part Description	Part No.	Part Description
1	Plastic diaphragms	4	Quartz glass viewing window
2	Evacuation tube	5	Test section pressure taps
3	Upstream pressure taps	6	Parabolic Profiles

Figures 4.13 to 4.15 show the combination of profiles and flat extensions and how each are arranged within the test section viewing window.

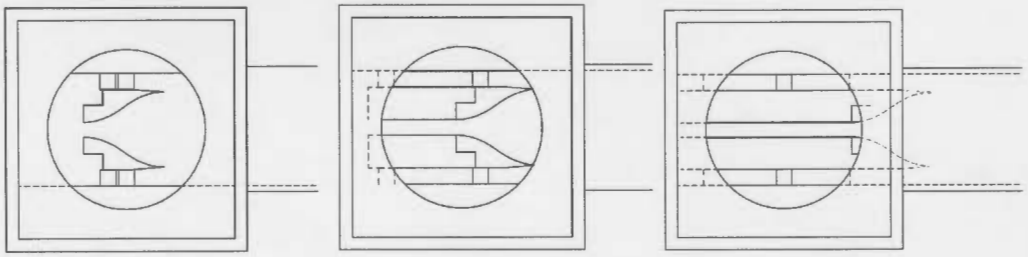

(a) (b) (c)

Figure 4.13: Assembly placement of (a) 130mm profile with (b) 140mm flat section and (c) 280mm flat section within the test section

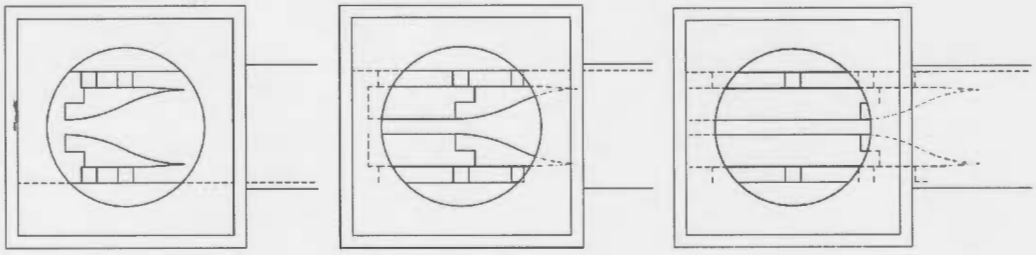

(a) (b) (c)

Figure 4.14: Assembly placement of (a) 195mm profile with (b) 140mm flat section and (c) 280mm flat section within the test section

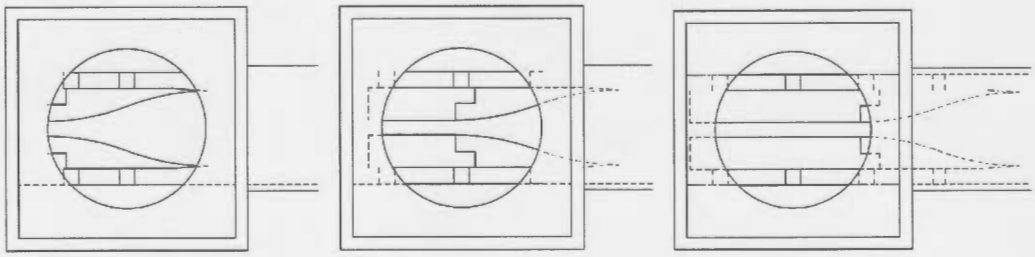

(a) (b) (c)

Figure 4.15: Assembly placement of (a) 260mm profile with (b) 140mm flat section and (c) 280mm flat section within the test section

4.3.3 Pressure Testing

Pressure tests were conducted by replacing one of the test section viewing windows with a machined aluminum pressure door consisting of a grid of pre–drilled pressure tappings. Three positions labeled 1,2 and 3 in figure 4.16 were allocated for pressure transducers. Pressure readings were taken for each of the profiles within (a) the 'profile section' utilising the profile and half flat extension and (b) the reduced section utilising the profile and full flat extension. Calibration constants for each of the pressure transducers used are provided in Appendix – C.2.

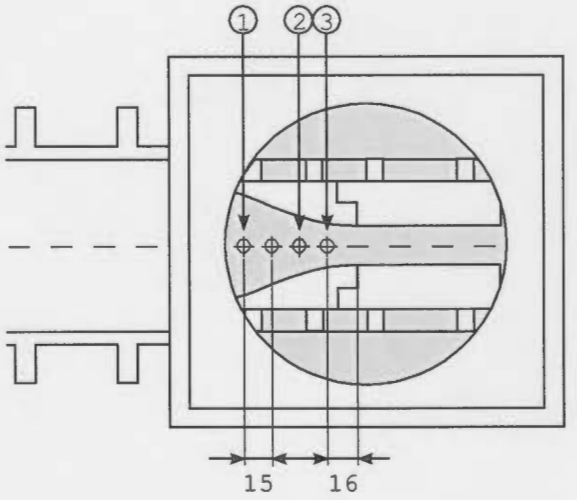

(a)

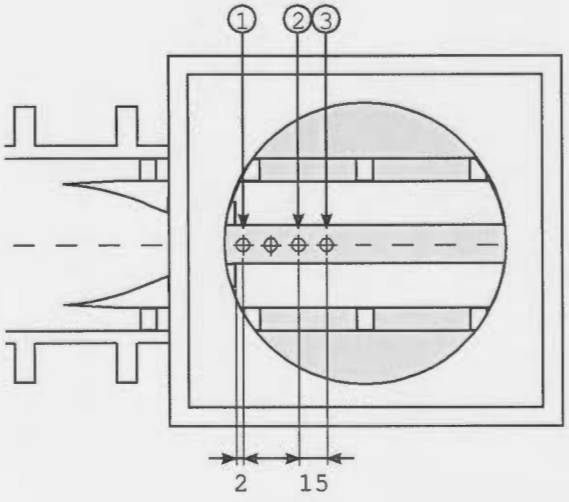

(b)

Figure 4.16: (a) Location of pressure tappings within the profile section, (b) location of pressure tappings within the reduced section

4.3.4 Flow visualisation setup

The following three visualization methods were used to capture the development of the shock wave and the accompanying flow disturbances whilst traveling through the area reduction.

1. Single shot, high resolution, colour Schlieren
2. High-speed video, low resolution, colour Schlieren
3. Single shot, high resolution, monochrome shadowgraph

All three optical setups utilised a standard horizontal 'z'-configuration at an angle of 10.2° to the central beam passing perpendicularly through the test section. Each rail is directed towards a parabolic front-silvered mirror with f-number $f/6$ and 254mm diameter. In order to minimize the astigmatism inherent to a 'z'-configuration, a small cylindrical lens ($f = 25$mm) is inserted after the first cut-off on the light source side. Unless otherwise specified all vertical and horizontal cut-offs comprise of stainless-steel Lion razer blades. All optical rails, lenses and parabolic mirrors were accurately leveled and aligned using a digital inclinometer and a rail-mounted cross-hair laser. Figures 4.17, 4.18 and 4.19 give overviews for all three optical setups and table 4.4 shows the main technical specifications for both the high resolution single shot camera and the lower resolution high-speed camera. For full instructions on how the rails and lenses were correctly setup, see the file '*Guide to Setup - Schlieren Optical System.pdf*' located on the CD provided in Appendix A.

Table 4.4: Technical specifications for the single-shot and high-speed cameras

Specification	**High Resolution Photo Single Shot Photo**	**Low Resolution High-Speed Video**
Camera:	Fujifilm S3 Pro DSLR	Photron FASTCAM SA5
Frame rate:	1 frame per exposure	60 000 – 185 000fps
Resolution:	Fixed, 12MP 3030 x 2036	Dependant on frame rate 320 x 264 @ 75kfps 832 x 96 @ 100kfps 320 x 88 @ 186kfps
Shutter/trigger:	Manual	External, 5V signal
Exposure time:	1μs	1μs
Light source:	15W Hamamatsu Xenon flash lamp	Canon 430EX Speedlite flash

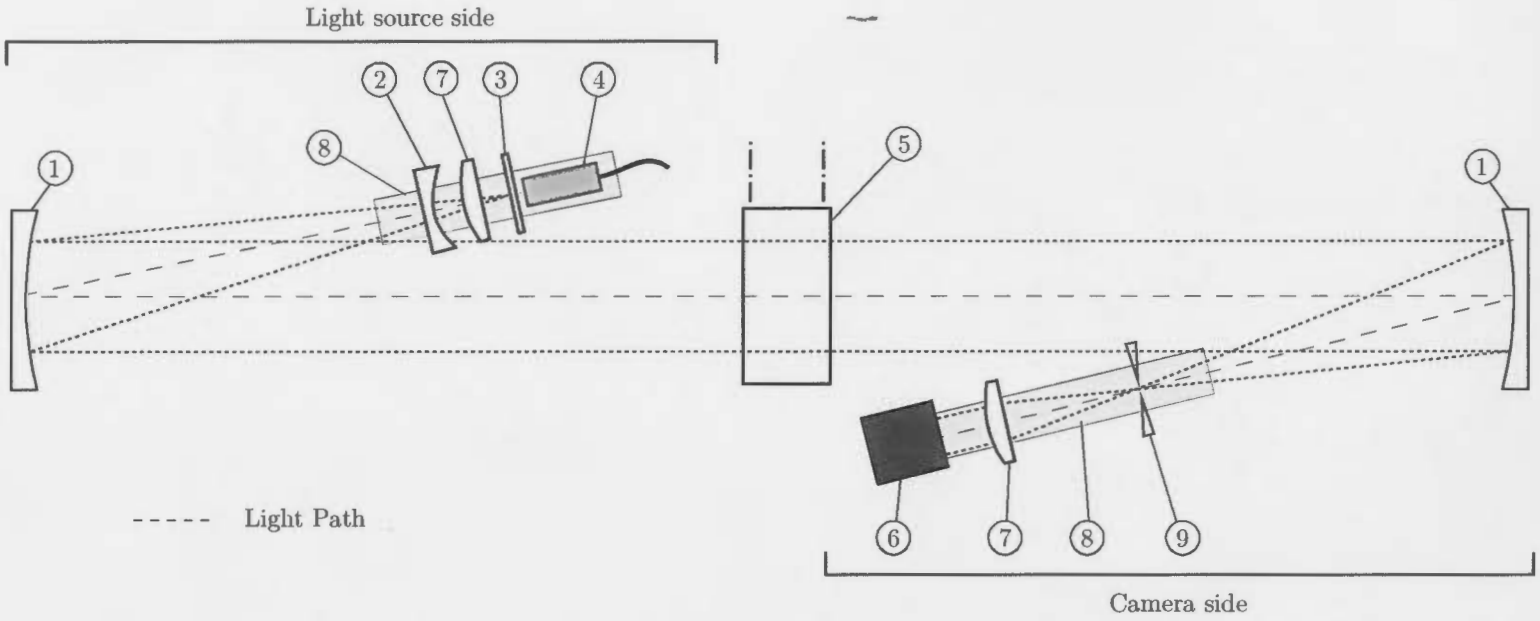

Figure 4.17: General arrangement of 'z'-configuration high resolution, single-shot, colour Schlieren photography

Part No.	Part Description	Part No.	Part Description	Part No.	Part Description
1	Schlieren mirror	4	Light source	7	Converging lens
2	Cylindrical lens	5	Test section	8	Optical rail
3	Colour mask	6	Digital camera	9	Iris cut-off

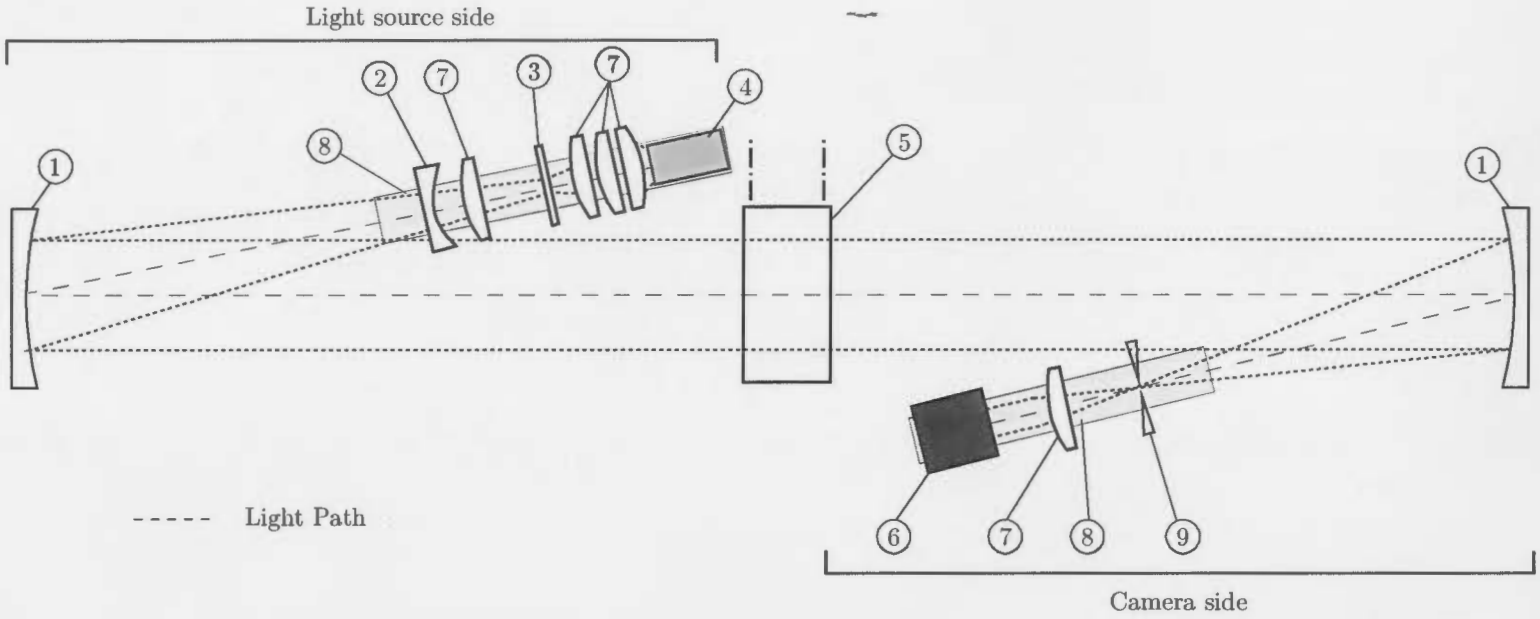

Figure 4.18: General arrangement of 'z'-configuration low resolution, high-speed video, colour Schlieren

Part No.	Part Description	Part No.	Part Description	Part No.	Part Description
1	Schlieren mirror	4	Light source	7	Converging lens
2	Cylindrical lens	5	Test section	8	Optical rail
3	Colour mask	6	High-speed camera	9	Iris cut-off

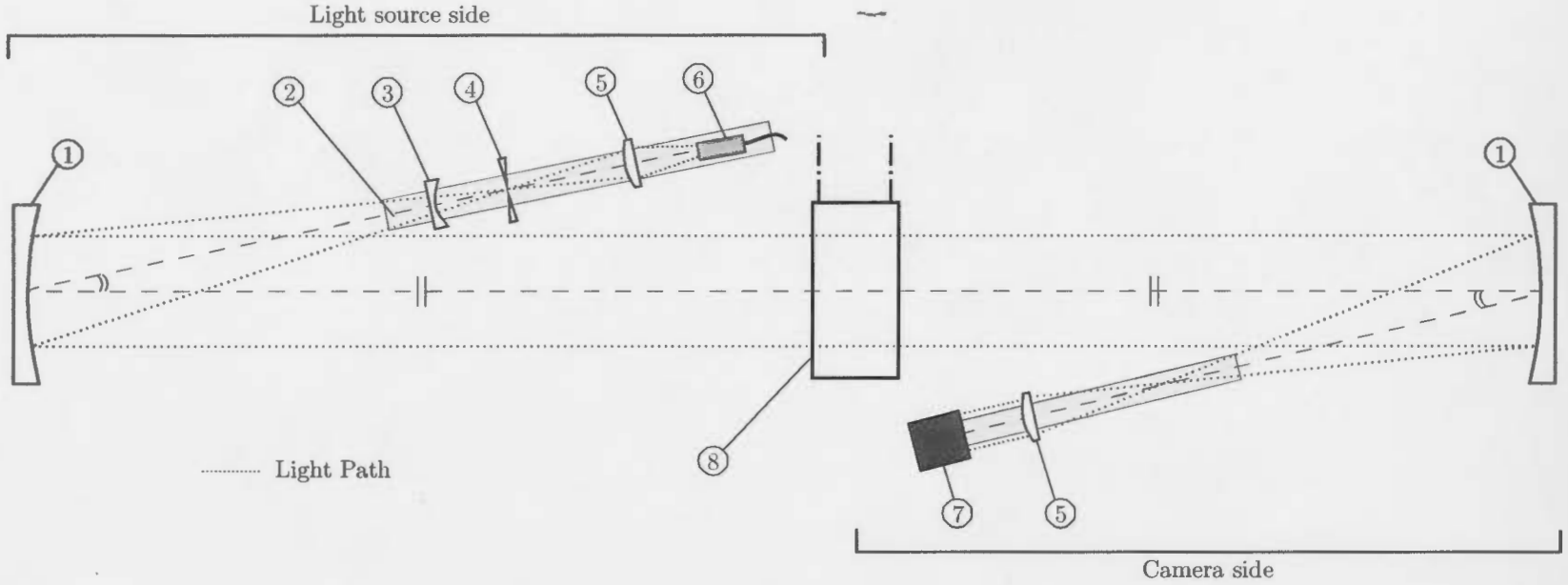

Figure 4.19: General arrangement for 'z'-configuration, high resolution, shadowgraph photography

Part No.	Part Description	Part No.	Part Description	Part No.	Part Description
1	Schlieren mirror	4	Cut-off	7	Digital Camera
2	Optical rail	5	Converging lens	8	Test section
3	Cylindrical lens	6	Light source		

Two different light sources were used for the Photron high-speed camera and single-shot Fujifilm camera. The Fujifilm camera does not have a low enough shutter speed to capture a focused image of the shock wave or any flow disturbances, so a Hamamatsu Xenon flash lamp capable of generating a pulse of light for $1\mu s$ was used. Conversely, the Photron high-speed camera does have the capability of a maximum shutter of $1\mu s$ but requires a large amount of light and relatively long exposure of 15ms. Hence, a Canon Speedlite flash was used to provide the necessary intensity and duration of light. In both cases the Seitz tube computer was used to provide the necessary delay timer and trigger signal once the shock passed the two upstream pressure transducers (see figure 4.12 for reference). The Hamamatsu flash lamp generates a very defined beam of light between two closely positioned electrodes, this makes it easy to converge the emitted light back to a defined point using only a single converging lens. In comparison, the Canon flash emits a wide defuse band of light and therefore up to three converging lenses were required to focus the light.

To create the colours for colour Schlieren, a simple elliptical colour mask was printed onto a blank film to filter the light into the three primary colours (see figure 4.20) and the mask was placed at the typical 'white light' point light source. The shape of the colour mask is elliptical in order to correctly distort to a circle on passing through the cylindrical lens. At the camera end, instead of the light focusing back down to a point it focuses down to a replication of the primary colours of the colour mask. At this focal point, an adjustable iris is used to 'cut-off' any deviations of light resulting from any density gradients within the test section, hence the sensitivity of this system is omni-directional.

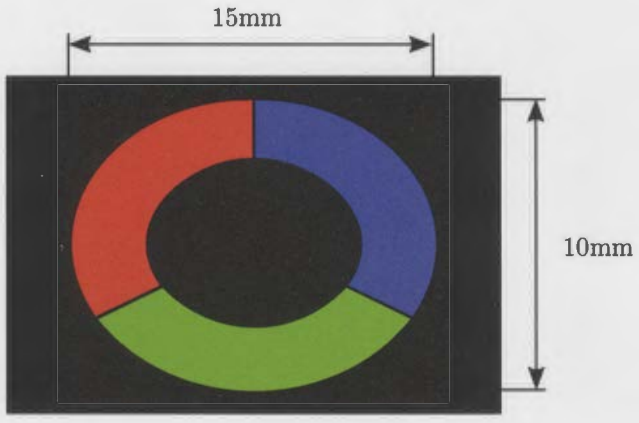

Figure 4.20: Elliptical colour mask used in the single shot and high-speed colour Schlieren optical setups

To assist in accurately positioning the colour mask and cylindrical lens a parabolic calibration lens with a high focal distance is used to simulate an artificial 'density gradient'. Figure 4.21 shows an example of an acceptable calibration image using the calibration lens.

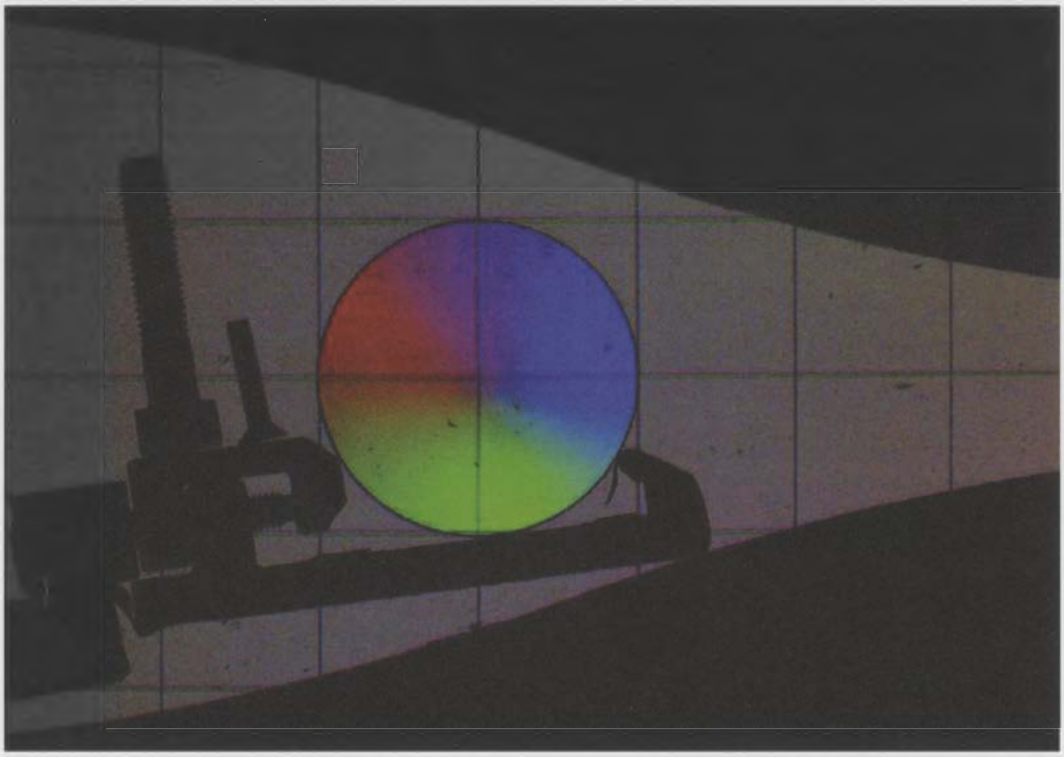

Figure 4.21: Test image of colour Schlieren optical system using calibration lens

In figure 4.21 all the colours are distributed evenly within and about the center of the calibration lens. The vibrancy and variation of the colours near the center of the lens will typically indicate the degree of sensitivity of the setup in all directions.

The background provides a uniform light grey colour (both horizontally and vertically) which indicates that in all regions the light is passing parallel through the test section and that the optical rails are correctly aligned. Towards the edges of the image there will be slight discolouring as the image may be distorted by the edges of any of the lenses or camera aperture.

Within each image the grid lines will appear unfocused with evidence of chromatic aberrations, this is to be expected since the grid wires are secured outside of the test section which is the main area of focus. In terms of focus, the threads on the bolts appear in focus as they are located in the center of the test section.

Whilst figure 4.21 presents an unedited JPEG version of the original RAW image file taken, by adjusting the global brightness and contrast levels an improved edited image of figure 4.21 is shown in figure 4.22. This form of editing helps to improve overall clarity without distorting the results.

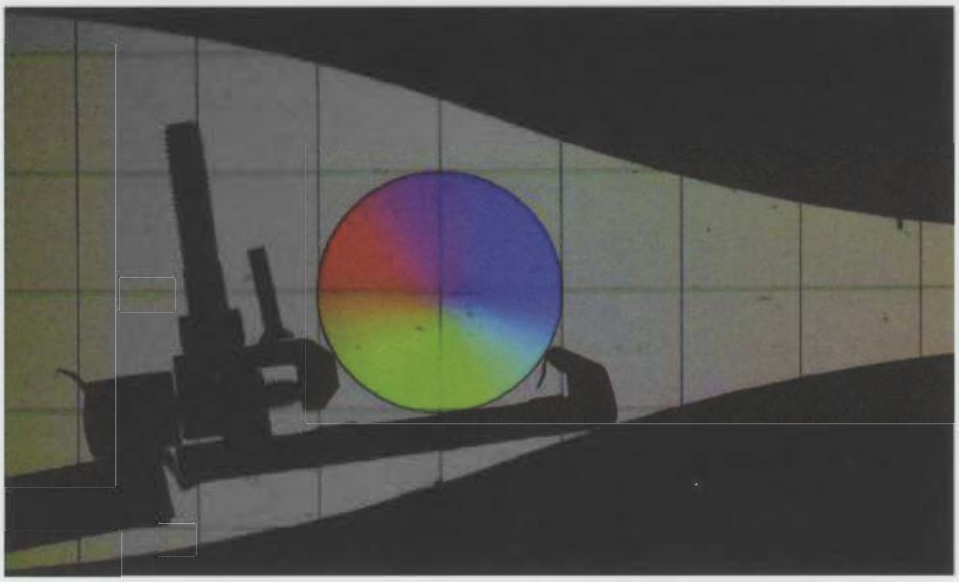

Figure 4.22: Edited test image where exposure and shadow controls are adjusted

5 Observations

This section provides a summary of the initial CFD simulations, experimental images and pressure traces observed during numerical and experimental stages of the research.

5.1 Initial CFD observations

The initial set of CFD simulations provided a basis for design and further experimental study. Figures 5.1, 5.2 and 5.3 show the three different types of flow developments for the parabolic profiles 130, 195 and 260mm respectively.

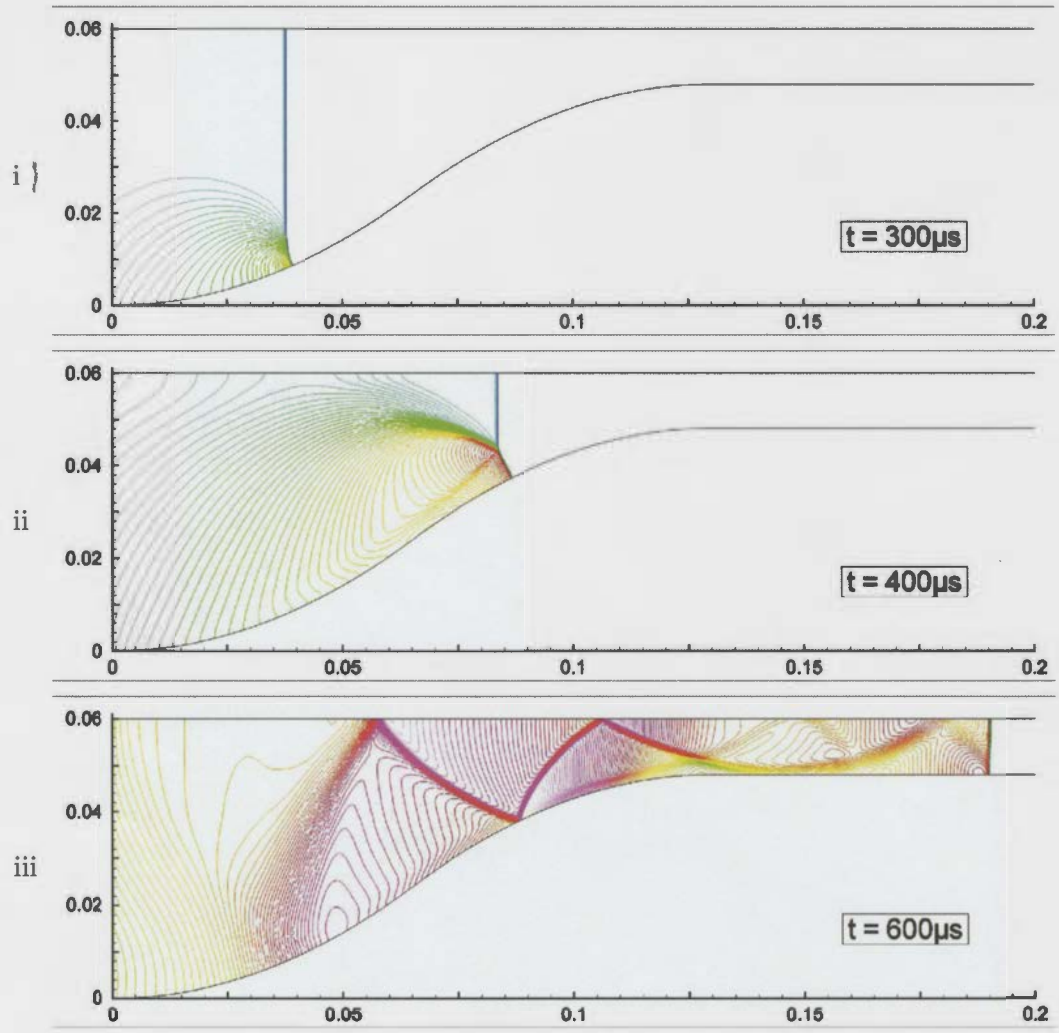

Figure 5.1: Two hundred isodensity plots from 1.6 to 2.8 for a 130mm profile ($M_i = 1.33$) from $t = 300\mu s$ to $t = 600\mu s$

A range of profile parameters were tested including simulations varying the inlet Mach number, point of inflection and percentage reduction in area ratio as set out in table 4.1. Of those simulations, 130m, 195m and 260mm parabolic profiles each with an inflection point at 50% and an 80% reduction in area ratio were chosen for further experimental testing based on their three different types of flow characteristics where the initial shock Mach number used was $M_s = 1.4$. Each plot represents contour lines of similar density values ranging from 1.4 to 2.8 kg/m^3.

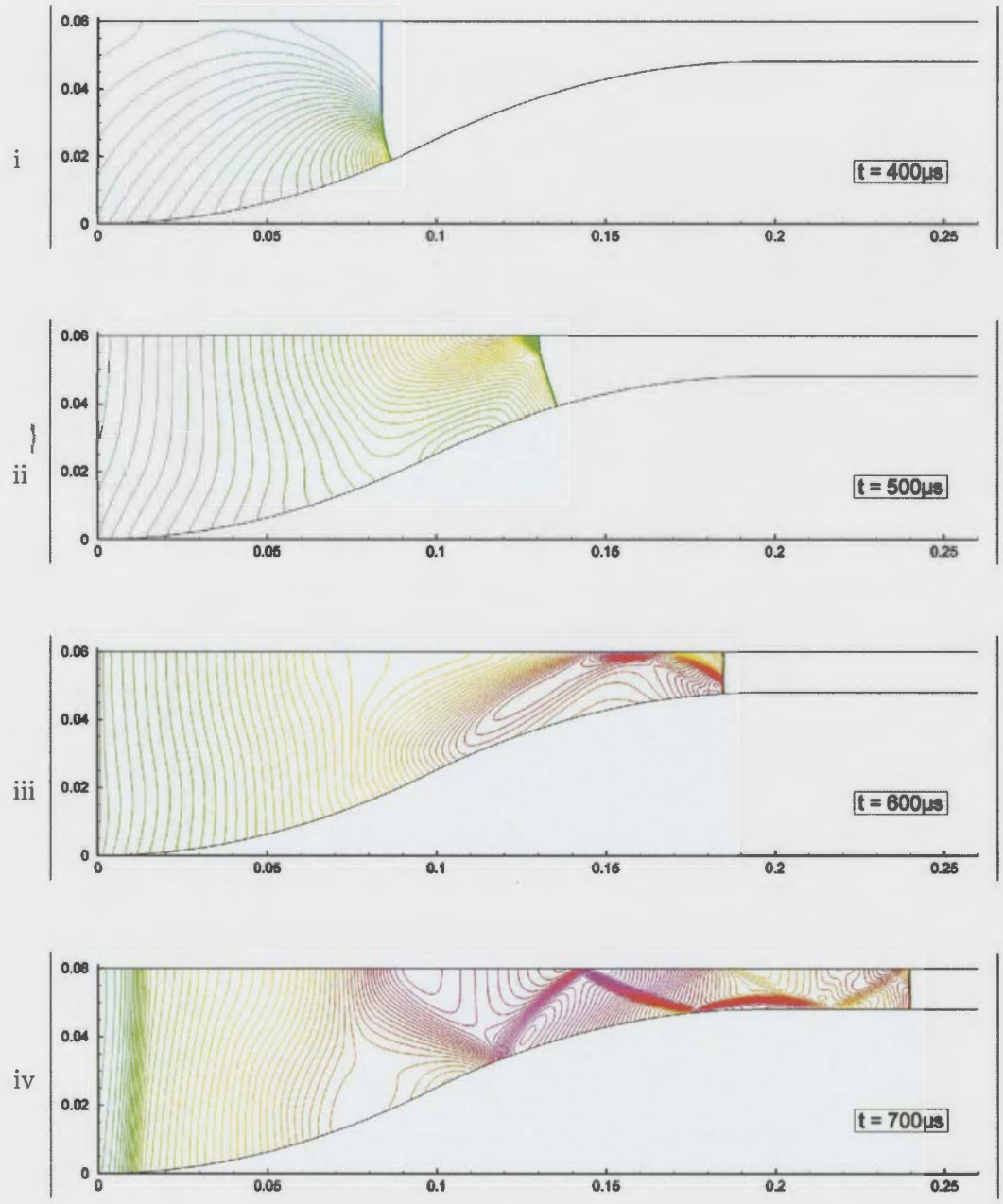

Figure 5.2: Two hundred isodensity plots from 1.6 to 2.8 for a 195mm profile ($M_i = 1.33$) from $t = 400\mu s$ to $t = 700\mu s$

For the three different profiles, the 130mm profile shows clearly a developed Mach reflection whereas the 260mm profile does not show any signs of transition, and the 195mm appears to show characteristics of both flows.

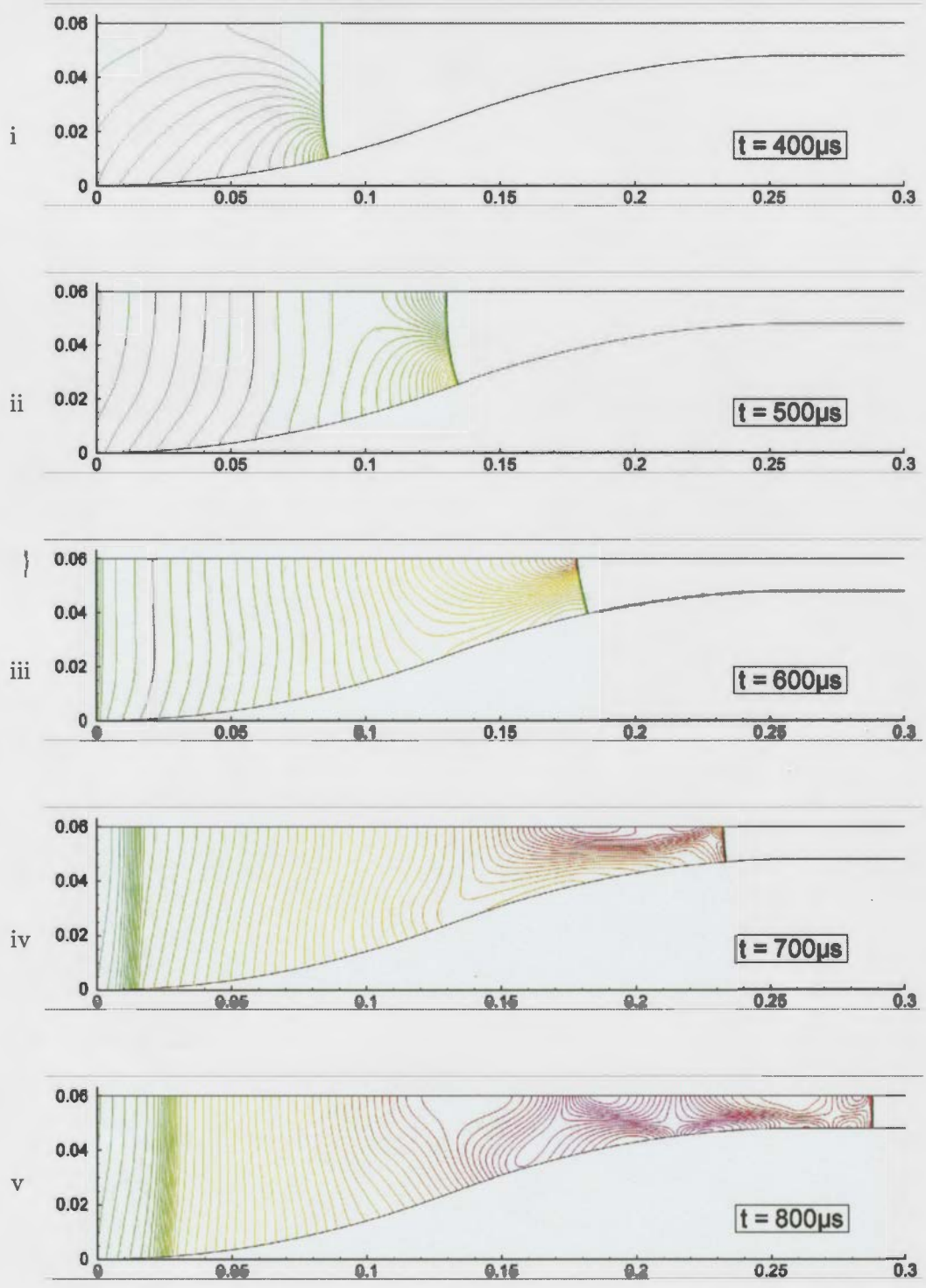

Figure 5.3: Two hundred isodensity plots from 1.5 to 2.8 for a 260mm profile ($M_i = 1.33$) from $t = 400\mu s$ to $t = 800\mu s$

5.2 Experimental Images

This section provides sample images of those captured during experimental testing, for full resolution images and high–speed videos refer to Appendix – A under the folder entitled *'Experimental Testing'*.

Figures 5.4 to 5.8 show comparative time–lapse images for a $M_s = 1.33$ shock wave propagating through each of three profiles. Overall, the collection of images show the propagation of the shock wave through the profile reduction and further along down the reduced channel. Each image was captured separately using the high-resolution, colour Schlieren visualisation setup with the Fujifilm S3 Pro DSLR detailed previously in section 4.3.4. The colours presented in each images can be correlated to the colour calibration image reproduced in figure 4.21.

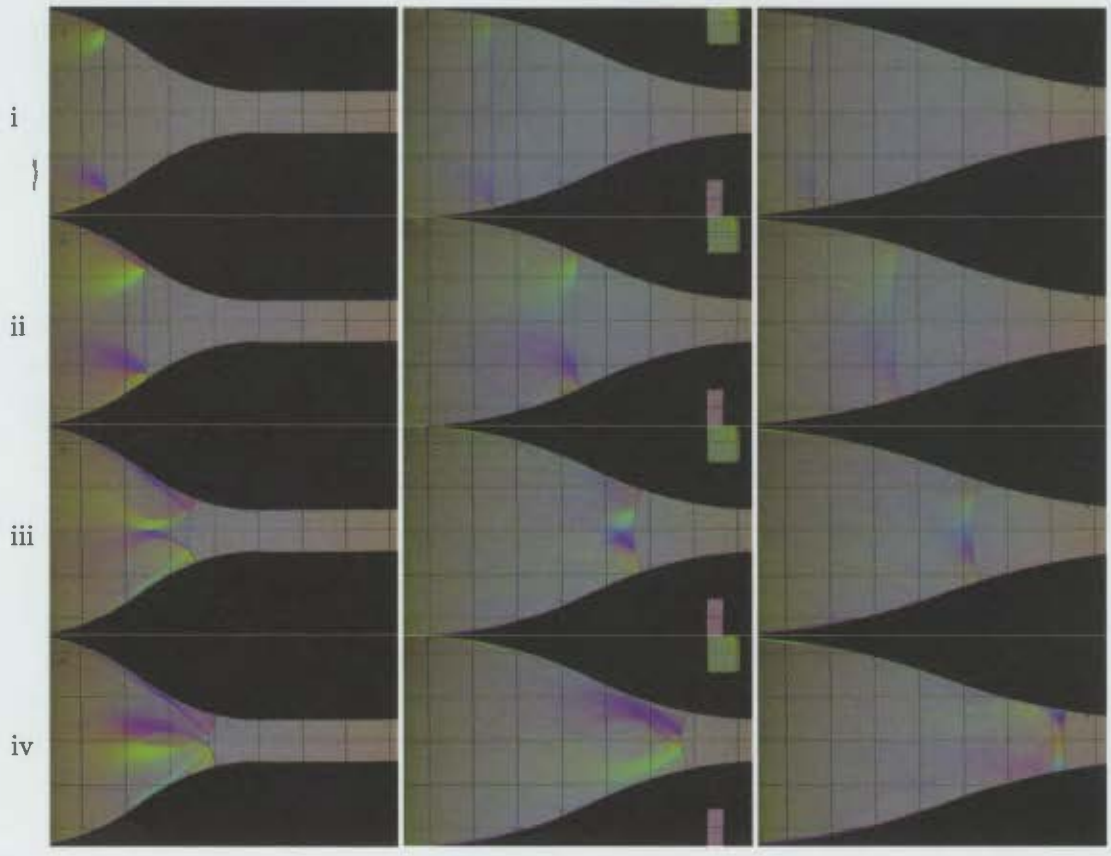

Figure 5.4: Time–lapse of a $M_s = 1.33$ shock wave propagating through a) 130mm Profile, b) 195mm Profile and c) 260mm Profile

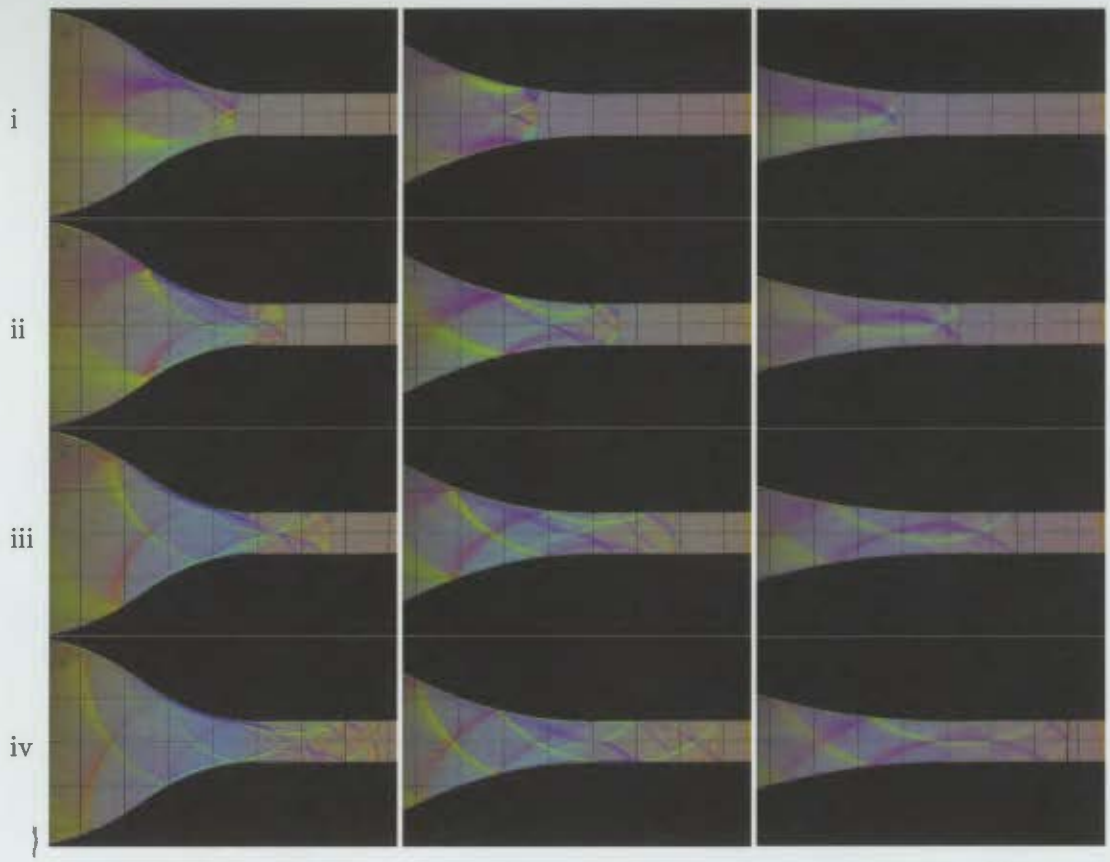

Figure 5.5: Shock propagation following each profile exit

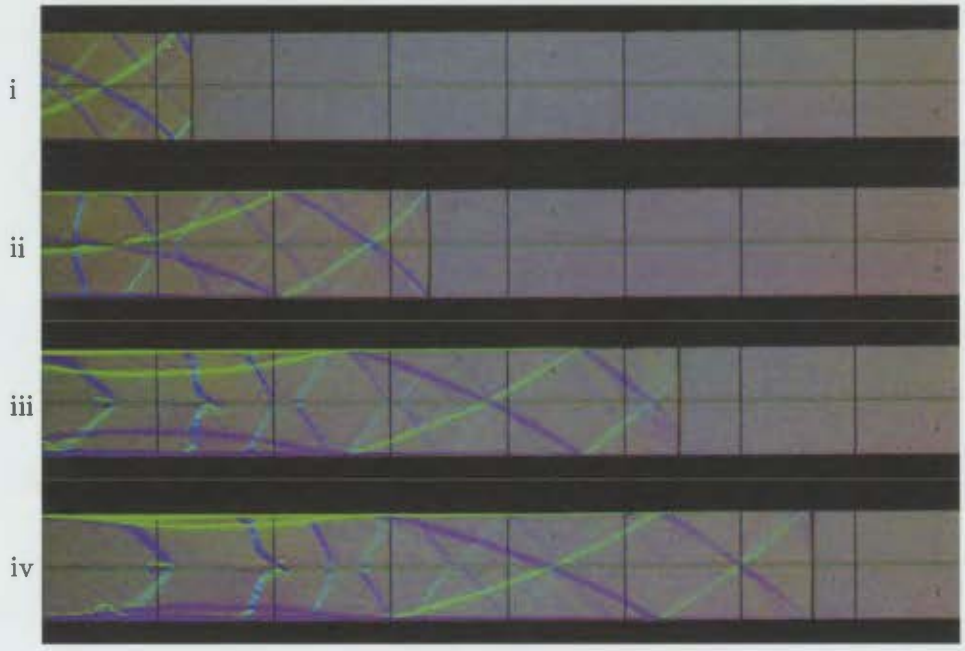

Figure 5.6: Progression of strengthened shock traveling through reduced section for a 130mm profile

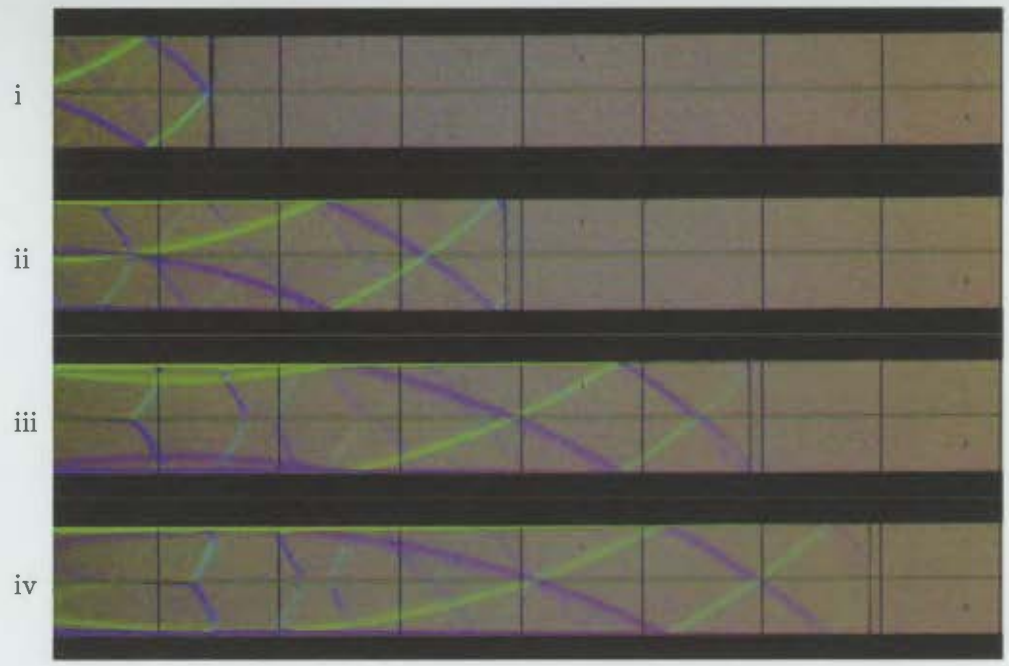

Figure 5.7: Images showing progression of strengthened shock wave traveling through reduced section from 195mm profile

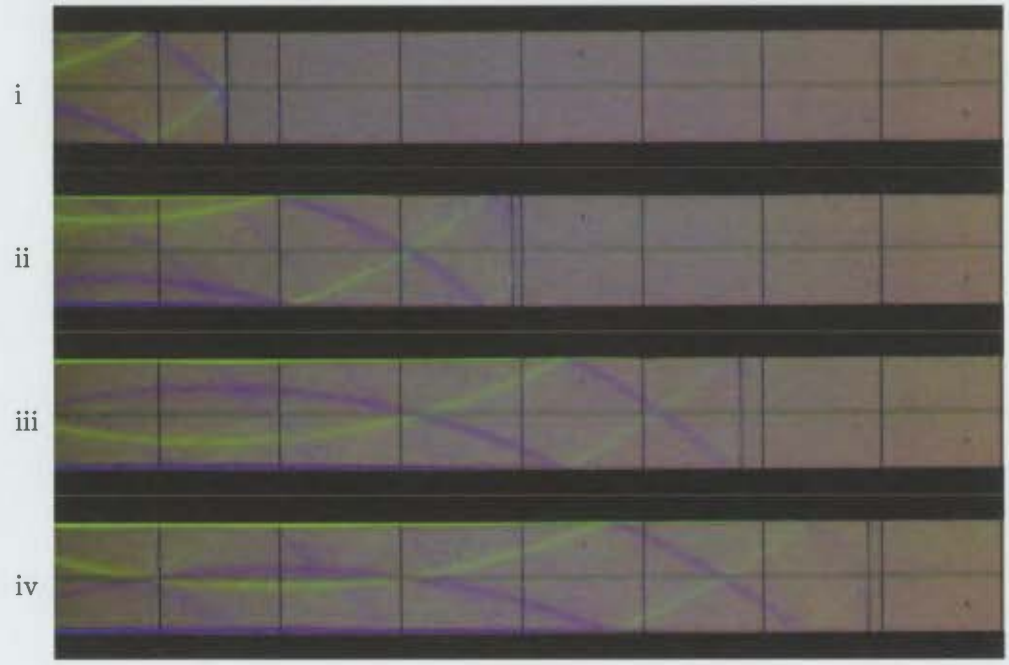

Figure 5.8: Images showing progression of strengthened shock wave traveling through reduced section from 260mm profile

In addition to the high resolution colour Schlieren, high–speed video footage was captured for the profiles and reduced channel views. Figure 5.9 shows every fifth image extracted from high–speed video footage captured at 87500 frames per second using a similar colour Schlieren setup. The images are cropped from the original 96 (H) x 832 (W) pixels to where the shock front ends. The images are then read into a MATLAB code that calculates the shock Mach number based on the cropped length, size calibration image and known camera frame rate. For high–speed footage for all three profiles, see Appendix A under the folder '*Experimental Testing*'.

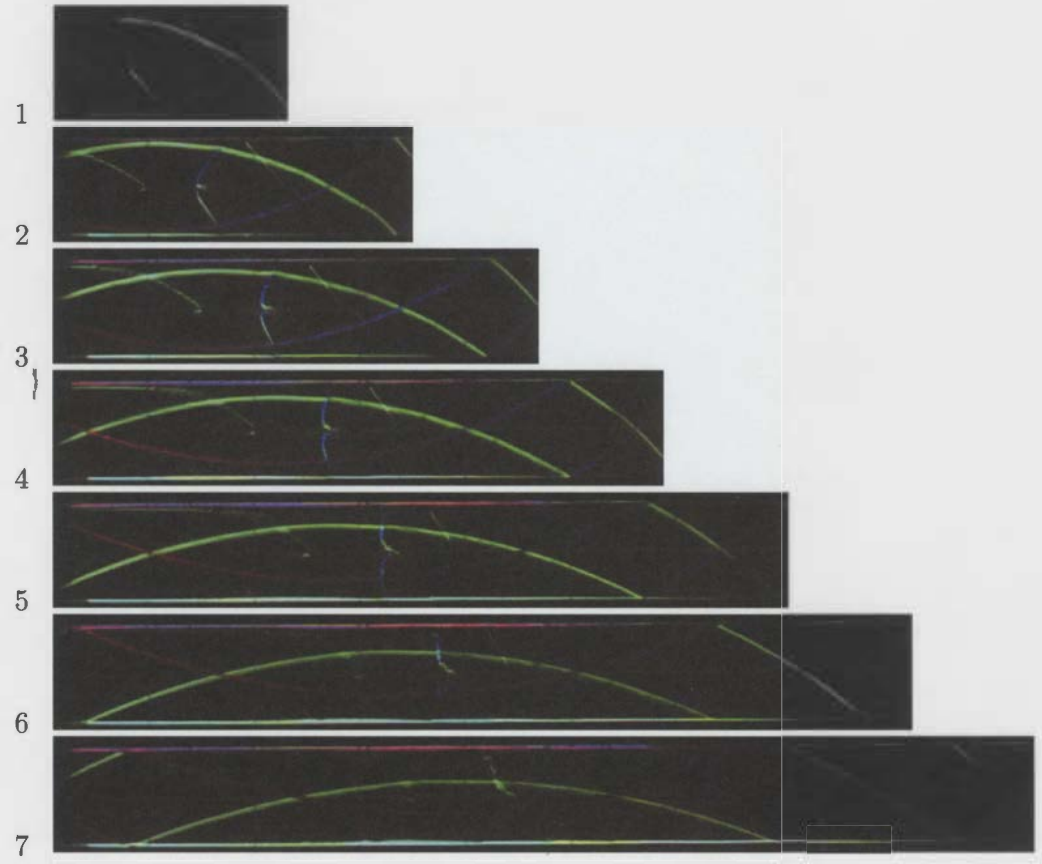

Figure 5.9: Cropped (and stacked) images extracted from the recorded high–speed video used for calculating the transmitted shock Mach number

Finally, figure 5.10 on the following page provides a time–lapse shock progression similar to figure 5.4a) for the 130mm profile but the images have been captured using a typical shadowgraph visualisation technique.

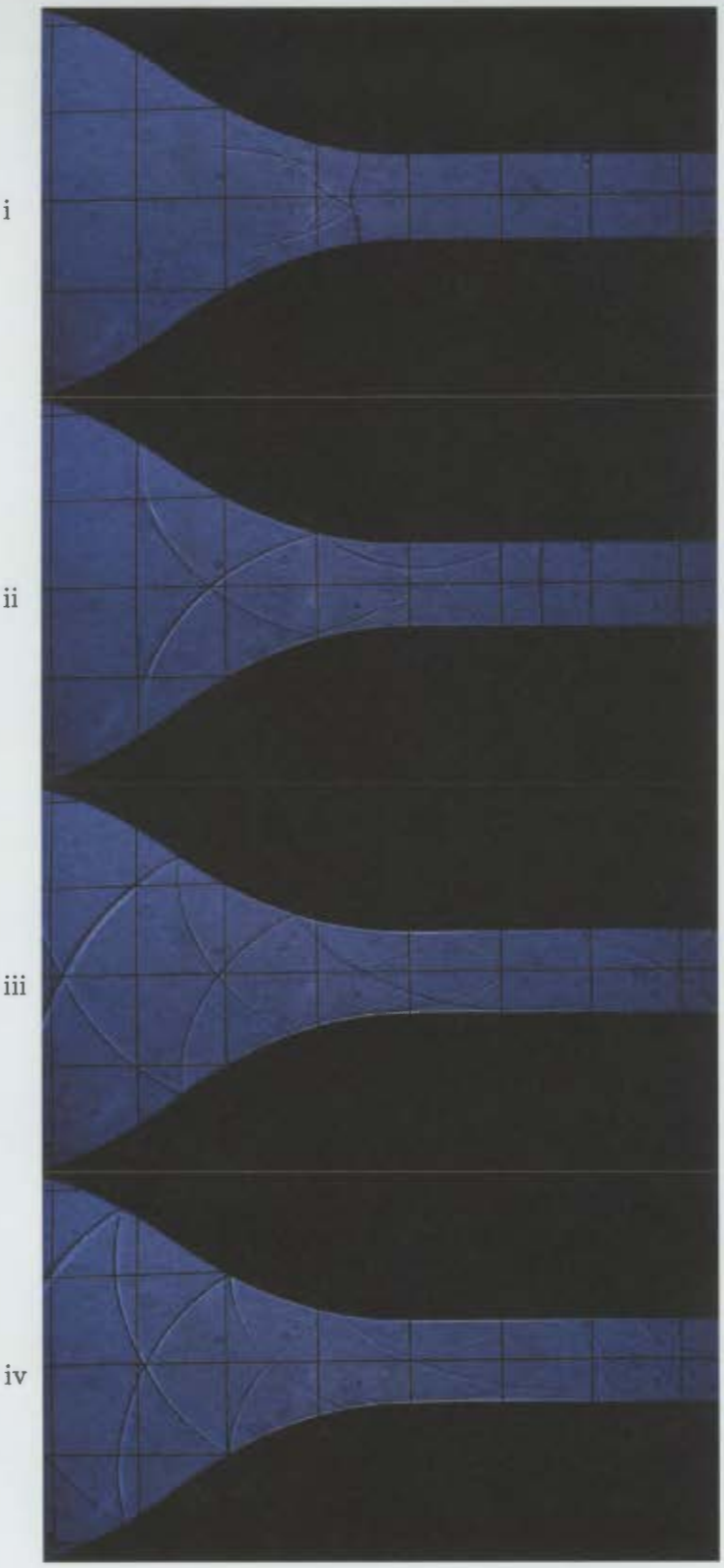

Figure 5.10: Shadowgraph images showing progression of a planar shock wave traveling through a 130mm profile

5.3 Experimental Pressure Traces

Figure 5.11 shows an example of pressure traces obtained from three pressure tappings located in the profile section for a 130mm profile with half length flat extension. Pressure readings have been converted to gauge pressure using the calibration constants provided in Appendix – C.2.

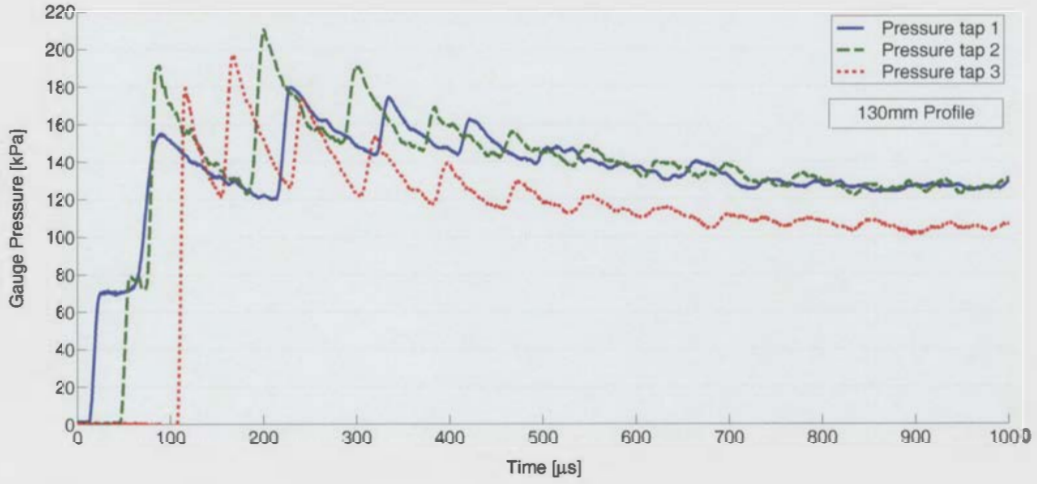

Figure 5.11: Pressure tracing for 130mm profile for three tappings situated on centerline of test section

Figure 5.12 shows an example of pressure traces obtained from three pressure tappings located in the reduced channel section for a 130mm profile with full length flat extension. For pressure traces recorded for 195mm and 260mm profiles, see Appendix C.2.

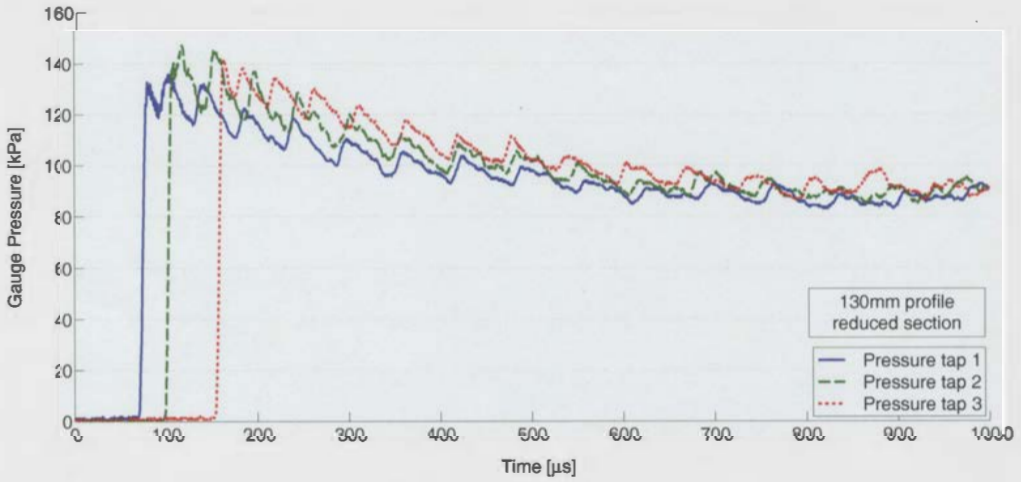

Figure 5.12: Pressure tracing for 130mm profile for three tappings situated within the extended reduced section

5.4 MATLAB Numerical Observations

Figure 5.13 and 5.14 show the MATLAB observations, using Henshaw's method, recorded for the 130mm profile. In figure 5.13 a pressure trace is shown for the average Mach number across the length of the shock where the average Mach number is calculated over the entire length of the shock front. This is a variable length scale for each time–step based on the measurement over the entire length of the shock from the profile surface to where the shock intersects the symmetry plane (or top of the domain). The shock 'length' for each time–step is associated with the position of the leading edge of the shock at the centerline. Figure 5.14 shows the shock Mach number measured solely at the symmetry plane. Both figures are provided with a plot of the relative position of the shock drawn at a set interval based on the percentage completion of the simulation.

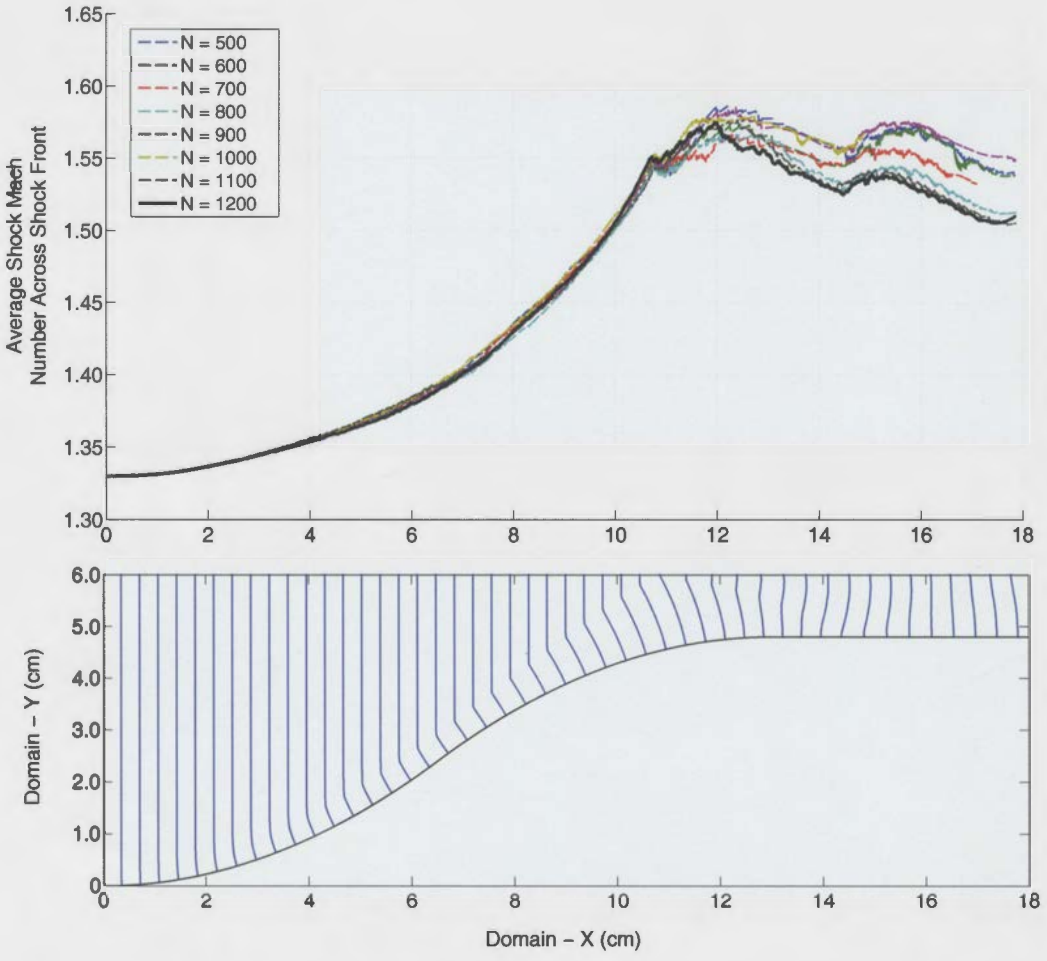

Figure 5.13: Average shock Mach number across the leading shock front for a 130mm profile

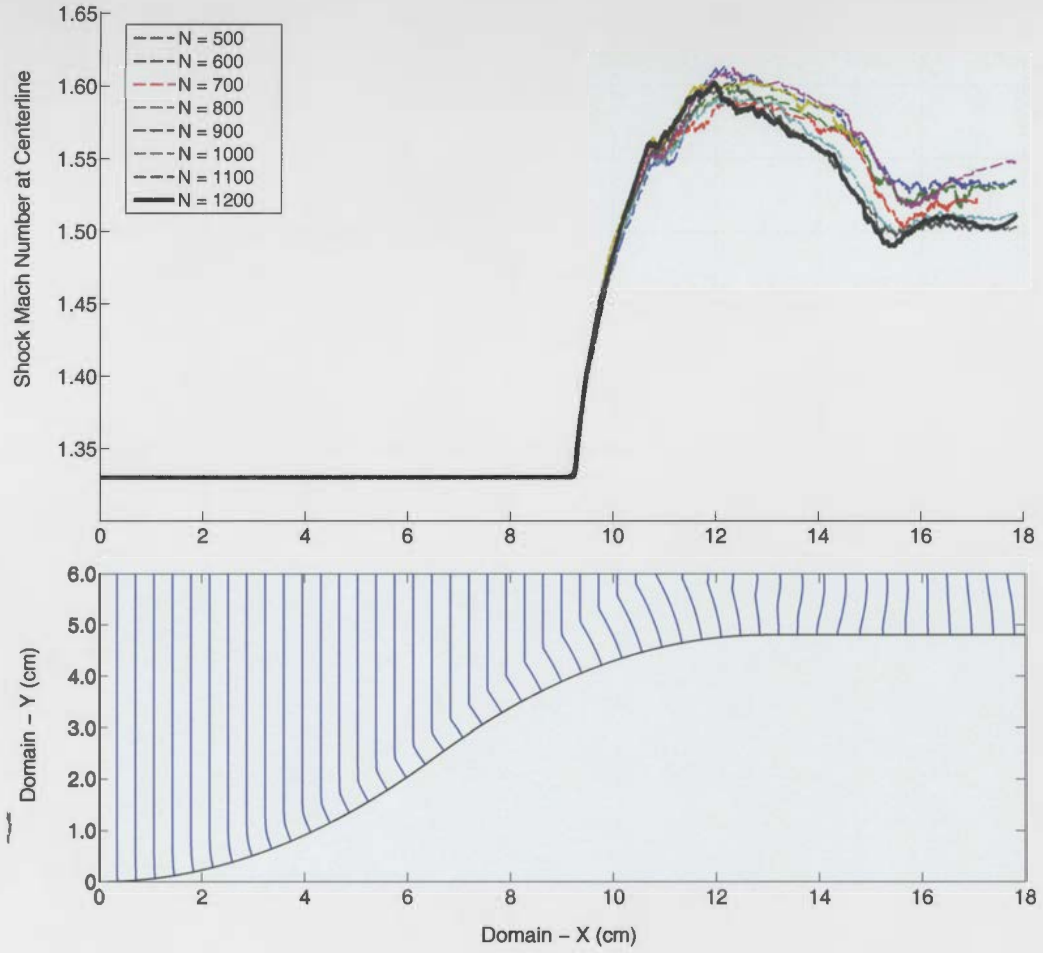

Figure 5.14: Comparison of the absolute shock Mach number at the centerline of the test section with a time–lapse plot of the shock development for a 130mm profile

Figure 5.15 shows an example of the implications of reducing the frequency of numerical dampening to dampen once every 25 time steps. Although the simulation is within the original recommended frequency of between 10 – 50, the rapid degradation of the solution is particularly apparent when addition or deletion of data points is required.

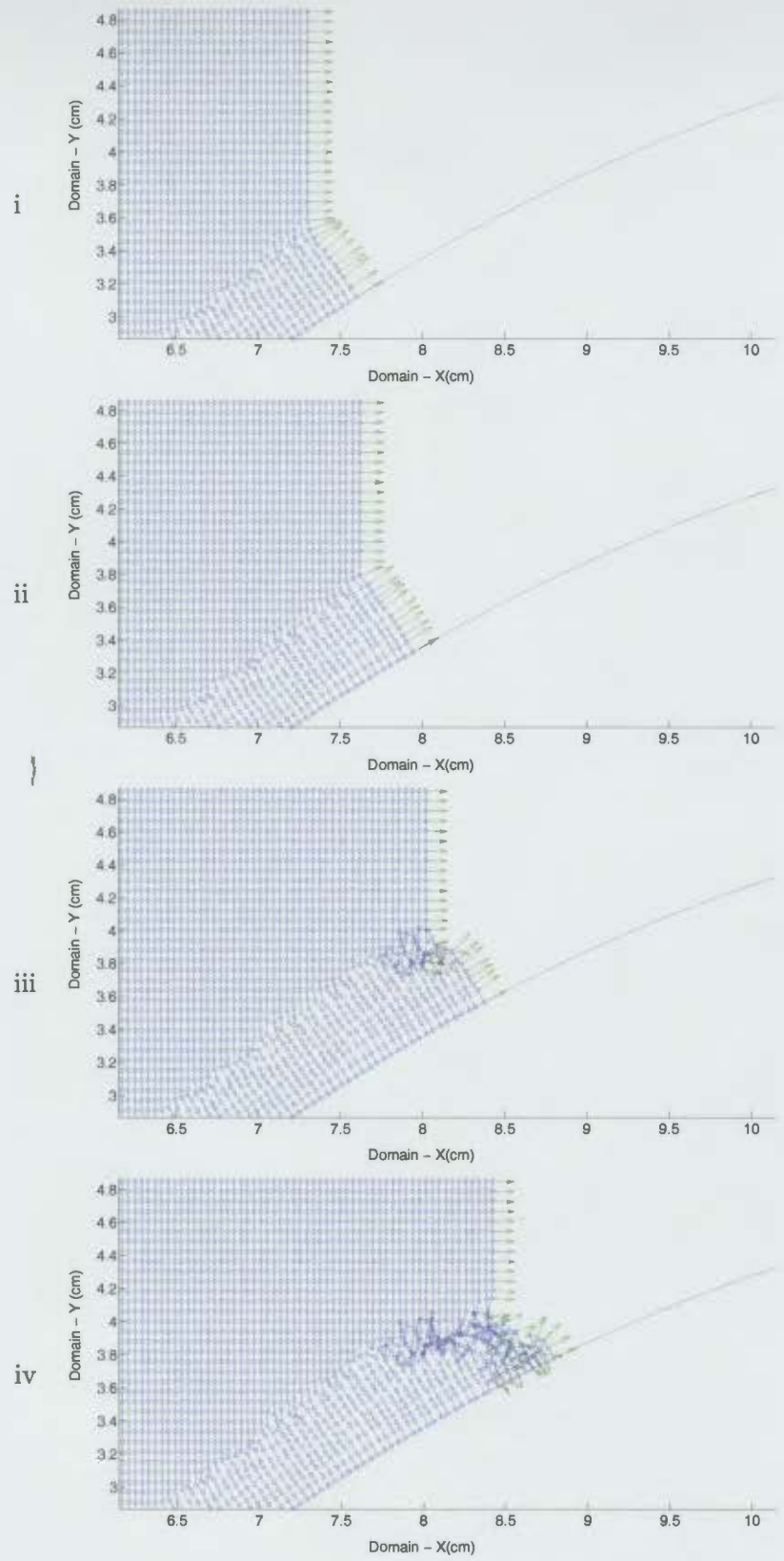

Figure 5.15: The effects of insufficient numerical dampening from a 130mm profile ($N = 100, K2 = 0.5$) MATLAB numerical simulation

6 Results and Discussion

From the literature reviewed it has already been shown that for higher Mach numbers ($M_s > 2$) theoretical predictions using the CCW Model together with Whitham's Theory using geometrical shock dynamics proves quite useful in predicting the strength and shape of the transmitted shock wave. But of particular interest is the analysis of a gradual area reduction whereby a relatively weak shock wave may be optimally strengthened over a certain distance.

When considering a shock wave approaching a change in area from A_1 to A_2, the geometrical method of connecting these areas is via a profile consisting of symmetric inclined straight surfaces. In practice though, a shock wave impinging on a sudden angled straight incline is expected to transition to Mach reflection in response from the flow to the sudden change in boundary conditions. The formation of a reflected shock is undesirable considering the associated losses and an increase in entropy of the system. In order to prevent or minimize the onset of transition of the flow, a higher function defining the profile wall which provides a seamless transition to smooth out the entrance and exit properties of the profile is required. Hence, the two step parabolic profile providing an optimal gradient for a given profile length was chosen for further numerical and experimental analysis.

The initial CFD simulations provided an overview of the expected flow features and a basis for the profiles to be manufactured for experimental testing. Of particular interest was the results obtained for a profile length of 130mm, 195mm and 260mm, with a percentage area reduction of 80% and initial Mach number of $M_s = 1.4$. For the 130mm profile it was clear from the observations shown in figure 5.1 that the flow was expected to transition to a simple Mach reflection whilst still within the profile section. Once the shock had propagated into the reduced section it would be followed by distinct reflected shocks expanding both upstream and downstream. In contrast, the simulations for the longer 260mm profile given in figure 5.3 does not show the shock transitioning at all and is instead accompanied by strong compression waves. Finally, the 195mm profile from figure 5.2 presented a situation in between where it was uncertain whether the flow had transitioned to Mach reflection or not but still presented a mixture of reflected shock waves and strong compression waves. The uncertainty can be attritubed to the lower resolution of the mesh and refinement criteria assigned for the initial simulation. Results from additional simulations conducted with alternative profile parameters as listed in table 4.1 will be discussed at a later stage in this section.

Results from experimental testing presented in figures 5.4 through to figure 5.10 showed three types of flow patterns observed. For each image the approaching shock as it entered the profile had an approximate initial Mach number of $M_s = 1.33$. Considering the shortest 130mm profile, from figure 5.4a)ii., it is clear by this point the shock has indeed transitioned to Mach reflection where a strong shear layer is present. The shear layer at this point half way up the profile is positioned almost parallel with the profile surface but angled slightly towards the surface indicating a stable Mach reflection. The tapering away of the profile in later images 5.4a)iii and iv allow the triple point to continue its path moving away from the profile surface where it eventually intercepts its symmetrical twin from the opposite profile and is reflected/transmitted back toward the profile surface. The initial positioning and motion of the triple point from these experimental results compares similarly with later produced revised CFD simulations.

Similar to the initial CFD simulation, the longest 260mm profile [figure 5.4c)i. – iv.] provides a gentle enough gradient that the flow is not required to transition to Mach reflection. Instead, the light shading of colour behind the shock as it propagates up the profile is almost evenly distributed along the length of the shock front. The lightness in colour and even distribution indicates that the shock and post-shock flow is able to easily adjust to the gradual changing boundary conditions where the density build–up is distributed along the shock front. The shock is required in figure 5.4c)iii to produce a relatively high curvature in order to satisfy the wall boundary conditions.

Finally, the shock development through the 195mm profile shows a strong compression wave developing behind the shock as it propagates up the profile. This is quite evident by the much stronger colours present in figure 5.4a)ii. and iii. On interception at the symmetry plane, the shock then transitions to Mach reflection which is more clearly seen later in figure 5.5b) near the profile exit. Note: The presence of very small weak perturbations propagating into the flow for each test is due to very thin perturbation tape placed on the profile at 25mm intervals for diagnostic purposes. Due to the high level of complexity of the flow as the shock entered the reduced section, the perturbations and their origins were rendered useless as they were impossible to track.

From these experimental results it can be concluded that there can be three types of scenarios for the propagation of a shock through an area reduction. The first scenario occurs when the shock transitions whilst propagating up the profile itself; the second scenario occurs when the shock transitions due to interaction/reflection at the symmetry plane; and the third occurs when transition is not reached at all.

The presence of either the first or second scenario results in reflected shock waves and shear layers being formed. These propagate downstream behind the transmitted shock in the reduced channel and can be seen in figure 5.6 and figure 5.8. In both cases, the reflected shock wave (and its mirror) propagate behind the transmitted shock expanding cylindrically upstream and downstream. Due to the expansion and interaction with its mirror, the reflected shock weakens over time. In figure 5.6.ii, the reflected shock can still be seen affecting the curvature of the transmitted shock indicating that the transmitted shock cannot be considered planar in shape yet and that the strength of the reflection is comparable to the transmitted shock itself. With each reflection across the shock front, a set of mirrored shear layers are produced in an alternating 'zig–zag' fashion. These sets of shear layers appear to separate from each other uniformly and become unstable and breakdown whilst moving along the reduced channel. The degradation into Kelvin-Helmholtz instabilities with their characteristic 'cat's eye' is shown in detail in figure 6.1 below.

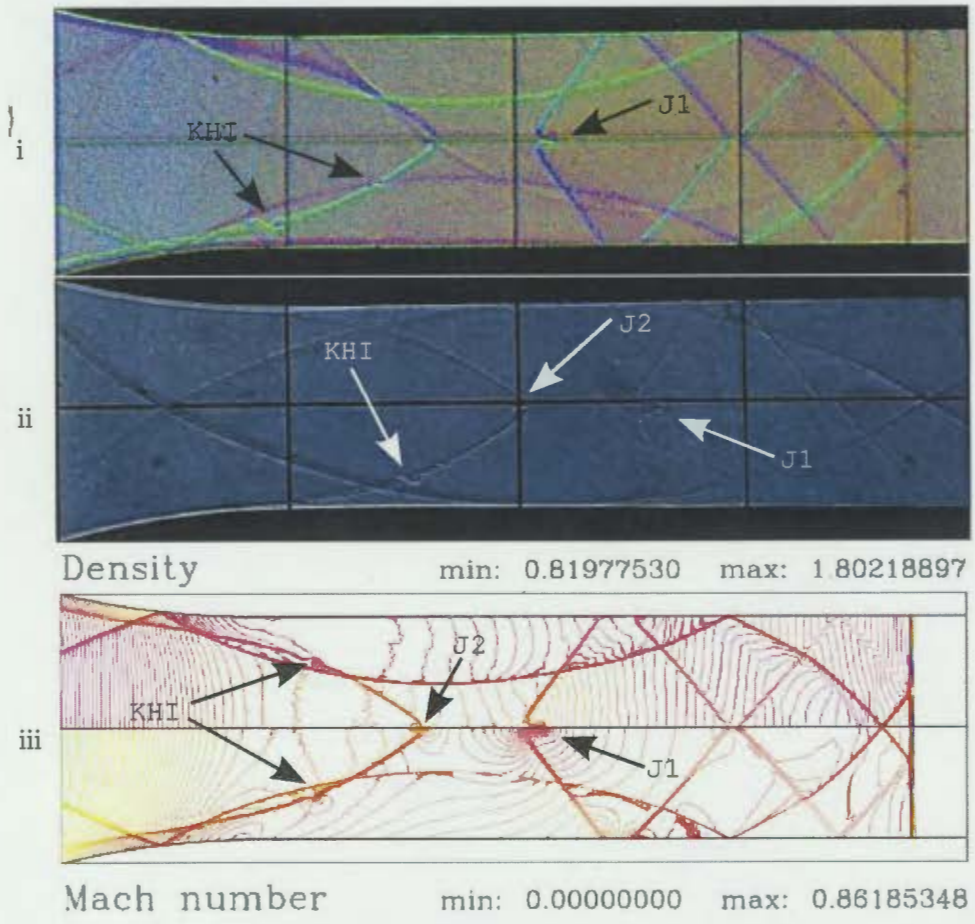

Figure 6.1: Comparison of similar initiation of Kelvin-Helmholtz instability and centerline jets for a 130mm profile for a $M_i = 1.33$

Figure 6.1 shows the flow conditions for a 130mm profile just after the profile exit where the first vertical wire on the left indicates the edge of the profile. The top two images are from Schlieren and shadowgraph images respectively and both present an interesting anomaly indicated on the figure by 'KHI'. At this position it appears that a Kelvin-Helmholtz instability has been triggered by an event, but looking on the opposite corresponding shear layer there is no such sudden relative large, unaccounted for instability. In later images this instability grows quite considerably to the extent that it is large enough to interact at the boundary wall. The bottom image of figure 6.1 shows a fifth–order MUSCL numerical plot produced by Ivanov et al. (2012) which appears to be reproducible but with a slight shift in space which Ivanov et al. attributes to the influence of the additional contact surface present in the experiments. Figure 6.1 also shows two jets: a downstream facing jet 'J1' and upstream facing jet 'J2'. Quite later on down the channel the downstream jet also destabilizes into a large split K-H instabilities whereas since J2 is facing upstream into a higher density flow its propagation remains. The presence of these jets at the centerline are a combination of the shear layers breaking down when they meet at the centerline and consequently the higher velocity local flow pushing through into neighbouring sections. The 130mm profile reduced section videos show quite clearly the continued breakdown of the Kelvin-Helmholtz instabilities such that near the instability near the boundary wall has grown significantly but 'appears' stable in its growth/expansion as it propagates downstream. Figure 6.2 shows a cropped view from figure 6.3 for a high–resolution picture clearly showing the advanced decay of the shear layer.The stronger downstream facing jet 'J1' shows to degrade and form recirculating flow around it's mushroom cap. The recirculating flow also tends to break down noticeably and in some cases forms new KHI's. The next cycle of shear layers can be seen to follow the same process of destabilisation and decomposition into KHI's and jets as described above.

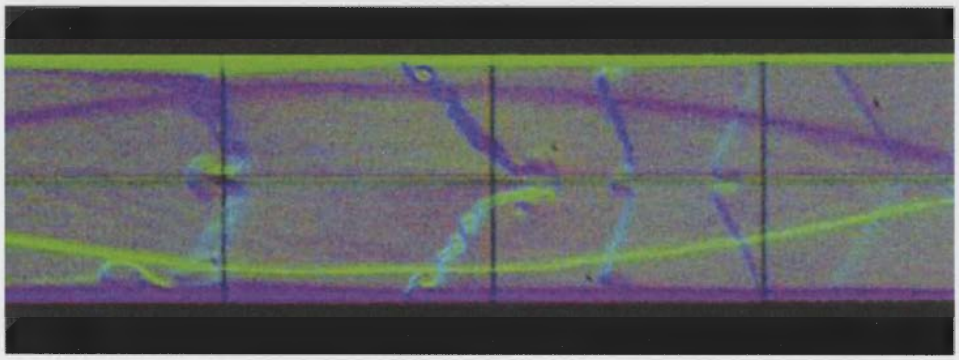

Figure 6.2: 130mm profile in reduced section crop showing advanced shear layer break-down for an initial M = 1.33 shock

For a look at the rapid destabilization of the shear layer and the accompanying jets within the reduced channel, refer to the high–speed video in Appendix – A recorded for the 130mm profile. Due to the low sensitivity of the high–speed camera and short exposure times the required light for the camera's sensor did not allow the setup to fully resolve all the flow features behind the shock. Instead the lenses and iris cut–off were setup to allow light through for large shifts in densities. In both the 130mm and 195mm profile videos, the destabilization of the shear layer and the accompanying jets and their development can be seen very clearly. The progression of which can also be seen to move quite uniformly along at the local the stream velocity within the reduced section. The high-speed videos within the reduced sections for the three profiles, clearly show bright green boundary layers and the subsequent break-down into turbulence further away from the profile sides.

The video captured by the high–speed video camera proved incredibly useful including a simplistic approach to capturing multiple frames of the same test with respectable image resolution. By cropping consecutive frames (figure 5.9) this has allowed an easy method to estimate the speed of the shock front from a stationary reference relative to the test section and profile. For future considerations it would then be possible to use this method to measure the relative speed of the accompanying flow features.

Figure 6.3 shows a direct comparison between the recorded experimental and CFD guage pressures on the symmetry plane/centerline for three pressure tappings and a 130mm profile.

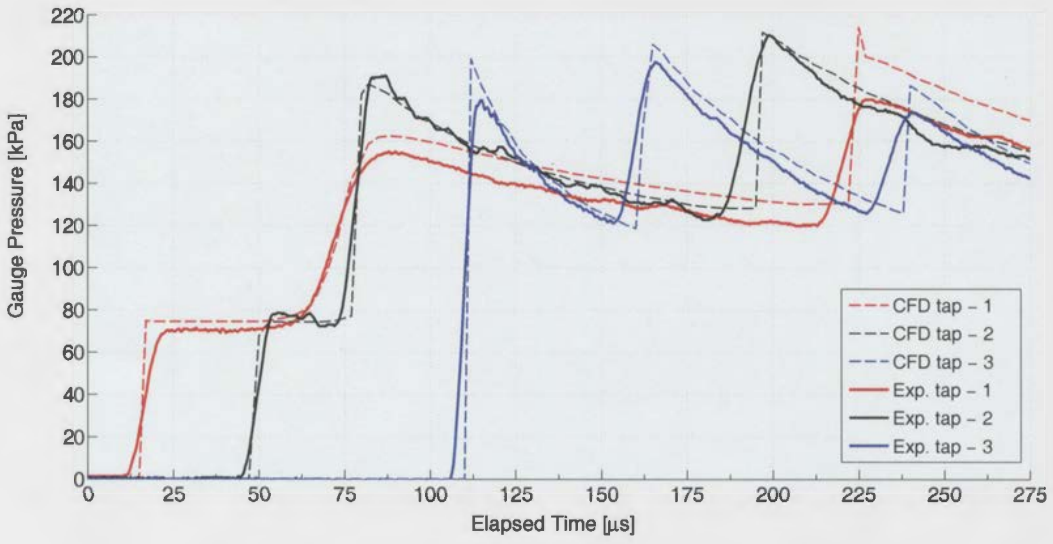

Figure 6.3: Pressure traces compared between experimental and CFD results for a 130mm profile

The simulation depicted in figure 6.3 represents the revisited CFD results where the computational mesh and refinement criteria was reduced. From 6.3 the pressure readings shows to correlate well at pressure tappings 2 and 3, but there is some discrepancy with magnitudes at pressure tapping 1. This can be attributed to the fact that pressure transducer 1 had a linearity of 41%FS which is exceedingly high and would result in the variability seen. Other than this issue, the revisited CFD and experimental pressure traces correlate well which gives further relaibility to the CFD findings depicted next in figure 6.4.

Results from CFD findings, experimental estimation and theoretical predictions using Milton's (1975) modified version of the CCW relation have been plotted in figure 6.4. For lower percentage in area reductions of 40% and 60% the CFD findings for either size profile of 130mm or 260mm are in good agreement with the theoretical predictions. Whereas looking at much higher area reductions of 80, 90 and 95% a larger difference between CFD and theoretical results is apparent where the shorter 130mm shows a 5% lower transmitted shock strength.

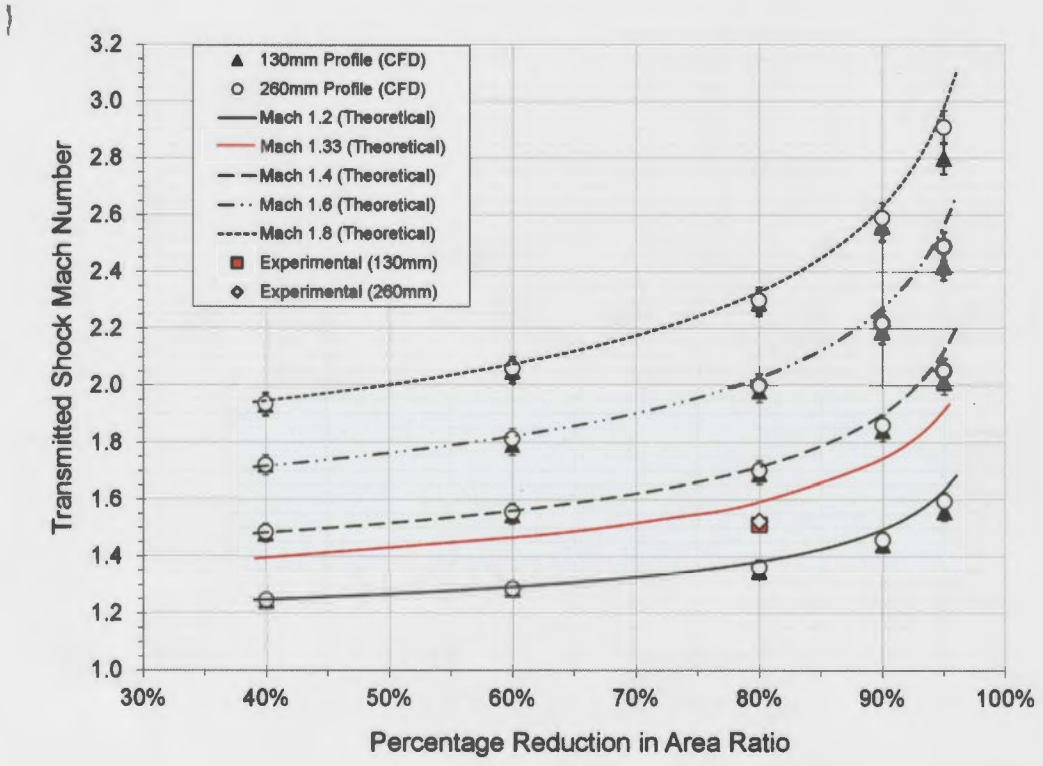

Figure 6.4: Comparison between theoretical predictions and extracted CFD results for the transmitted shock Mach number in the reduced channel

The differences at high percentage area reductions with shorter profile lengths is a result of the fact that the CCW Relation neglects the change in entropy across the area change which will be quite significant in these cases. The experimental transmitted Mach number was calculated using the high–speed camera and speeds of M1.51 for 130mm and 195mm profiles, and M1.52 for the longer 260mm profile were calculated which represents a net gain of 12.7%. Comparing these values with the theoretical curve they fall below the predicted transmitted Mach number of M1.594 for $M_s = 1.33$ shock at 80% reduction in area. Therefore, theoretical predictions based on Milton's (1975) modified Whitham's Theory over predict the transmitted Mach number (for worst case of 130mm profile) by a factor of 1.051, or within 5.1% of experimental results. This compares almost exactly with Russell's (1967) results where strengthened shock speeds at the exit of the convergence also agreed to within 5% of results obtained from the CCW model.

Figure 6.5 shows that the difference in pressure ratio for the extended profile simulations. After 0.1m from the profile exit the difference of 1.5% continues to increase to 4.2% after 0.8m. This can be attributed to the stronger transverse waves propagating against the transmitted shock retarding it due to the subsequent expansion wave. This could be important when considering if the application of the area reduction is to increase strength across the shock after a certain distance as it then becomes much more beneficial using a longer profile.

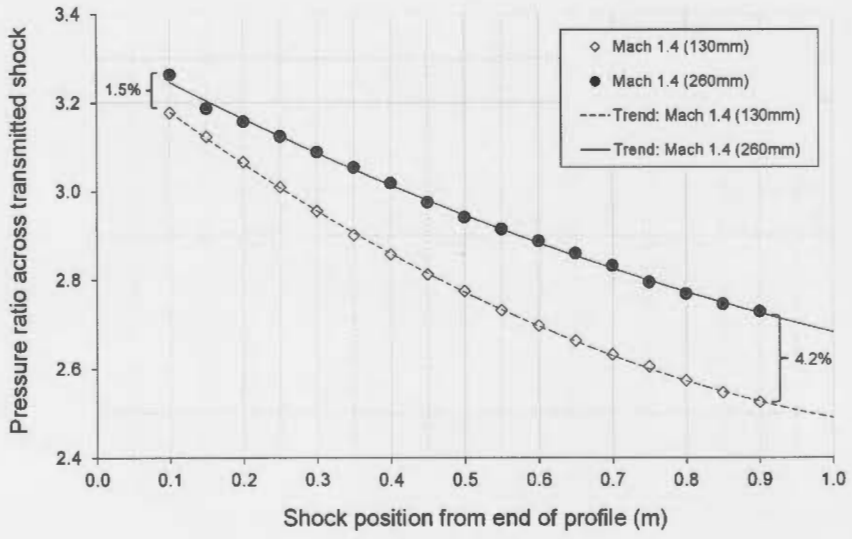

Figure 6.5: Results from extended channel simulations comparing relative shock decay between 130mm and 260mm profiles

The MATLAB numerical scheme developed by the author was based on Henshaw et al.'s (1986) numerical shock–tracking scheme and utilised Milton's (1975) modified version of the CCW Relation as the principal Mach–Area relation. The simulations proved to be very unpredictable when numerical dampening was not used after every time–step. In most cases Using Henshaw et al.'s (1986) recommended $10 - 50$ time–step frequency resulted in figure 5.15 and thus a failed result. Without the smoothing effect of the numerical dampening, the calculated $t + \Delta t$ coordinates were highly susceptible to numerical noise. Considering the addition of the added η factor for the M–A relationship from Milton was for the intention of accounting for post–shock flow reflections, this correction term is assumed be main contributor, if not the source, of the excessive noise and instability inherent in the code.

Figure 5.13 and 5.14 show a sample set of results produced from the MATLAB scheme and figures 6.6 and 6.7 show the overall results for all three profiles. Provided numerical dampening was used every time–step, the program was able to fairly accurately track the development and progress of a triple point from a Mach reflection. Although, from figure 5.14 where the Mach number is taken from the symmetry plane, the Mach is shown to sharply increase before the triple point reaches this plane. One reason for this anomaly is that pressure waves ,originating from the leading edge of profile, are travelling ahead of the triple point up the shock front and intercepting the symmetry plane before the triple point. But still, this is counter intuitive from what is shown in the experimental and CFD pressure traces (figure 6.3) where the pressure rises almost instantaneously. From Henshaw et al.'s (1986) numerical method, the definition of the triple point is reliant on both the points above and below the triple point being deleted or added which subsequently alters the curvature of the shock. This change in curvature together with constant numerical dampen may be causing this pseudo–compression wave ahead of the triple point resulting in the premature increase in the Mach number.

It was also found from the pressure plot that once the triple point reflected off the symmetry plane it's definition tended to become less predictable at being clearly tracked. This can be attributed to the intense numerical dampening present in the code resulting in smoothing out of the shock the moments the triple point reflects off the symmetry plane and subsequently the profile surface. Hence, the shock tends to stabilise to a planar shock much quicker compared to experimental and CFD results.

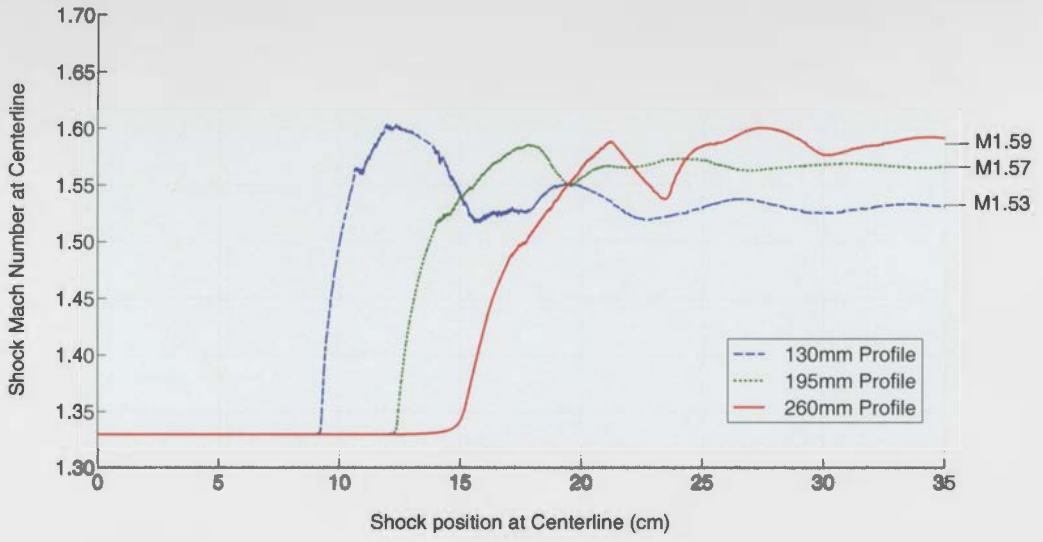

Figure 6.6: Comparison of MATLAB results for the shock Mach number at the centerline for 130, 195 and 260mm profiles

In the 260mm simulation a slight 'kink' is seen in figure C.7 but quickly dissipates after intercepting with the symmetry wall. The presence of this randomly developed triple-point may indicate issues in tracking slightly largely curved shock waves without deleting points resulting in the formation of a Mach reflection. The transmitted Mach number for the three profiles varies from M1.53, M1.57 to M1.59 for the 130, 195 and 260 profile respectively. At the higher end the MATLAB results for the 260mm profile compares well with the theoretical trend presented in figure 6.4 but at the lower end the 130mm profile's M1.53 is more in line with experimental results.

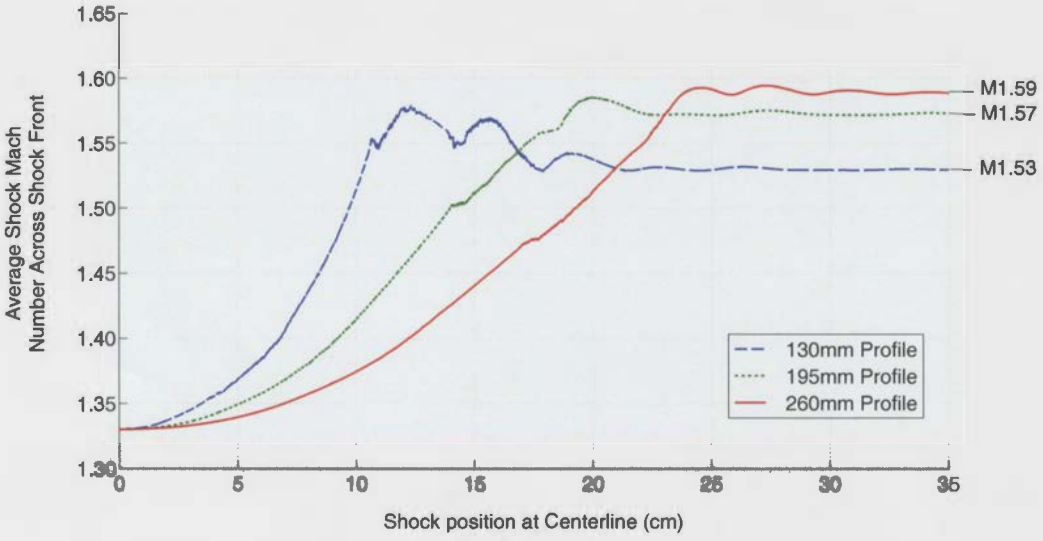

Figure 6.7: Comparison of MATLAB results for the average shock Mach number across the shock front for 130, 195 and 260mm profiles

In summary, this discussion has looked at the design of the profile and the initial CFD simulations conducted to provide a basis for experimental testing. The three types of scenarios were detailed according to the three different forms of shock propagation through each profile. The instabilities produced from scenarios one and two were discussed and the revisited CFD were shown to have good correlation with experimental pressure traces. The overall transmitted shock Mach number for various initial shock Mach numbers, profile length and percentage area reduction were presented. Finally, shock decay based on profile length and results from the MTALAB numerical scheme were presented.

7 Conclusions

In addressing the original objectives presented previously in section 2 the following conclusions have been drawn from the analysed results.

- In order to provide an optimal wave amplification or to maximize the strength of a transmitted shock wave, the formation of a reflected shock wave needs to be avoided. From the analysed results it can be concluded that there can be three types of scenarios for the propagation of a shock through an area reduction. The first scenario occurs when the shock transitions to Mach reflection whilst propagating up the profile itself; the second scenario occurs when the shock transitions due to interaction/reflection at the symmetry plane; and the third occurs when transition is not reached at all. The optimal strength of the transmitted shock wave occurs for the third scenario.

- The development of the shock and whether transition to Mach reflection occurs depends on the gradient of the profile and the rate of information transmitted into the post–shock flow. It was found that for the relatively weak shock waves tested, it took the transmitted shock from the shorter 130mm profile longer to become planar because the reflected shock was comparable in strength to the incident shock even once propagating into the reduced channel.

- When comparing experimental transmitted shock Mach numbers to theoretical predictions using a modified version of the CCW Relation and a numerical shock–tracking scheme, the theory predicted the transmitted Mach number within 5% of the worst case scenario for a 130m profile. In all cases the theoretical prediction over-estimated the Mach number expected.

8 Recommendations

The research presented in this dissertation on area effects on shock wave propagation details mainly on shock wave strengthening by area reduction for relatively weak shock waves of $M_s > 1.0$. The following points for study are recommended to further work in the study of area change effects on shock wave propagation.

- Investigate the effects of varying the rate of compression across the profile by adjusting the point of inflection.
- Investigate the area change effects for strong and weak shock waves propagating through a gradual area expansion. By reducing the shock wave strength accurately by area expansion, a very weak shock wave may be reliably produced for testing very weak shock phenomena.
- Further experimental analysis is required into the effects of a gradual area reduction for very weak $M_i \approx 1$ and very strong $M_i > 2$. The results of which may be compared to the current study for any correlation.

References

Ben-Dor G., Igra O., Elperin T., Lifshitz A. (2001) *Shock Wave Interaction and Propagation*; Handbook of Shock Waves; vol. 2.

Bird G.A. (1959) *The effect of wall shape on the degree of reinforcement of a shock wave moving into a converging channel*; Journal of Fluid Mechanics; vol. 5, no. 01, pp. 60–66.

Chester W. (1953) *The Propagation Of Shock Waves in a Channel of Non-Uniform Width*; The Quarterly Journal of Mechanics and Applied Mathematics; vol. 6, no. 4, pp. 440–452.

Chester W. (1954) *CXLV. The quasi-cylindrical shock tube*; Philosophical Magazine Series 7; vol. 45, no. 371, pp. 1293–1301.

Chisnell R.F. (1957) *The motion of a shock wave in a channel, with applications to cylindrical and spherical shock waves*; Journal of Fluid Mechanics; vol. 2, no. 03, pp. 286–298.

Han Z., Yin X. (1993) *Shock dynamics*; *Fluid Mechanics and Its Applications*, vol. 11; Science Press, Beijing.

Henshaw W., Smyth N., Schwendemen D. (1986) *Numerical shock propagation using geometrical shock dynamics*; Journal of Fluid Mechanics; vol. 171, pp. 519–545.

Igra O., Elperin T., Falcovitz J., Zmiri B. (1994) *Shock wave interaction with area changes in ducts*; Shock Waves; vol. 3, no. 3, pp. 233–238.

Igra O., Wang L., Falcovitz J. (1998) *Non-stationary compressible flow in ducts with varying cross-section*; Proceedings of the Institution of Mechanical Engineers, Part G: Journal of Aerospace Engineering; vol. 212, no. 4, pp. 225–243.

Itoh S., Okazaki N., Itaya M. (1981) *On the transition between regular and Mach reflection in truly non-stationary flows*; Journal of Fluid Mechanics; vol. 108, pp. 384–400.

Ivanov I., Kryukov I., Dowse J., Skews B., Znamenskaya I. (2012) *Kelvin-Helmholtz Instability on Shock Wave Propagation*; 15th International Symposium on Flow Visualisation, 2012.

Khan Z., Skews B. (2009) *Area change optimisation for shock wave passage down a duct*; Final year project report; University of the Witwatersrand.

Milton B. (1975) *Mach reflection using Ray-Shock theory*; AIAA Journal; vol. 13, pp. 1531–1533.

Milton B., Archer R. (1996) *Conical Mach reflection of moving shock waves*; Shock Waves; vol. 6, pp. 29–39.

Oshima K. (1965) *Diffraction of a plane shock wave around a corner*; Rept. no. 393; Insitute of Space and Aeronautical Science, University of Tokyo.

Rosciszewski J. (1960) *Calculation of the motion of non-uniform shock waves*; Journal of Fluid Mechanics; vol. 8, no. 03, pp. 337–367.

Russell D.A. (1967) *Shock-wave strengthening by area convergence*; Journal of Fluid Mechanics; vol. 27, no. 2, pp. 305–314.

Seitz M.W. (2001) *Shock wave interactions with porous, compressible foams*; Ph.D. thesis; University of the Witwatersrand.

Skews B., Kleine H. (2008) *Unsteady flow diagnostics using weak perturbations*; Experiments in Fluids; vol. 46, no. 1, pp. 65–76.

Skews B., Kleine H. (2010) *Some developments in transient gas dynamics*; The South African Conference on Computational and Applied Mechanics, SACAM 10, Paper 006, 2010.

Whitham G.B. (1957) *A new approach to problems of shock dynamics Part I Two-dimensional problems*; Journal of Fluid Mechanics; vol. 2, no. 02, pp. 145–171.

Whitham G.B. (1958) *On the propagation of shock waves through regions of non-uniform area or flow*; Journal of Fluid Mechanics; vol. 4, no. 04, pp. 337–360.

Whitham G.B. (1959) *A new approach to problems of shock dynamics Part 2. Three-dimensional problems*; Journal of Fluid Mechanics; vol. 5, no. 03, pp. 369–386.

Whitham G.B. (1974) *Linear and Nonlinear Waves*; J. Wiley, New York.

Appendix A – Digital Content

The following list shows the directory for the layout of the folders (+) and any sub-folders (-) contained on the attached CD.

- Root folder
  - + Experimental Testing
    - 130mm - HS Video
    - 130mm - Images
    - 130mm - Shadowgraph
    - 195mm - HS Video)
    - 195mm - Images
    - 260mm - HS Video
    - 260mm - Images
  - + Manufacturing
    - 130mm profile
    - 195mm profile
    - 260mm profile
    - Flat Sections
    - Spacers
  - + Schlieren Optical Setup
  - + MATLAB Whitham Code
    - Figures

Appendix B – MATLAB Numerical Shock–Fitting Scheme

Figures B.1 to B.4 depict a summarised flow diagram for the Matlab coding of Henshaw et al.'s (1986) shock-fitting numerical scheme. The main MATLAB m-file 'whitham_main.m' with commenting and ancillary m-files can be found in Appendix A – Digital Content.

The parameters N and Δt are chosen by the general rules:

$$\text{Rule 1} \qquad \Delta s_{\text{avg}} = \frac{s_N(0)}{N} = K_1 \ll 1, \qquad \text{[B.1]}$$

$$\text{Rule 2} \qquad \frac{\Delta t}{\Delta s_{\text{min}}} = \frac{\Delta t}{d\Delta s_{\text{avg}}} < K_2, \qquad \text{[B.2]}$$

where $\Delta s_i(t) = s_i(t) - s_{i-1}(t)$ and d is the minimum tolerance on $\Delta s_i(t)$. Henshaw et al. (1986) recommends taking constants K_1 and K_2 equal to 0.01 and 0.2 respectively. Rule 1 provides adequate resolution of the shock front and Rule 2 is the Courant-Friedrichs-Levy condition and gives stability for all cases.

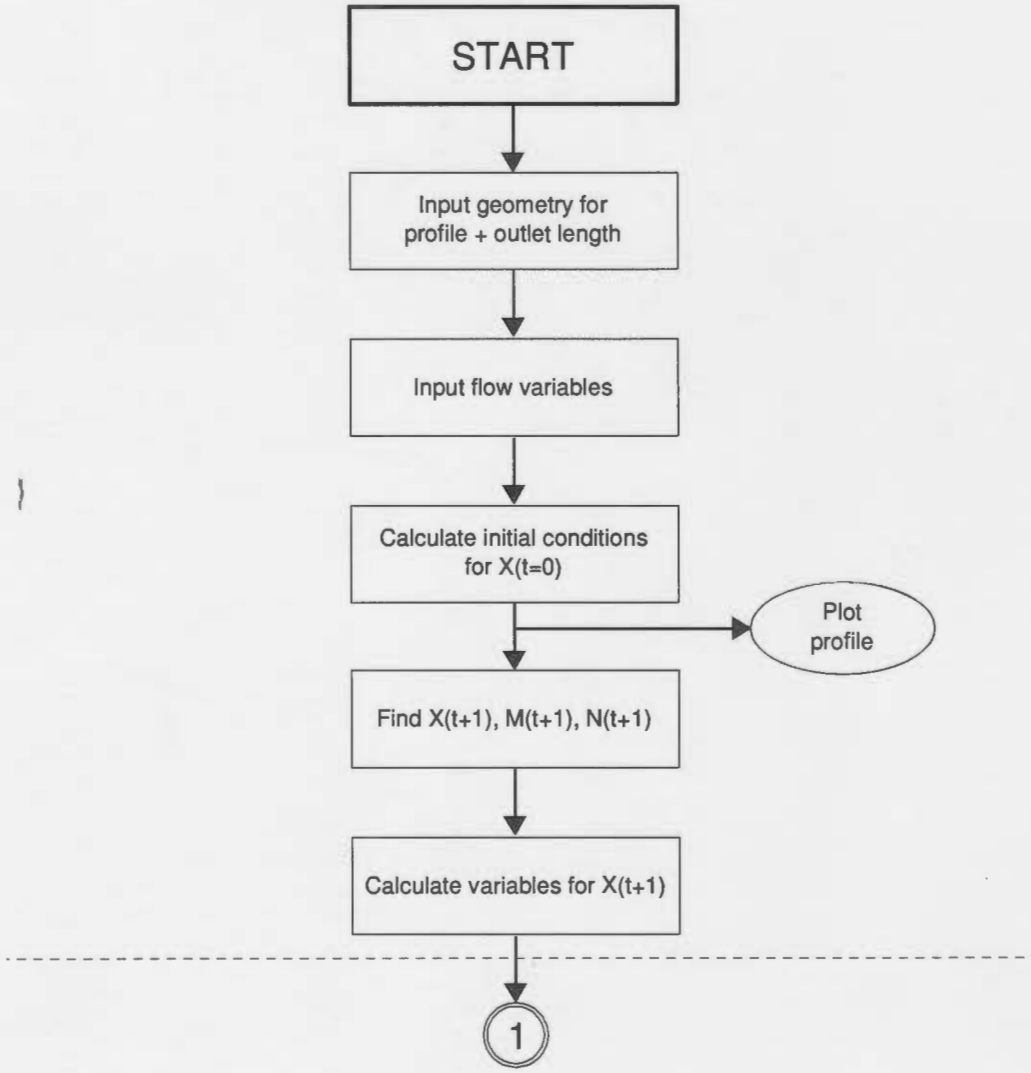

Figure B.1: MATLAB numerical code flow diagram - 1

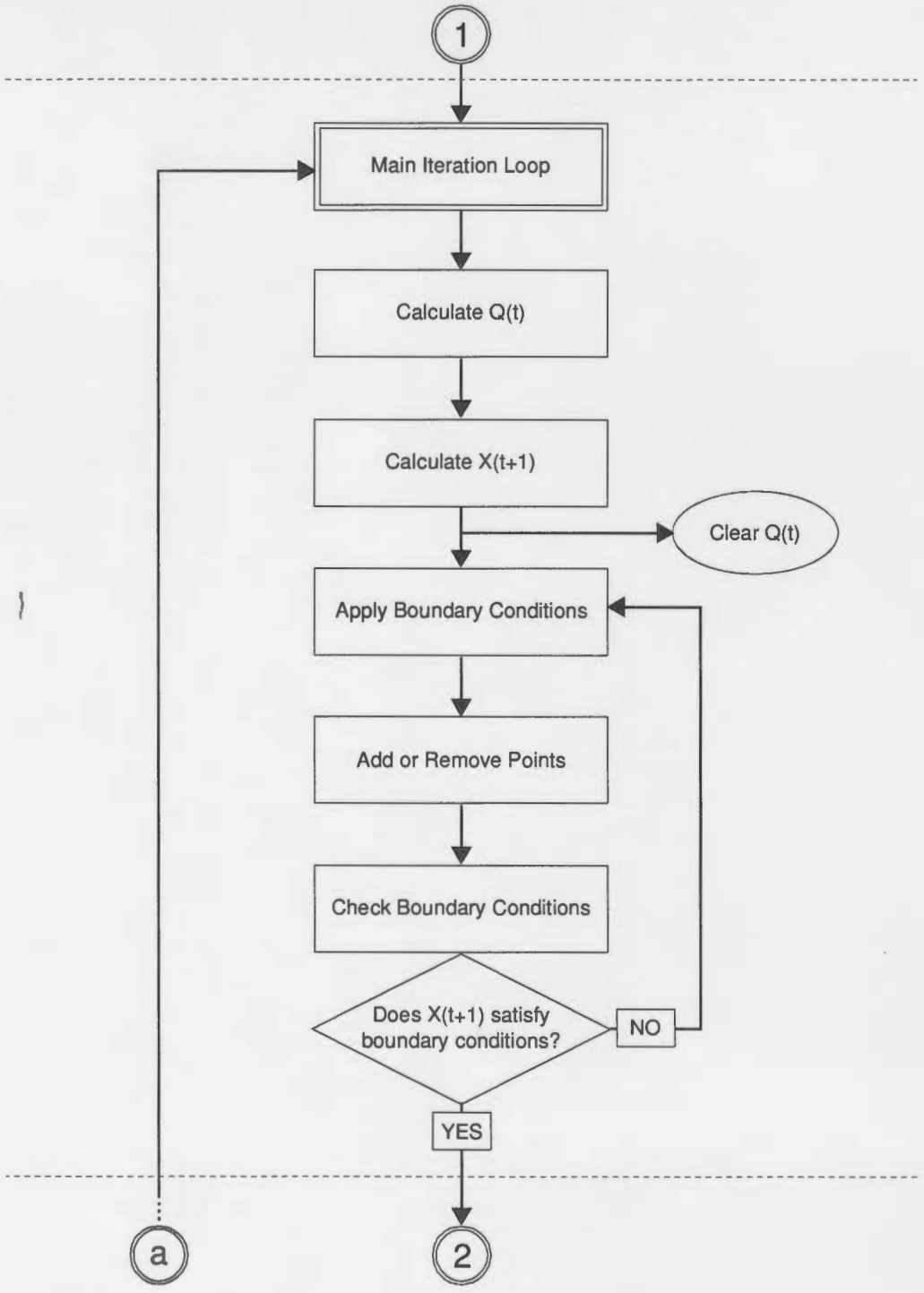

Figure B.2: MATLAB numerical code flow diagram - 2

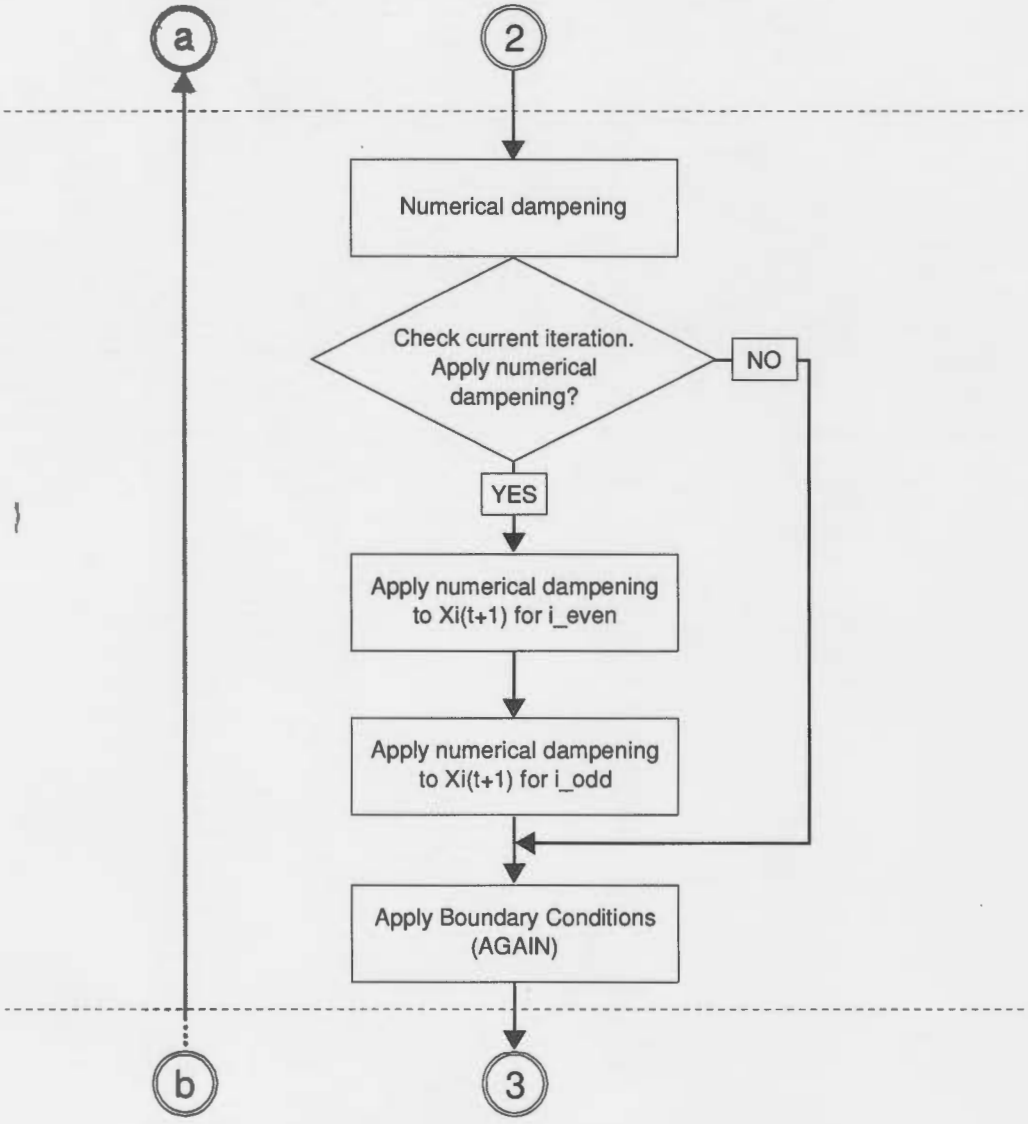

Figure B.3: MATLAB numerical code flow diagram - 3

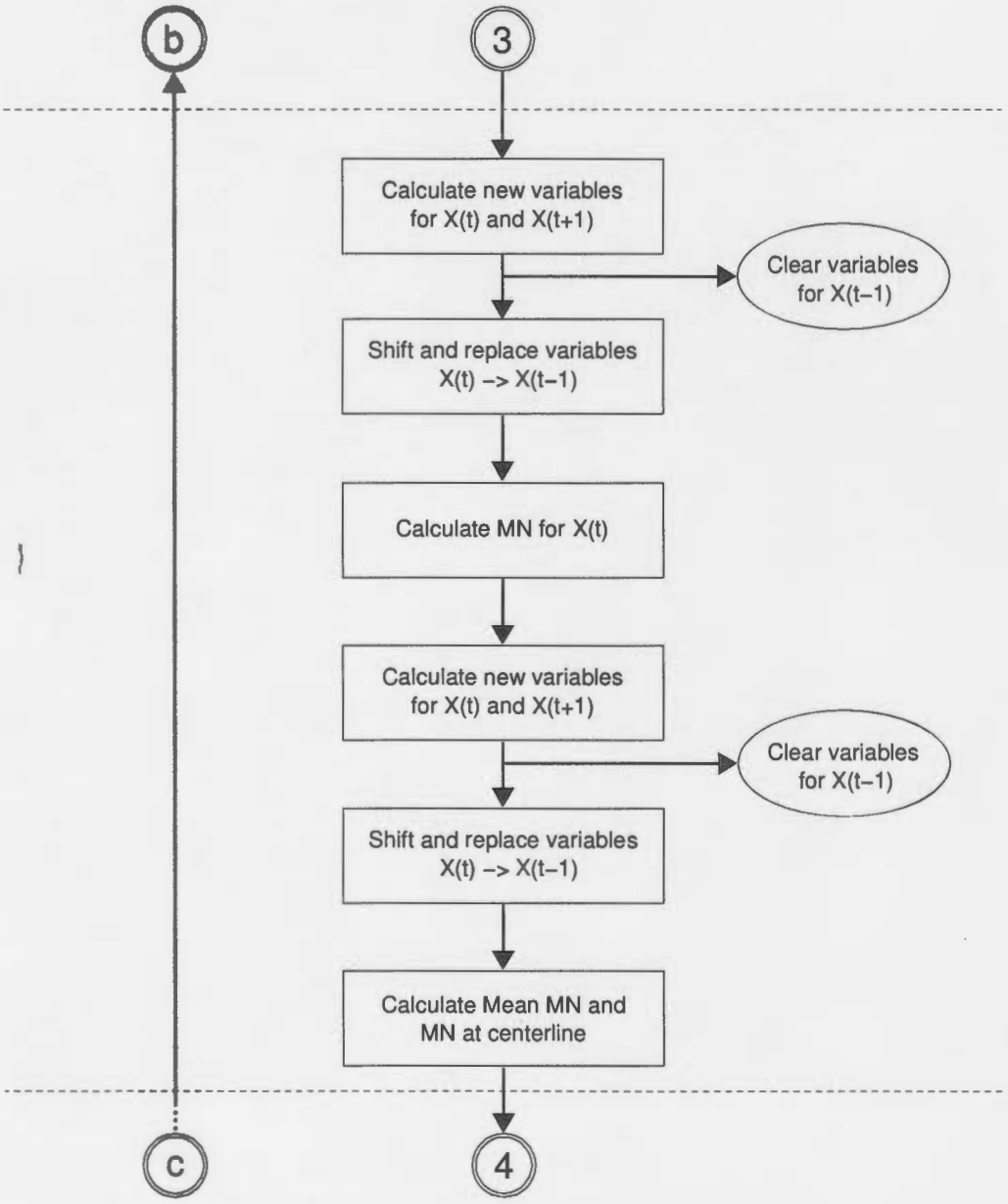

Figure B.4: MATLAB numerical code diagram - 4

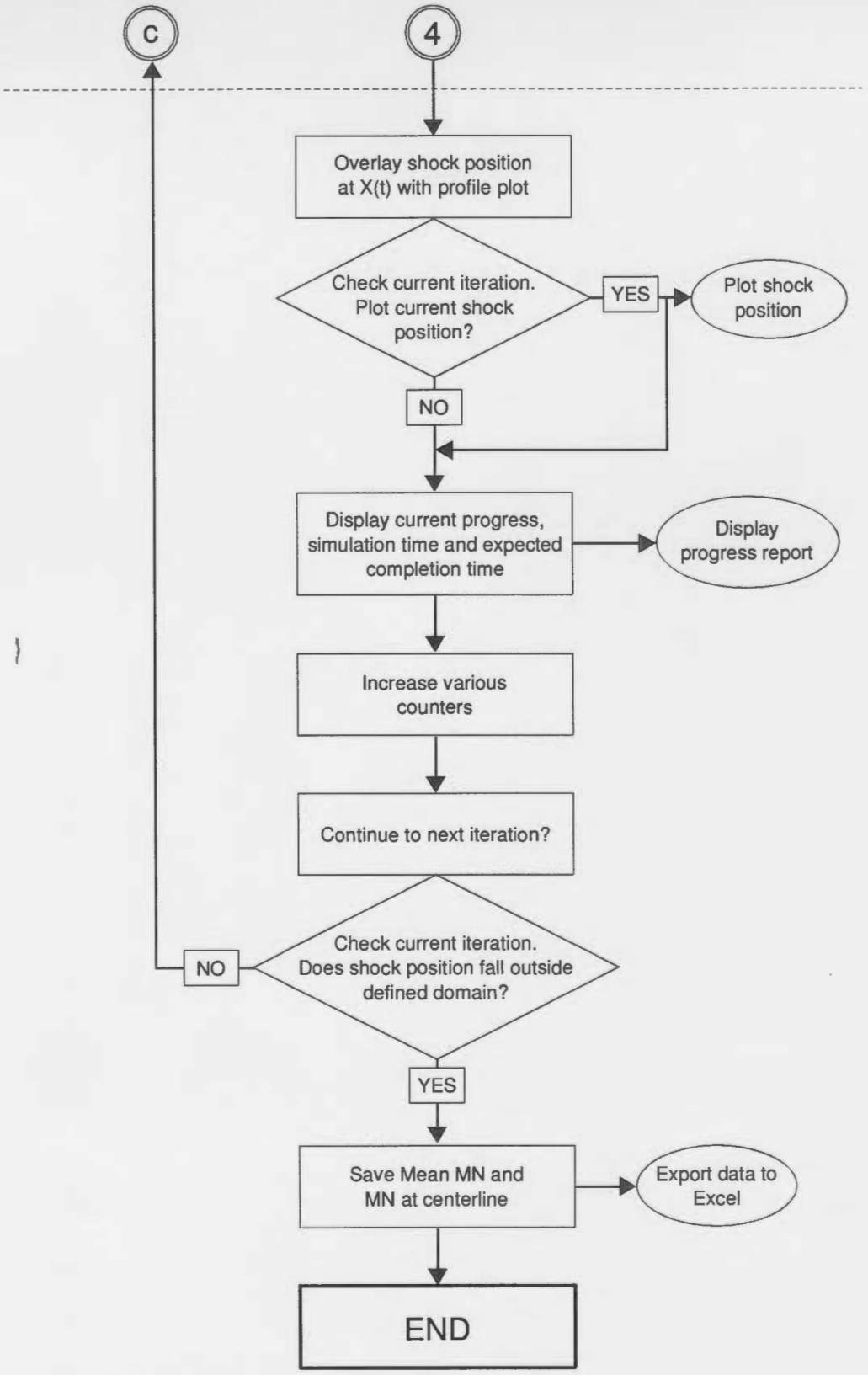

Figure B.5: MATLAB numerical code diagram - 5

Appendix C – Supplementary Results

C.1 CFD Results

In this section additional CFD results are provided in the form of figure C.1 and figure C.2 which compare the recorded experimental pressure readings and extracted CFD readings for 130mm and 195mm profiles respectively.

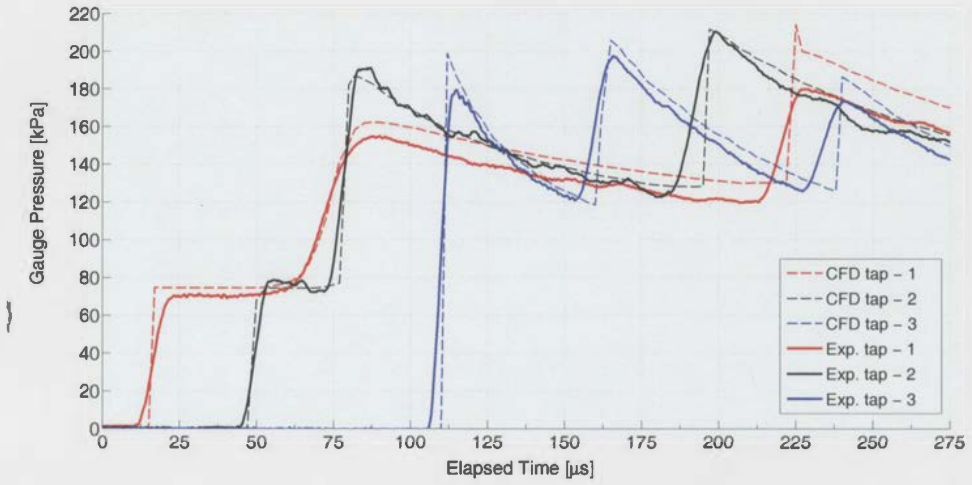

Figure C.1: Pressure traces compared between experimental and CFD results for a 130mm profile

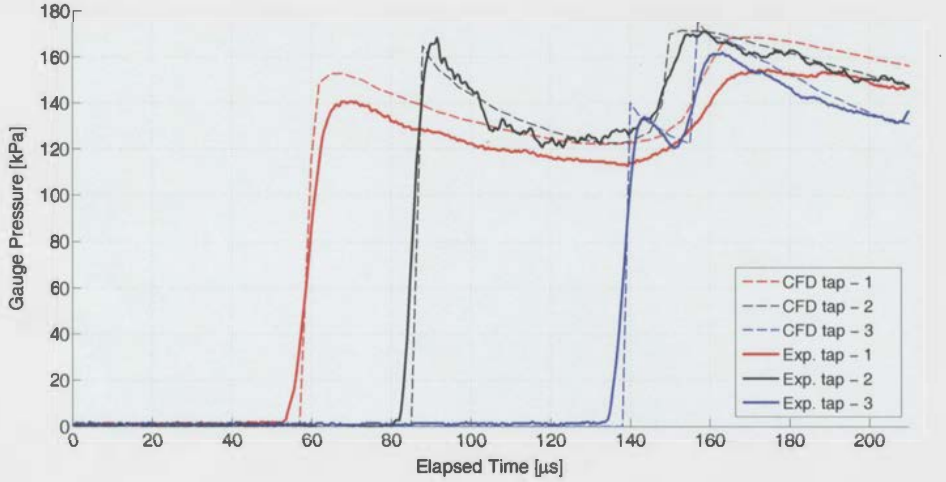

Figure C.2: Pressure traces compared between experimental and CFD results for a 195mm profile

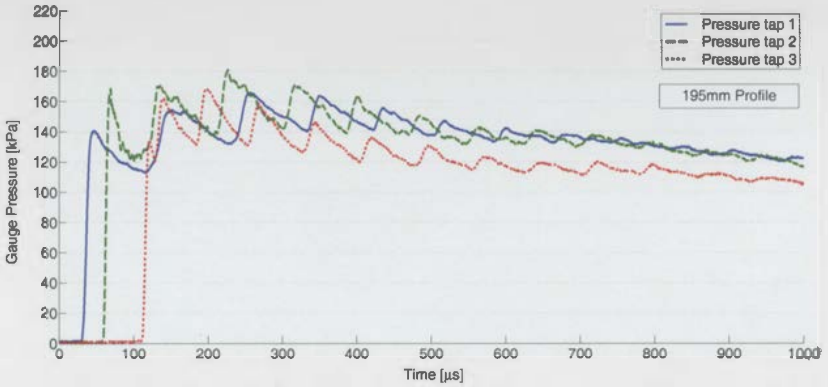

ht!]
Figure C.3: Pressure tracing for 195mm profile for three tappings situated on centerline of test section

C.2 Pressure Testing

This section provides additional information relating to the experimental pressure tests conducted. Table C.1 provides the calibration constants for the pressure transducers used for testing

Table C.1: Details for calibration constants for pressure transducers

Transducer No.	Serial No. S/N	Sensitivity [mV/psi]	Linearity [%FS]
1	6391	27.8	41
2	7937	24.39	1
3	8288	26	1

Figure C.3 and figure C.4 give the pressure (gauge) trace for pressure tappings situated within the profile section for 195mm and 260mm profiles respectively.

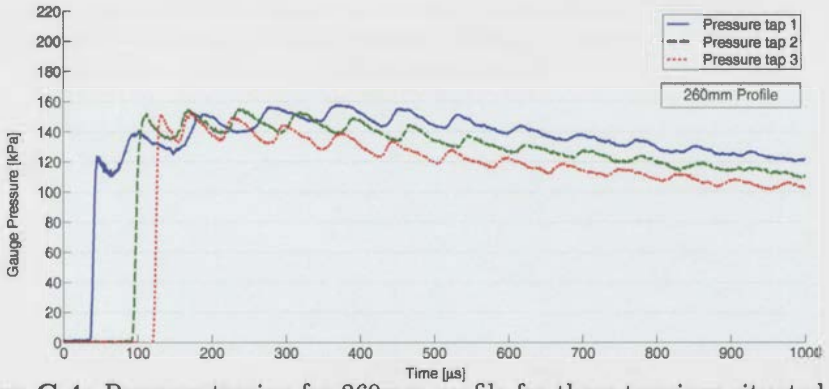

Figure C.4: Pressure tracing for 260mm profile for three tappings situated on centerline of test section

Figure C.5 and figure C.6 give the pressure (gauge) trace for pressure tappings situated within the reduced section for 195mm and 260mm profiles respectively.

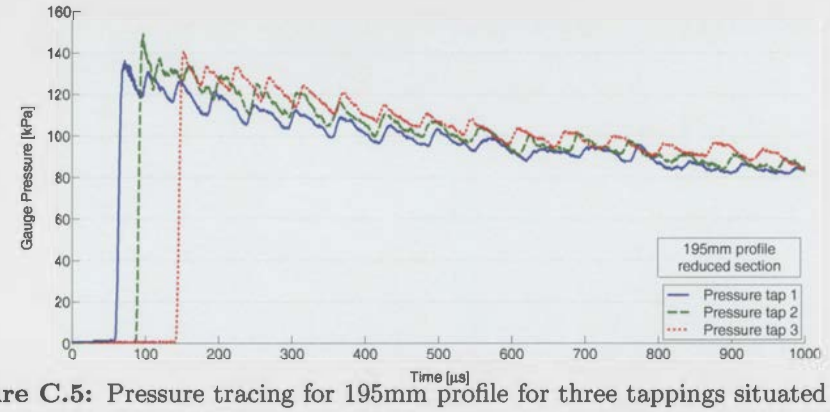

Figure C.5: Pressure tracing for 195mm profile for three tappings situated within the extended reduced section

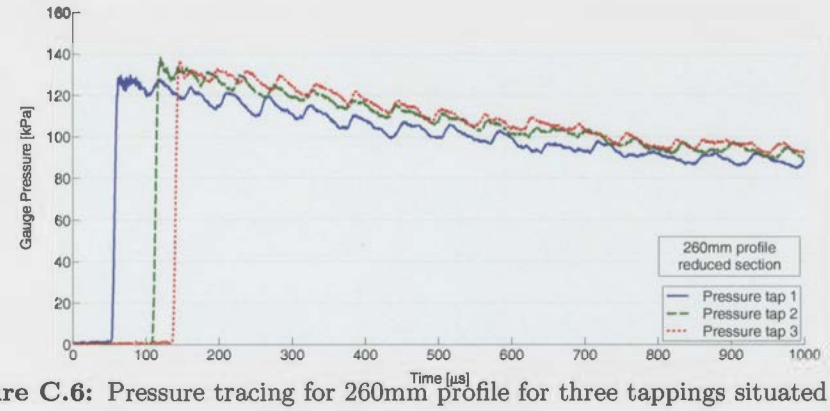

Figure C.6: Pressure tracing for 260mm profile for three tappings situated within the extended reduced section

C.3 MATLAB Results

Figures C.7 and C.8 provide the MATLAB results obtained for 260 and 195mm profiles. Each figure contains a set of three sub–figures namely the average shock Mach number (top), the Mach number across the centerline (middle), and the time–lapse profile plot showing shock propagation (bottom).

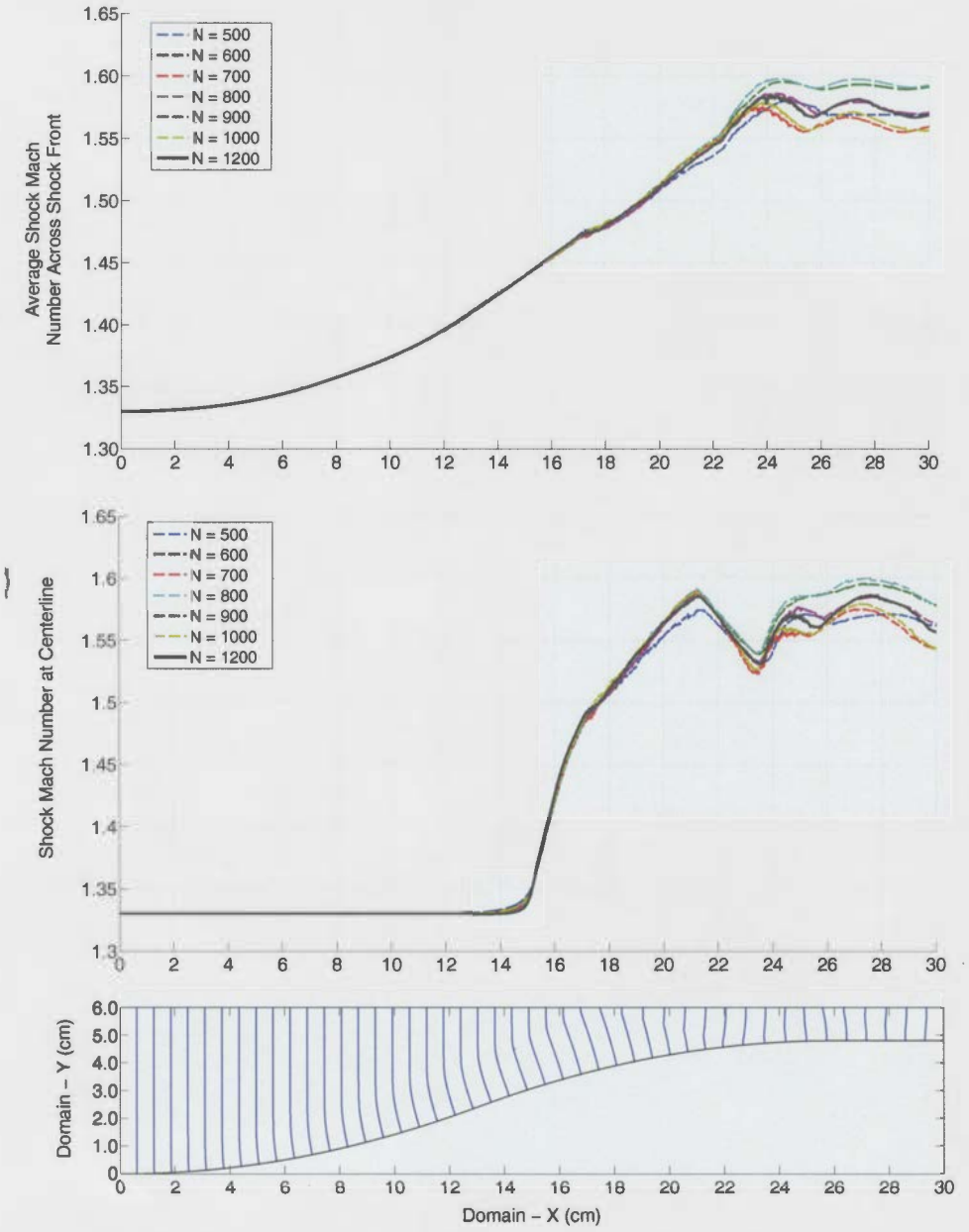

Figure C.7: Comparison of the average and absolute shock Mach number across the shock front and at the centerline respectively for

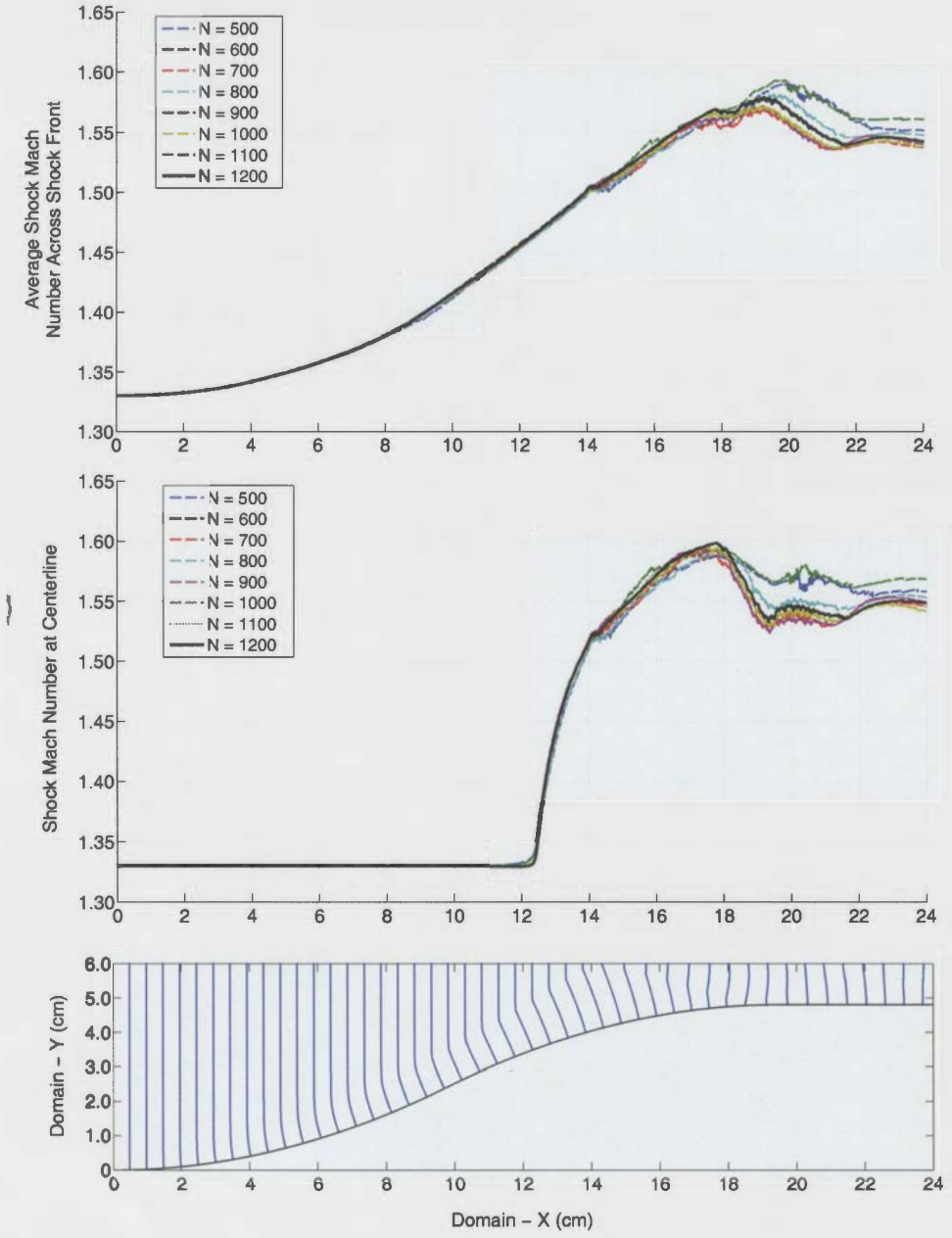

Figure C.8: Comparison of the average and absolute shock Mach number across the shock front and at the centerline respectively for a 195mm profile

Appendix D – Engineering Drawings

Engineering drawings are presented for the following manufactured pieces used for experimental testing. All manufacturing was conducted by the laboratory staff within the Mechanical Engineering Laboratory, University of the Witwatersrand, Johannesburg. The engineering drawings for the profiles, flat extensions and spacers are presented in the following order:

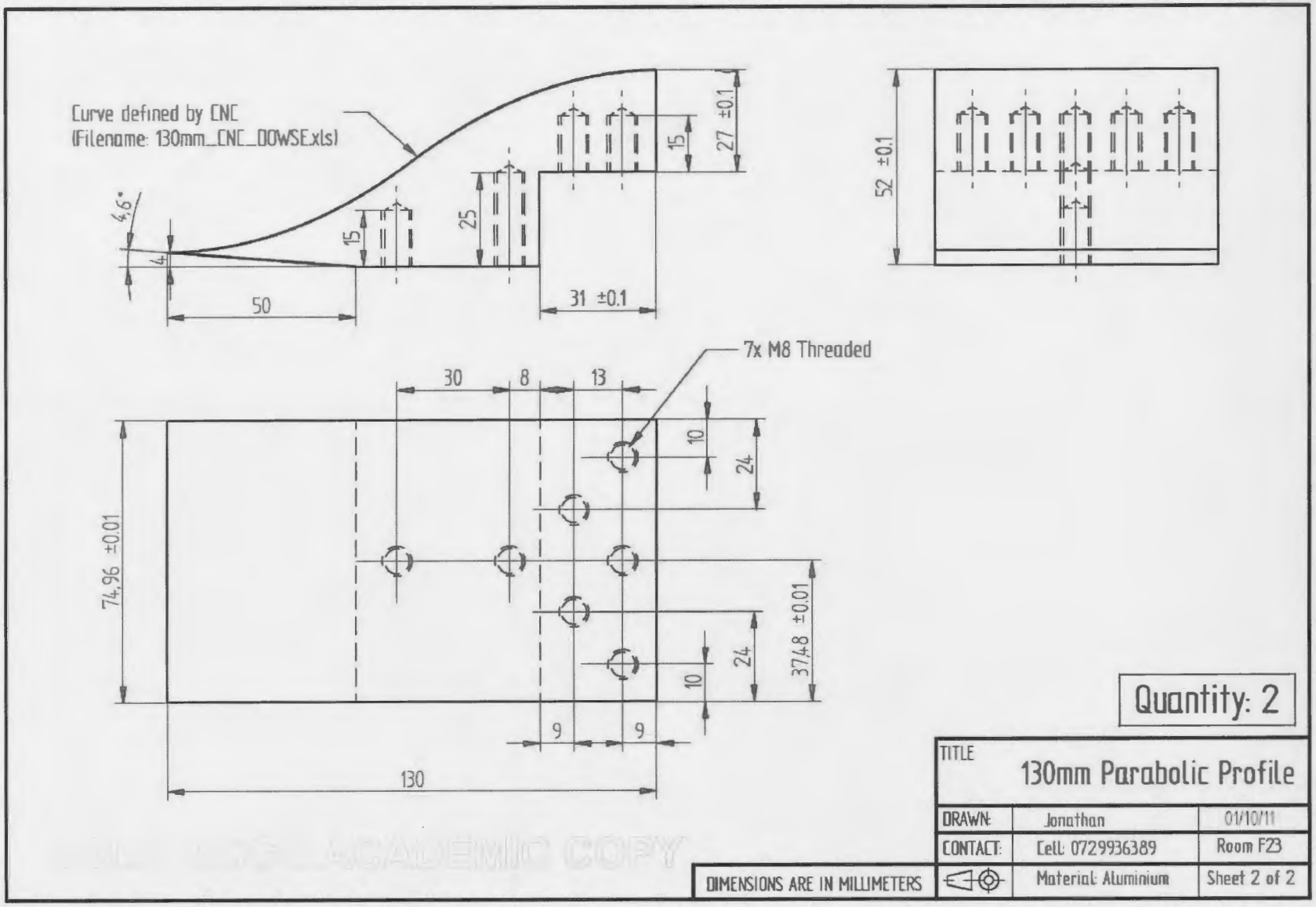

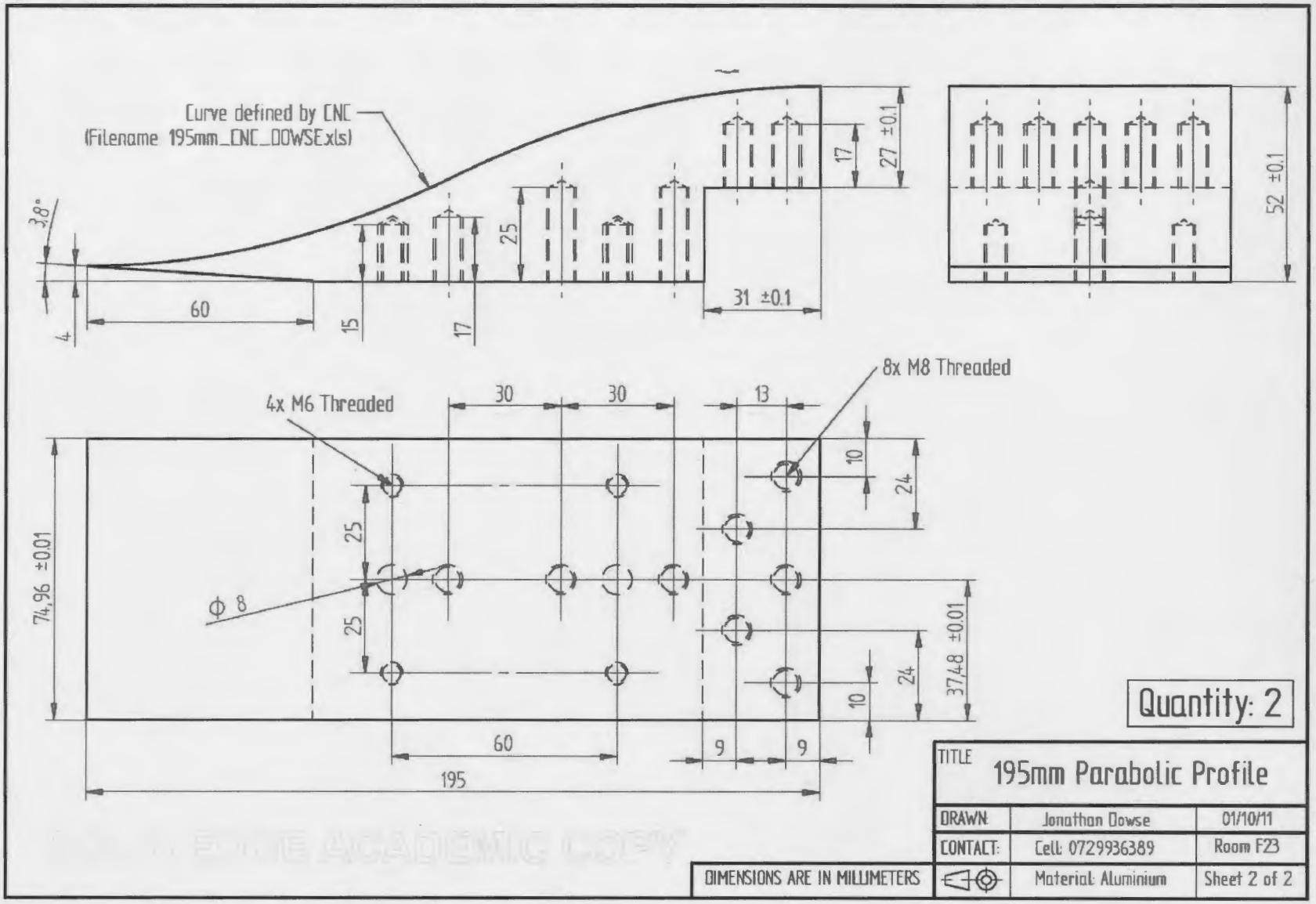

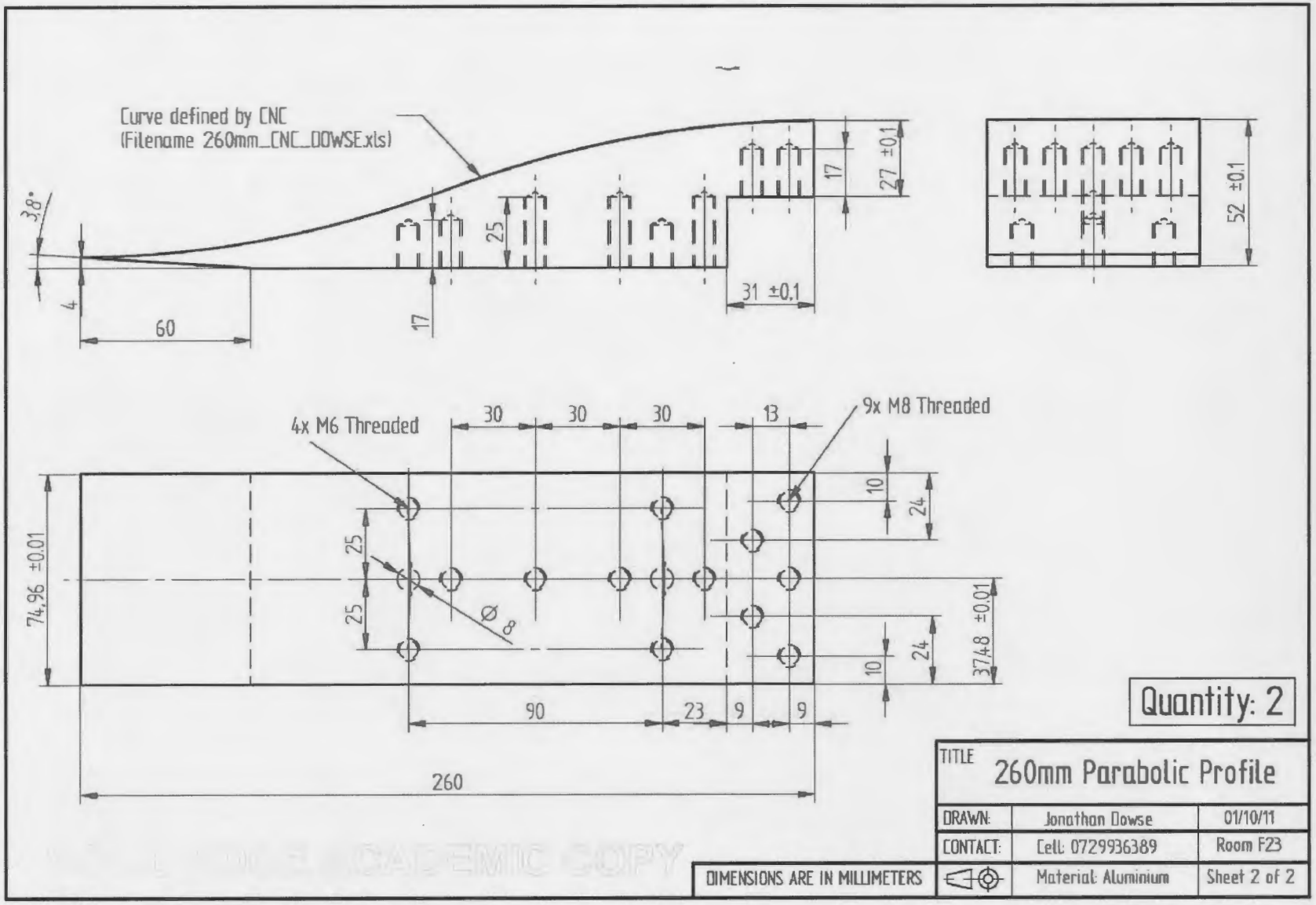

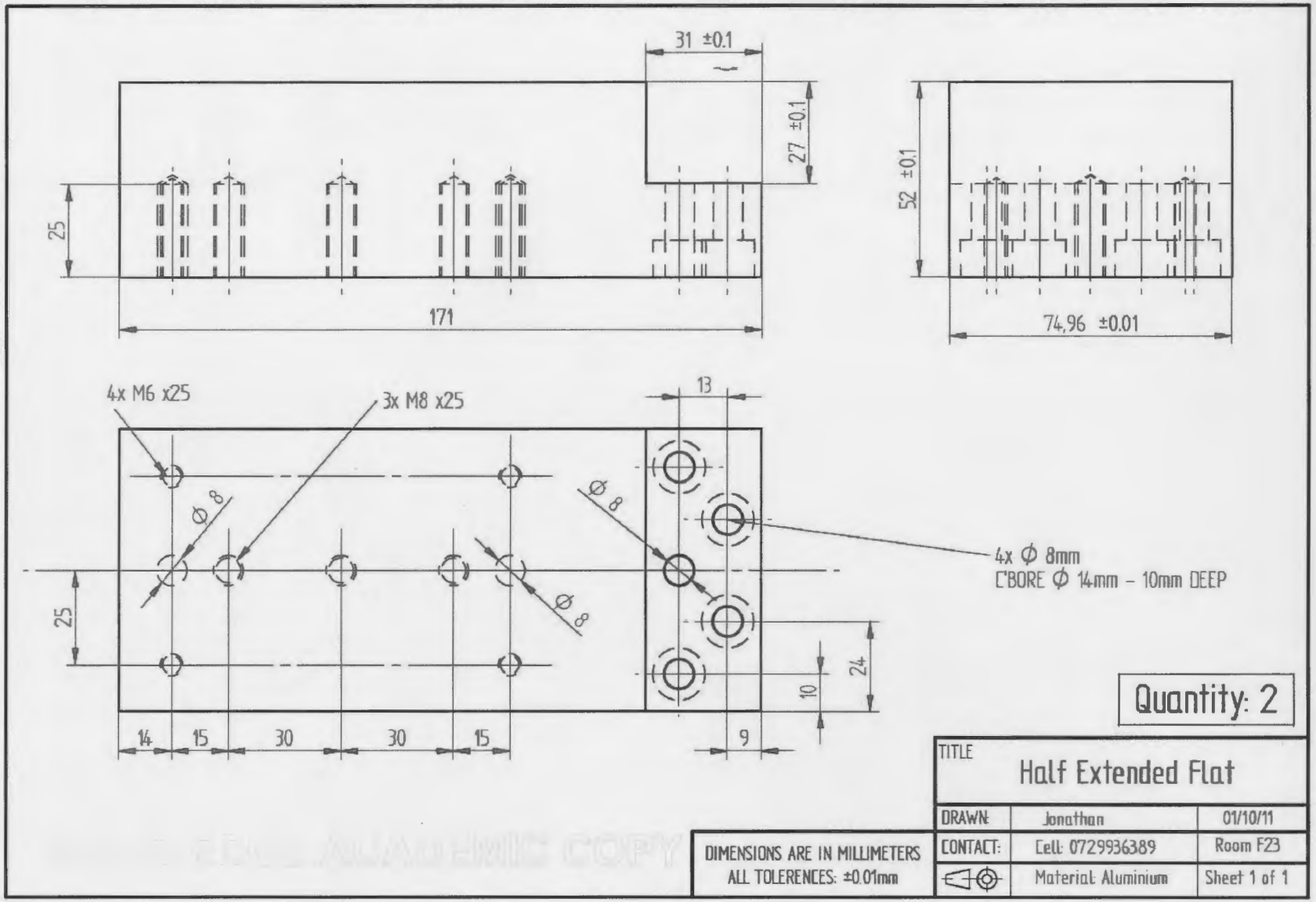
31 ±0.1
27 ±0.1
25
171
52 ±0.1
74,96 ±0.01
4x M6 x25
3x M8 x25
13
Ø 8
Ø 8
Ø 8
4x Ø 8mm
C'BORE Ø 14mm – 10mm DEEP
25
14
15
30
30
15
9
10
24
Quantity: 2
TITLE
Half Extended Flat
DRAWN: Jonathan 01/10/11
CONTACT: Cell: 0729936389 Room F23
Material: Aluminium Sheet 1 of 1
DIMENSIONS ARE IN MILLIMETERS
ALL TOLERENCES: ±0.01mm

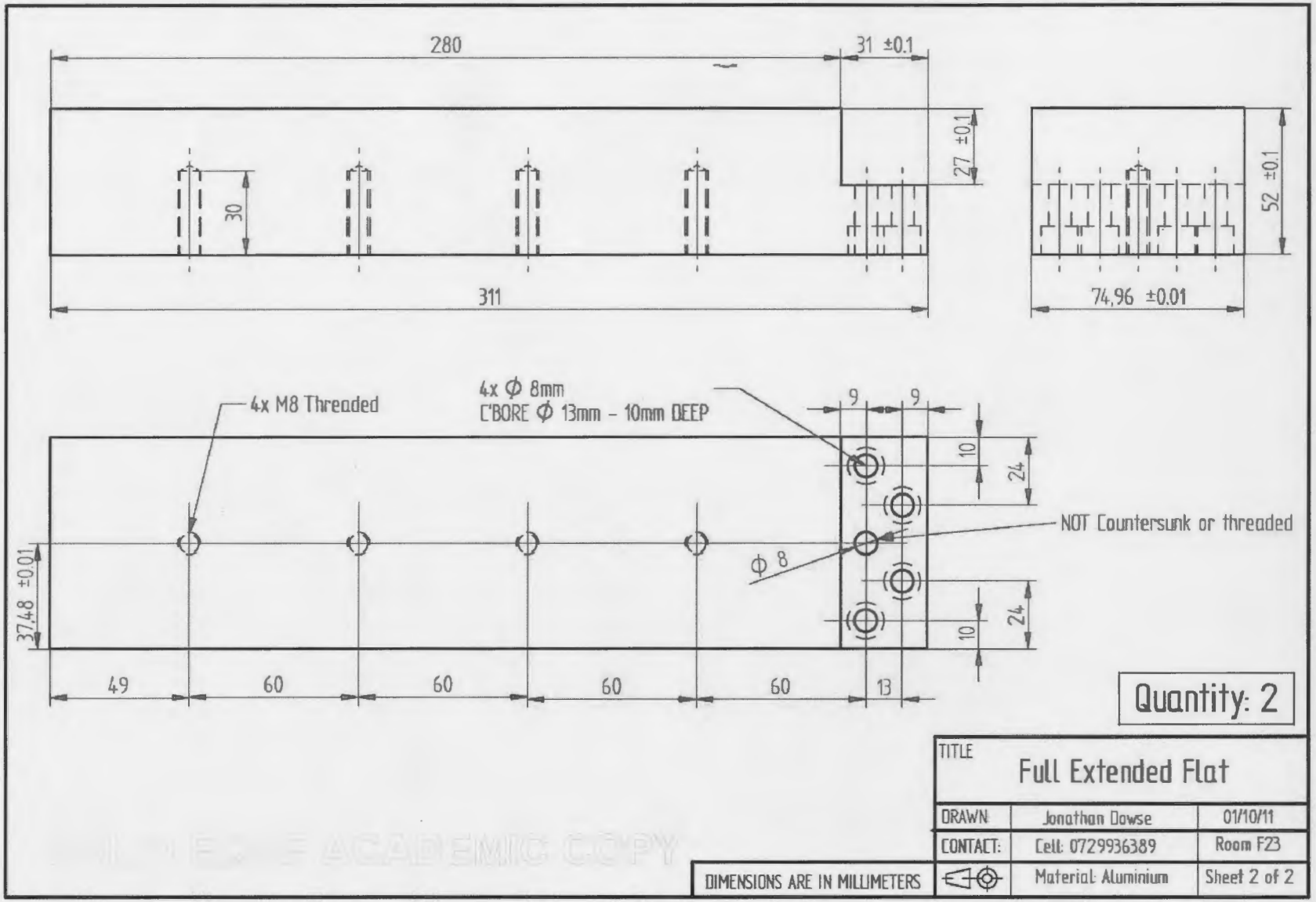

Quantity: 6

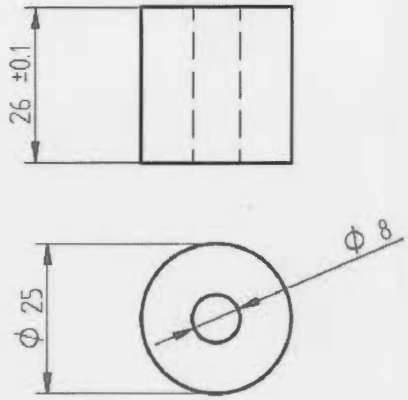

Quantity: 2

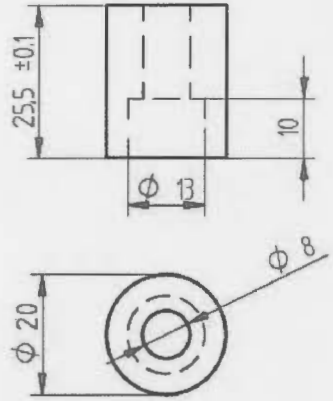

TITLE: Spacers		
DRAWN:	Jonathan Dowse	01/10/11
CONTACT:	Cell: 0729936389	Room F23
DIMENSIONS ARE IN MILLIMETERS	Material: Aluminium or PVC	Sheet 1 of 1